School of Science & Engineering
Department of Petroleum Engineering

Investigation of Gas Shale Pore Structure and its Influence on Transport Properties

Adnan S. Al Hinai

This thesis is presented for the Degree of
Doctor of Philosophy
of
Curtin University

October 2014

DECLARATION OF ACADEMIC INTEGRITY

To the best of my knowledge and belief this thesis contains no material previously published by any other person except where due acknowledgment has been made. This thesis contains no material which has been accepted for the award of any other degree or diploma in any university.

Signature:

Date:

DEDICATION

I would like to dedicate my thesis to my father (Saif Al Hinai) who has always drilled into my head "education is important". To my mother (Aisha Al Hinai), my wife (Maryam Al Habsi) and my children (Saif and Layal Al Hinai)

ABSTRACT

Petrophysical analysis of unconventional reservoirs such as gas shale formations still remains a challenge. This is mainly because of shale ultra-low permeability, the presence of a high percentage of clays, and the heterogeneity of the formation. The main research objective of this study is: to better understand the pore network of gas shale reservoirs, in order to map the fluid flow behavior of these pores, using several experimental techniques.

This thesis evaluates the microstructural characteristics of gas shale formations from the Perth Basin, Western Australia. It focuses on three key areas: (1) comparisons of pore size distribution; (2) recognizing the relationship between pore geometry and permeability; (3) the presence of clay on fluid transport properties. Combinations of mercury injection capillary pressure (MICP), low field nuclear magnetic resonance (NMR) and nitrogen adsorption (N_2) tests are used to determine the pore geometrical properties. The promising, innovative technique of high resolution, focused ion beam-scanning electron microscopy (FIB/SEM) is used to further support the experimental pore structure interpretations at sub-micron scale.

Initially, the discrepancies in the porosities and pore size distributions (PSD) are characterized. MICP computed pore throat size distribution down to 3 nm and presented most of the porosity "connected" involved in the fluid transport. While NMR provided the full spectrum of pore geometry, the total pore spaces. N_2 analysis demonstrated the pore size distribution in the micro-pore range (< 2 nm) that is not accessible by MICP and limited in low field NMR resolution.The results showed that porosities from MICP and N_2 are mostly identical; however NMR porosities show almost three times higher than MICP or N_2 porosities.

A new method to interchange MICP data with NMR data is established, through the estimation of the surface relaxivity parameter (ρ_2). The NMR transverse relaxation time (T_2) - equivalent capillary pressure, and MICP-equivalent T_2 were successfully estimated on gas shale samples from Western Australia.

An improved relationship between permeability and pore throat size is successfully established through regression. The findings reveal that the porosity symbolizes the

pore volume, and permeability reflects the pore throat size in the system. The strongest coefficient of correlation was when the mercury saturation reached 75%.

Three types of shales can be classified from samples studied, based on their clay contents: (i) low I/S but high kaolinite; (ii) high I/S but low kaolinite; and (iii) high I/S and high kaolinite. High I/S content recorded high entry pressure, consequent on low pore throat radius from MICP. Low I/S (but high kaolinite) has lower entry pressure and never reaches full saturation, up to 60,000 psi of pressure applied on the mercury. The N_2 adsorption and desorption curves for the tested samples indicate that the change in I/S to kaolinite ratio has an effect on the profile. As the clay component of mixed Illite/Smectite increases, the T_2 relaxation time tends to decrease, corresponding to smaller pore sizes or restricted environment.

ACKNOWLEDGMENTS

In The Name of Allah, The Most Gracious, The Most Merciful

First of all, I would like to express my utmost sincere appreciation to my supervisor Professor Reza Rezaee. I am grateful for his continual guidance and knowledge, which have provided the energy for me to push through the difficulties during my PhD research, not only academically but also through my personal life. I am also very thankful to my panel committee members Professor Brian Evans (chair), Dr. Stefan Igulear, Dr. Ali Saeedi and Dr Ben Clennell for their ideas and comments that helped me to refine the content of this project.

I would like to convey special thanks and appreciation to Dr. Lionel Esteban, who has continuously helped me with various experimental designs and data analysis, and with my written English. I also would like to thank Derek Winchester for preparing some of the experimental samples at very short notice.

In addition, I would like to thank the other research staff in the Petroleum Department. Dr. Mofazzal Hossain for his friendship and endless support during hard times. Also, my colleagues and office-mates (previous and current PhDs students): Yazeed, Abu Al Kasim, Muftah, Hanieh and Mehdi who have offered their friendship, advices, and support.

I thank Dr Christina Houen for copy editing my thesis according to the standards of the Institute of Professional Editing.

Ultimately, I am thankful to Allah for all opportunities that I have had. Also my sincere thanks and gratitude go to my family especially my father and my mother for their encouragement, prayers and love that helped me a lot throughout the duration of this project. I also thank my brothers and sisters for their cheer throughout this long process. My final and far most significant acknowledgement must be given to my wife, Maryam Al-Habsi, for her long suffering patience while I was working in this project; without her help and forbearance, this project would not have been done. And I hope she will be grateful now as I can come home early.

PUBLICATIONS

Al Hinai, A. and Rezaee R., 2012. "Nano Pore Scale Studies of Gas Shales". RIU Good Oil Conference, Perth, Australia. Technical Presentation.

Al Hinai, A., Rezaee R. and Esteban, L., 2012. "Gas Shale Pore Geometry Evaluation: An Example from the Perth Basin, Western Australia". AAPG/EAGE/SPE Shale Gas Workshop, Muscat, Oman. Technical Presentation.

Al Hinai, A., Rezaee, R., Saeedi, A. and Lenormand, R., 2013. "Permeability prediction from mercury injection capillary pressure: an example from the Perth Basin, Western Australia". *APPEA Journal* 53.

Labani, M., Rezaee, R., Saeedi, A. and **Al Hinai, A.,** 2013. "Evaluation of pore size spectrum of gas shale reservoirs using low pressure nitrogen adsorption, gas expansion and mercury porosimetry: a case study from the Perth and Canning Basins, Western Australia". *Journal of Petroleum Science and Engineering* 112:7-16.

Al Hinai, A., Rezaee, R., Esteban, L. and Jafari, H. 2014. "Shale gas pore assessment". *APPEA Conference.* Perth. Extended Abstract

Al Hinai, A., Rezaee, R., Esteban, L. and Labani, M., 2014. "Comparisons of Pore Size Distribution: A Case from the Western Australian Shale Gas Formations". *Journal of Unconventional Oil and Gas Resources* 8:1-13.

Al Hinai, A. and Rezaee, R. 2014. "Pore geometry of gas shale reservoirs". In Fundamentals of gas shale reservoirs. *Wiley-Blackwell*. Under publication

CONTENTS

List of Figures

List of Tables

1. CHAPTER 1: INTRODUCTION

1.1 Natural Gas Industry

Currently, the oil and gas industry is paying attention to producing hydrocarbons from unconventional resources such as gas shale reservoirs. These reservoirs potentially contain a large amount of natural gas. Natural gas is considered to be a premium fuel, as it has high caloric value, it is clean burning, relatively easy to handle and excellent for domestic use and heating (Olah et al., 2006). Natural gas is widely used in residential and commercial applications, for heating, electricity generation and as an alternative transportation fuel.

Natural gas production (with the main component of methane) from unconventional reservoirs has not been vigorously pursued, mainly because the formation has long been considered prohibitively expensive to access. However, with the great success of the Mississippian Barnett Shale exploitation (Jarvie et al., 2007), the growth of drilling and fracturing technologies and rising natural gas prices have attracted attention to these previously untapped reservoirs.

According to the US Department of Energy (2013), the United States has 7,299 trillion cubic feet of technically recoverable gas shale resources. The successful gas shale operations in the Barnett shale have encouraged the industry to accelerate its development activity in other shale plays.

With the increased interest in natural gas, petroleum engineers are progressively concerned with hydrocarbon flow in low permeability systems (Nelson, 2009) such as shale. Australia looks poised to commercialize its gas shale resources on a large scale. Australia is one of the top 10 countries in the world that contains large quantities of natural gas in shale formations. The US department of Energy (2013) estimates there are 4.7 trillion cubic feet of technically recoverable gas shale resources in the USA. There are a number of geological areas in Australia that are thought to be prospective for gas shale, such as the Cooper Basin (South Australia and Queensland), the Maryborough Basin (Queensland), and Perth and Canning Basin (Western Australia) (Figure 1-1).

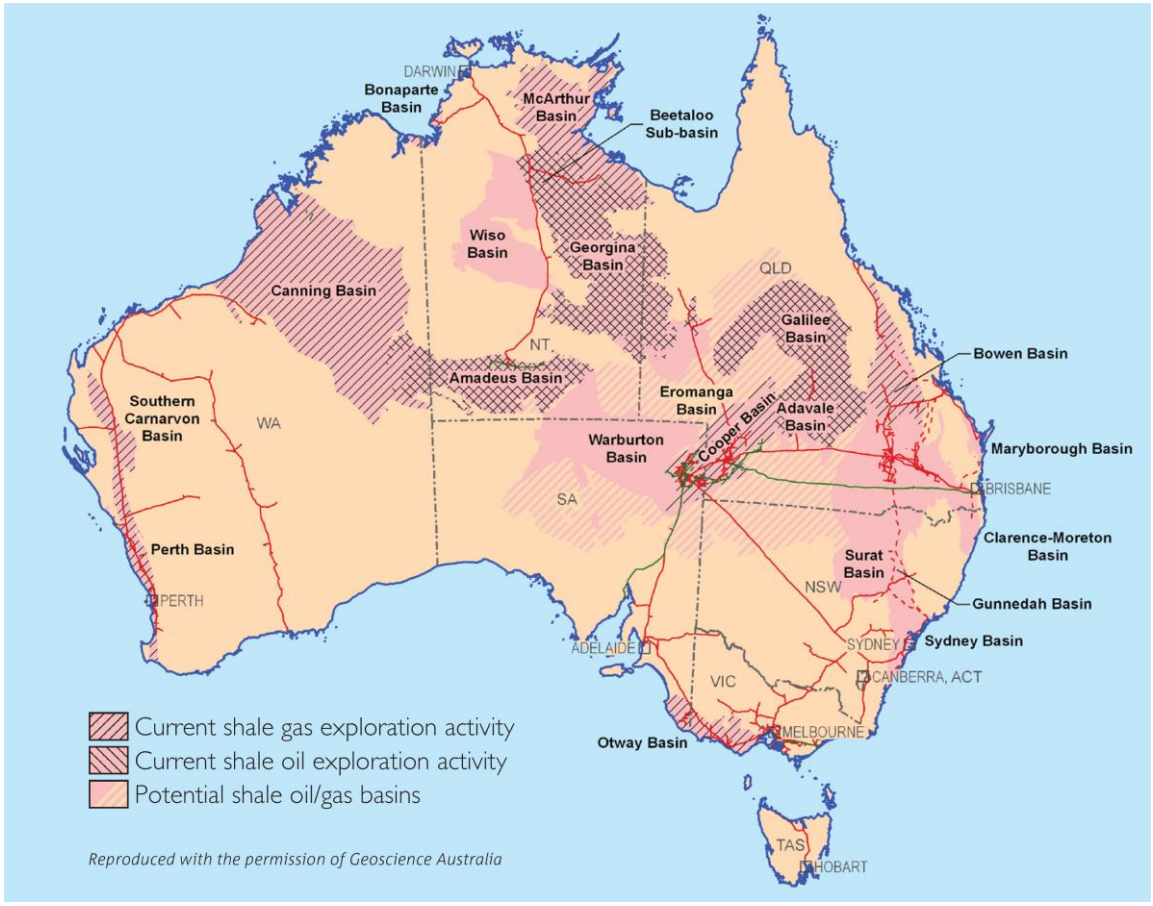

Figure 1-1: Current and potential gas shale resources in Australia (CSIRO, 2013)

1.2 Challenges Associated with Gas shale

Gas shale systems are composed of fine-grained sedimentary rock that is mainly consolidated by clay sized mineral grains. It is known as 'mudstone' in the category of sedimentary rocks. Fissile and laminated attributes makes shale distinguishable from other 'mudstones' (Salman et al., 2007). That is, the rock is made up of many thin parallel layers, and the rock readily splits into thin pieces along the layers.

The systems are typically organically rich; the higher total organic content (TOC) commonly has a higher adsorbed gas content (Boyer et al., 2006). Fracture stimulation is required for the systems to be economically processed (King, 2010). Fractures are created easily in silica rich and carbonate rich shales compared to clay rich shales, and total porosities are larger in clay rich shales than in silica rich shales (Bustin et al., 2008; Ross & Marc Bustin, 2009).

These reservoirs are unique because the pore structure and fluid flux characteristics differ significantly between formations, due to lithological differences resulting from sedimentology, diagenesis and structural history (Bustin et al., 2008; Evdokimov et al., 2006). This poses major challenges to the exploration and production of shale-gas reservoirs.

One of the most important and difficult variables to determine is the in-situ permeability (fluid flow parameter/reservoir quality) (Shaw et al., 2006) because gas storage capacity and transport behaviour is dictated by the pore structure (Bustin et al., 2008). Rock typing in terms of the hydraulic process (Rushing et al., 2008b) from porosity-permeability cross-plots is not practical in gas shale reservoirs because the dynamic range for porosity in shales is very narrow compared to sandstone.

An added challenge is measuring the porosity of shale samples by techniques such as injecting helium gas through the sample. Given that the molecule of helium is much smaller than methane (Bustin et al., 2008) and has greater access to fine pores, the helium porosity may be greater than the methane content of the pore space. Thus the porosity is overestimated and we may not determine the gas content correctly. However, helium can be utilized for the initial inspection and correction for sorption can be applied.

Core analysis under ambient or reservoir conditions is a common method for direct measurement of permeability. Because of high costs, only a limited number of core analyses are done for any particular field. Cuttings are available in almost all wells. The mercury injection technique may be used on well cuttings or chips (Jennings, 1987). As reservoir properties such as porosity and permeability are controlled by the size and arrangement of pores and throats, the mercury injection method is commonly employed to characterize pore size distribution and permeability in porous media (Swanson, 1981b; Katz & Thompson, 1987). Most of these studies have been for sandstones, and there is a lack of comprehensive studies for shale.

Transport properties of gas shale chiefly depend on the distribution of the pore spaces, which can be regarded as the connection of the void pore bodies by smaller void conduits (pore throats). Such characteristics can be described through geometrical rock properties, including porosity, size, shape and distribution of pore

bodies and throats, pore connectivity and body to pore throat size ratio. Shale pore geometry is acknowledged as exceptionally complex, and limited research has been done on the characterization of pore networks in shale rocks (mudstones) (Heath et al., 2011), because of constraints in sampling, measurement resolution and the heterogeneous nature of the rock increase.

Undeniably, a fluid's efficiency in flowing through the pore system (hydraulic conductivity and permeability) will also depend on the fluid-solid interactions, tortuosity of the pore network, intrinsic structures such as veins, faults or bedding (i.e. heterogeneities) and anisotropic aspects of these characteristics. At this stage, the only way to extract gas from gas shale is through extensive hydraulic fracturing (Gale et al., 2007), and the gas recovery efficiency will depend on the flow and trap properties of the gas shale. It is therefore crucial to understand the pore structures of gas shale. As yet, there is no clear understanding of how these pore systems are connected, and it is very possible that different reservoirs have different connectivities.

To evaluate small Pore Size Distribution (PSD) of gas shale, a limited range of laboratory techniques can be applied with their individual pros and cons:

(i) Mercury Injection Capillary Pressure method (MICP) is the most common method for characterizing the pore throat size distribution, using injection of mercury under controlled pressure;

(ii) Nitrogen adsorption (N_2) method evaluates the specific pore volume and PSD from the quantity of free and adsorbed gas;

(iii) Low field Nuclear Magnetic Resonance (NMR) qualifies and quantifies the magnetic response of protons under specific sequence(s) of applied magnetic fields that are dependent on the volume of fluids and on the pore body size distribution.

1.3 Research Objectives

This study uses a case study of organically rich gas shale samples to focus on understanding pore network characteristics in three key areas: (1) comparisons of pore size distribution; (2) recognizing the relationship between pore geometry and permeability; (3) effects of clay occurrence on fluid transport properties. The objectives are to:

(1) Compare PSD results from MICP with NMR and N_2 to understand the pore network characteristics of organically rich gas shale samples from Permo-Triassic Kockatea and Carynginia formations from the Northern Perth Basin. FIB/SEM image analysis was used to further verify the pore size at sub-micron scale and help to support laboratory pore structure analysis interpretations.

(2) Establish a practical approach to interchanging mercury injection capillary pressure (MICP) data with nuclear magnetic resonance (NMR) data to determine NMR transverse relaxation time (T_2)-equivalent capillary pressure and MICP-equivalent T_2 relaxation time.

(3) Develop a suitable methodology to determine gas shale permeability from MICP and NMR and compare various permeability models with laboratory measured permeability.

(4) The influence of clay types and pore structures on the fluid flow and storage capacity are also investigated. In addition, mineralogy is determined through XRD and SEM to substantiate the existence of different types of porosities in tested gas shale specimens coupled with identification of their composition that can have effects on pore distribution in these reservoirs.

The advantages and the shortcomings of the methods adopted to evaluate the pore system are also discussed. Knowledge of the pore network can provide an insight into fluid flow mechanism in gas shale reservoir to improve gas production.

2. CHAPTER 2: THEORETICAL BACKGROUND

2.1 Permeability

2.1.1 Introduction

Understanding laboratory permeability measurements of unconventional reservoirs has been a focus of the oil and gas industry in the past two decades (Lasswell, 2013). Various researchers have made attempts to understand shale permeability utilizing various approaches, and the results are not consistent. The main objectives of this chapter are to present two common approaches that are used to determine laboratory permeability and the mathematical relationships that describe fluid flow through a porous media. The two methods are steady state and unsteady state permeability measurements; their methodology, advantages and disadvantages are discussed.

The basic law of flow through a porous medium can be described by Darcy's law, developed by Henry Darcy in 1856. Darcy's Law states that the velocity of a fluid in a porous medium is proportional to the pressure gradient and inversely proportional to the fluid viscosity (Figure 2-1) and is expressed as:

$$q = \left(\frac{K}{\mu}\right)\left(\frac{A}{L}\right)\Delta P \qquad \text{Equation 2-1}$$

where, q is the volumetric flow rate in cubic centimetres per second and A is total cross-sectional area of the rock in square centimetres, L is the length of sample (cm), ΔP is the pressure drop across the sample (atm), μ is the fluid viscosity centipoise units, and k is the permeability in Darcy units.

Darcy's law can be applied in confidence when the flow is laminar. When the flow becomes turbulent (differential pressure is proportional to the flow rate), the flow becomes non-Darcy (Figure 2-2) because Darcy's law is applied to the macroscopic level and not the microscopic level.

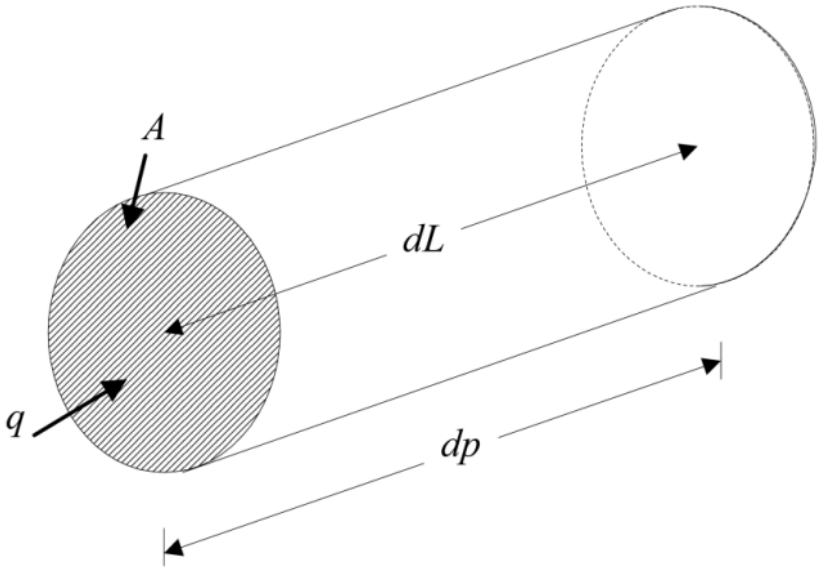

Figure 2-1: Schematic diagram illustrating the flow thru a porous media. The velocity in the medium is proportional to the pressure gradient (Saeedi, 2013a)

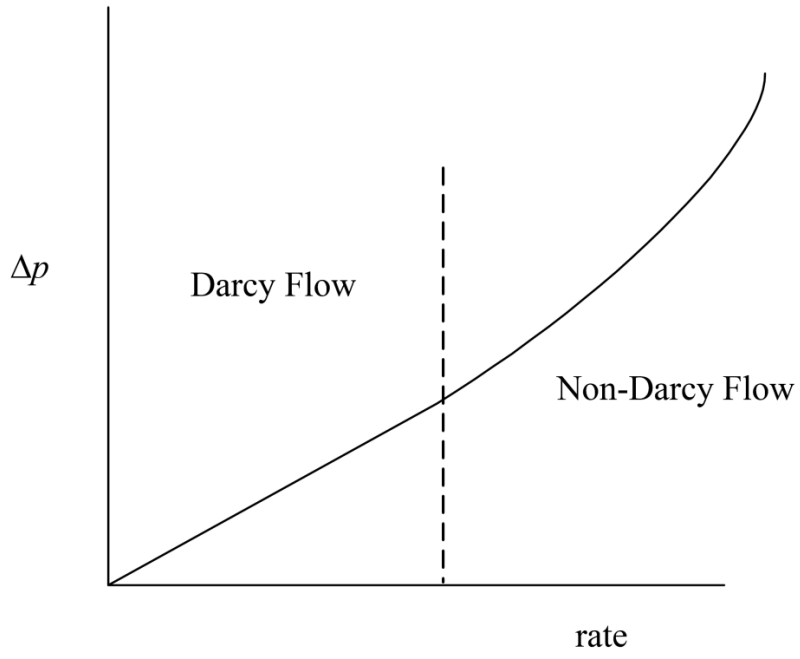

Figure 2-2: Plot describing differential pressure versus flow rate for Darcy and non-Darcy flow (Saeedi, 2013a)

2.1.2 Flowing Fluids

Gas shale permeability can be classified in two types; fracture and matrix permeability. Fracture permeability is described as the ability of the fluid to flow in the pore system through its natural or induced (hydraulic) fracture. These are commonly in the milli-Darcy range. Matrix permeability is the fluid conveyed through the intact portion of the rock. In this study, matrix permeability is measured (Saeedi, 2013a). In permeability measurements, either gas or liquid (commonly brine) is used as the flowing fluid. Gas and brine flooded experiments would produce different permeability readings even when using the same medium. Hence, it is important to know how we can relate gas permeability to liquid permeability.

Liquid Flooding: The permeability of a rock would remain constant and is independent of the differential pressure when the flow is laminar and there is no interaction between the fluid and the rock and the liquid has completely filled the pore space. In this situation, where the fluid is laminar, the fluid adheres to the surface. The velocity is zero at the surface of the rock and maximum in the middle of the pore (Saeedi, 2013a).

Gas Slippage: Permeability experiments conducted using gas as the flowing medium would reveal higher permeability values. The difference in molecular movement of gas as compared to liquid movement results a dependence of permeability on the mean pressure of the existing gas during the time of measurement, this effect is known as Klinkenberg effect. The microscopic flow can be described as "average" gas permeability:

$$K_g = K_l \left(1 + \frac{b}{<P>}\right) \qquad \text{Equation 2-2}$$

where Kg is the average gas permeability, K_l is the Klinkenberg corrected permeability that is determined from the intercept; b is the gas slippage factor that is computed from the slope of the gas permeability versus the reciprocal average pressure plot (Figure 2-3). The Klinkenberg plot is used to determine the liquid permeability and also take into account the gas slippage effects (Figure 2-4).

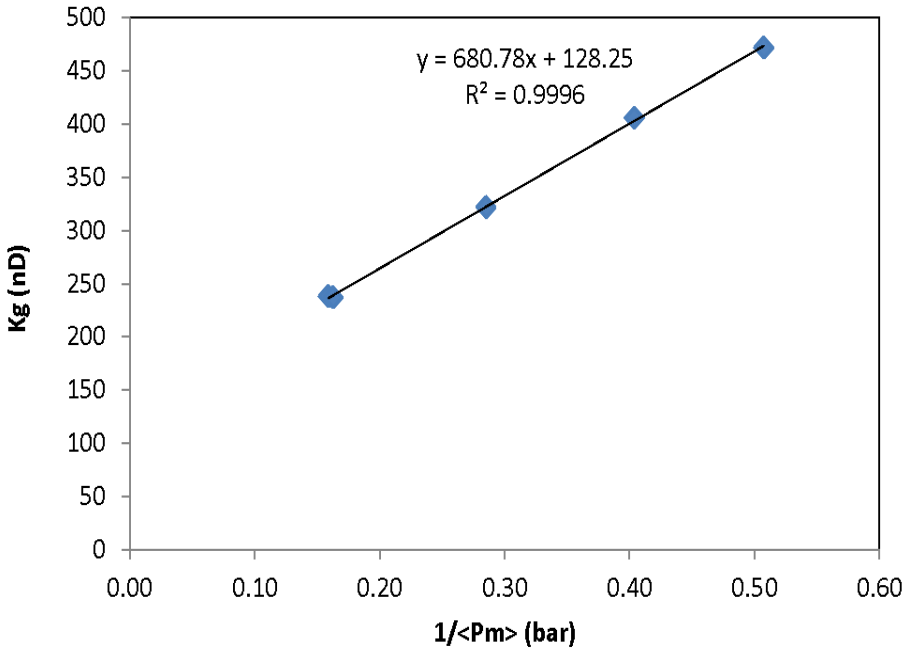

Figure 2-3: Gas permeability versus the reciprocal average pressure. The slope is the gas slippage factor.

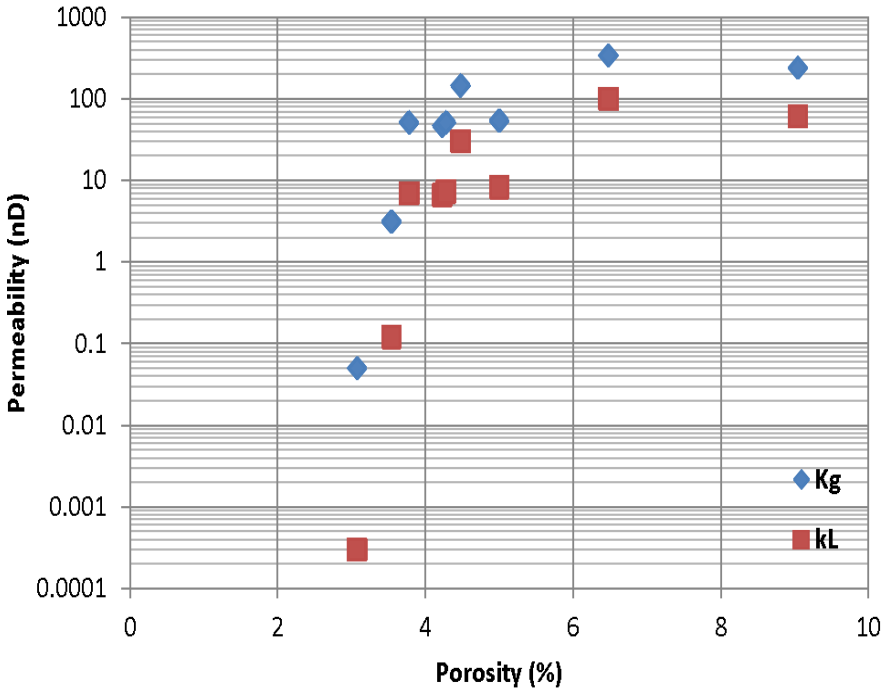

Figure 2-4: The measured porosity and permeability (gas and liquid) of the samples in the study

2.2 Determination of Capillary Pressure Profile

2.2.1 Introduction

Gas shale reservoirs play a major role in exploration and production because they are deemed to be both source rocks and cap rock. They display good sealing characteristics due to their small pore throats, which are responsible for creating high capillary pressures (Al-Bazali et al., 2005). To understand capillary pressure behaviour, mercury intrusion experiments are normally conducted.

The mercury intrusion capillary pressure (MICP) technique is used to determine various quantifiable aspects of a porous medium such as pore diameter, total pore volume, surface area, and bulk and absolute densities (Burdine et al., 1950; Chen & Song, 2002; Kale et al., 2010a, 2010b) as a function of pressure, correlated with permeability in some rocks (Dastidar et al., 2007; Ma et al., 1991; Owolabi & Watson, 1993; Swanson, 1981a) and rock typing in shale by integrating geological cores (Kale et al., 2010a) .

2.2.2 MICP Porosimetry Technique

This technique involves the intrusion of mercury (non-wetting liquid) at high pressure into a material through the use of a special assembly called a penetrometer. The pressure is applied at a constant rate (pressure steps between 5–60,000 psi) and the volume of the injected mercury is measured at each increment (Figure 2-5).

Consider a capillary tube immersed in a water-gas system, as shown in Figure 2-6. The capillary force is shown acting along the surface of the water, which forms the contact angle θ with the wall of the tube. The force is proportional to the energy required to maintain the interface between the water and oil. This is called interfacial tension σ, for a liquid-liquid interface, or surface tension for a liquid-gas interface, and has units of force per unit length. σ is also sometimes referred to as the specific free energy of the interface. The length over which this force is applied in a capillary tube is the circumference of a circle of radius r. Thus the total capillary force is $2\pi r\sigma$ and the vertical component of the force is $2\pi r\sigma cos\theta$. When this is expressed as a pressure, by dividing the total force by the cross-sectional area, πr^2, thus the capillary pressure can be obtained (Tiab & Donaldson, 2004).

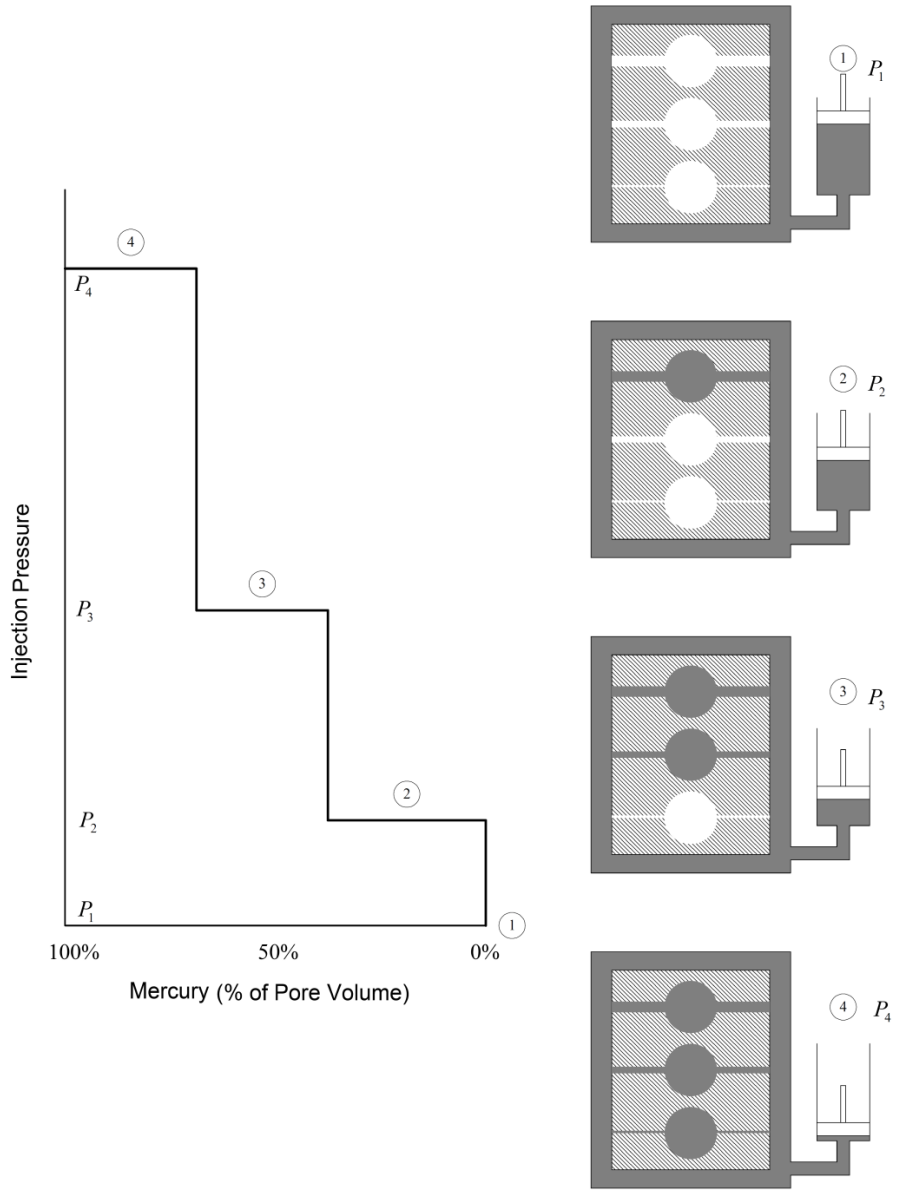

Figure 2-5: Schematic diagram showing the capillary pressure experiment. The pressure is applied at a constant rate and the volume of the injected mercury is measured at each increment (Saeedi, 2013b)

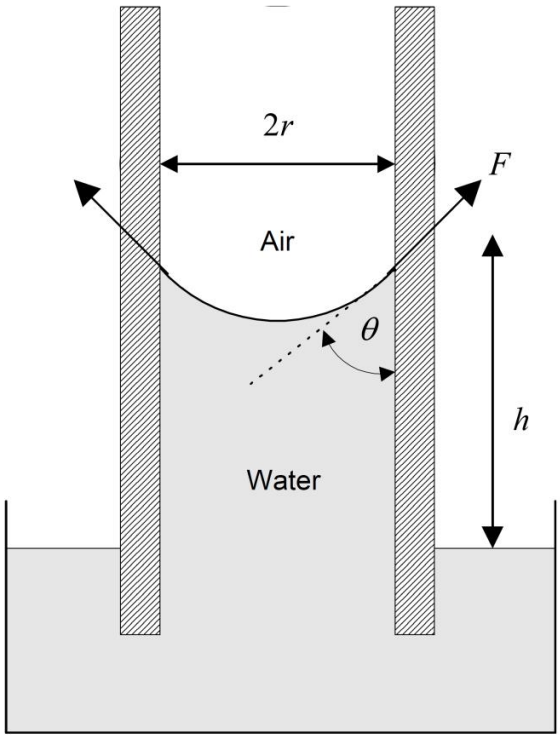

Figure 2-6: Schematic diagram showing the capillary force acting on the water when a capillary tube is immersed into a gas-water system. The capillary pressure can be obtained by dividing the total force by the cross sectional area (Saeedi, 2013b)

The pore throat radius can be found from the entry pressure at the beginning of the sudden pressure drop, assuming cylindrical pores, by the Laplace-Washburn (1921) equation:

$$R = \frac{2\sigma\cos\theta}{P_c} \qquad \text{Equation 2-3}$$

where Pc is the entry pressure (psi), σ is the interfacial tension (dynes/cm), θ the contact angle (degrees) and R is the pore throat radius (um). The minimum capillary entry pressure is the capillary pressure at which the non-wetting phase starts to displace the wetting phase, confined in the largest pore throat within a water-wet formation. The capillary entry pressure can be major, particularly for shales with very small pore throats (permeability) (Al-Bazali et al., 2005). The entry pressure is inversely proportional to the size of the pore in which mercury will intrude (radius).

Figure 2-7 shows the capillary pressure curve during the injection process. At the lower injection pressure, the mercury starts to enter the large pores and then starts to plateau at lower injection pressure. The bend "apex" or the inflection point is proposed by Swanson (1981), where the pressure curve starts to have a steep slope towards the higher capillary pressure, illustrating the smaller pore throats, mircro-pores or nano-pores when dealing with tight gas or gas shale rocks.

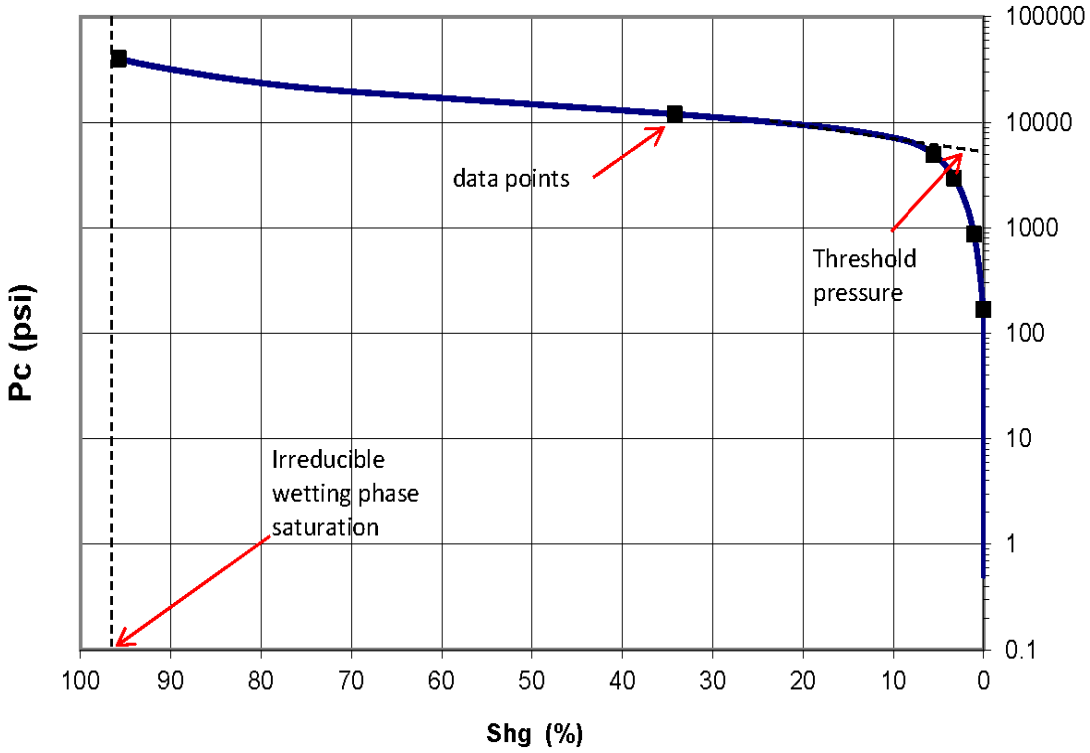

Figure 2-7: Illustration of capillary pressure curve profile during the injection process. At low pressures, the mercury starts to invade the large pores. At the inflection point "apex", the mercury starts to invade smaller pores.

However, mercury intrusion experiments alone do not provide full experimental characterization of pore geometry (Chen & Song, 2002), because they operates by injecting pressure incrementally into the porous media and recording the injected volume at each step. This type of pressure controlled instrument measures the pore throat size (pore entry radii) and does not detect the size of the pore body behind the throats (Burdine et al., 1950; Churcher et al., 1991; Heath et al., 2011).

2.2.3 MICP Permeability

From a review of the literature on the permeability estimation model, several models appear to be available, with varying derivations and assumptions. These models have generally two basic theories behind their derivation — Poiseuille theory and Percolation/characteristics length theory. Poiseuille theory describes the rock's internal shape as entangled tubes with varying complexity, and as such defines the permeability using parameters which define several internal characteristics such as cementation and tortuosity (Comisky et al., 2007). Percolation theory assumes the internals of the rocks to be interconnected in a completely random manner, and that fluid spreads in that medium randomly. This randomness is due to the nature of the medium, which can be modeled under percolation to predict fluid flow. The modeling involved in Percolation theory involves the description of characteristics of a specific length and bulk volume (cylindrical sample) of materials which would be stimulated as a small reservoir (Comisky et al., 2007; Fleming, 1983). Thus this approach is also known as the length characteristics theory.

Permeability models are as follow:

Capillary Tube Models

Kozeny (1927) made an attempt to systematically quantify the relationship between porosity and permeability. He made a simplifying assumption that a porous rock could be considered to consist of a bundle of capillary tubes of equal length. For this situation the Hagen-Poiseuille's law describes laminar flow, which, for a single tube, is:

$$q = \frac{\pi r^2}{8\mu}\frac{\Delta P}{L} \qquad \text{Equation 2-4}$$

Where r is the tube radius, ΔP is the pressure drop across the tube, μ the fluid viscosity and L is the length. From equation (2-1) & (2-4), the effective permeability of a (horizontal) tube is:

$$k = \frac{r^2}{8} \qquad \text{Equation 2-5}$$

The porosity (*Ø*) of a bundle of (*n*) capillaries whose ends occupy a surface area of (*A*) is given by:

$$\emptyset = \frac{n\pi r^2}{A} \qquad \text{Equation 2-6}$$

From equation (2) and comparing with Darcy's law gives:

$$k = \frac{\emptyset r^2}{8} \qquad \text{Equation 2-7}$$

Implying that the permeability of a reservoir rock will depend on porosity and the square of the pore throat size. This shows quite simply that permeability has the dimensions of $[L]^2$. This approach can be modified to allow for tortuosity, τ, of the real pore network, such that the actual length of each capillary is *L*, to give:

$$k = \frac{\emptyset r^2}{8\tau} \qquad \text{Equation 2-8}$$

Tortuosity can be determined from electrical properties:

$$\tau = \emptyset F \qquad \text{Equation 2-9}$$

Where F is the formation resistivity factor ($F=\emptyset^{-m}$), where m is the cementation factor that have values of 1 to 3. Equation (6) gives:

$$k = \frac{\emptyset r^2}{F} \qquad \text{Equation 2-10}$$

Katz and Thompson (Katz and Thompson 1986) introduced an equation to estimate permeability from percolation theory:

$$k = 226\frac{l_c}{F} \qquad \text{Equation 2-11}$$

where l_c, is the diameter of the critical pore throat size that have the major contribution to permeability (the inflection point on the capillary pressure curve).

Katz and Thompson permeability equation also can be written as

$$K = 17.7R_c^2\emptyset^m \qquad \text{Equation 2-12}$$

Equation 10 is employed from percolation theory to derive a deceptively simple relationship, on the influence of pore structure on flow properties. Their relationship suggests that permeability can be estimates by assuming that the effective pore size is the smallest pore on the connected path of pores containing the largest pores. The authors argue that the inflection point marks the pressure at which a sample is first filled continuously end to end with mercury and the largest pores first filled are those that control permeability.

Empirical Models

The empirical models are based on parameters such as pore throat radius, grain size, specific surface area and irreducible waster saturation that may or may not have a direct effect on permeability. In this study, pore throat size are discussed.

Swanson (1980) extended on the work of Purcell (1949) in developing a new method of correlating permeability with capillary pressure data. In order to relate capillary pressure data with permeability, they have defined an apex (inflection) point on the graph that has the major contribution to permeability (Swanson 1981). The work was based on 319 samples (carbonates and sandstone), the air permeability is:

$$K_{swanson,air} = 399\left[\frac{S_b}{P_c}\right]_{Apex}^{1.691} \qquad \text{Equation 2-13}$$

Walls and Amaefule (1985) modified Swanson's (1980) approach for low permeability sands. They found the logarithm of mercury saturation against the square root of capillary pressure mercury saturation ration. By correlating the Swanson parameter with air permeabilites thay developed an dequation for calculating absolute permeability:

$$K_{W-A} = 30.5\left[\frac{S_b}{P_c}\right]_A^{1.56} \qquad \text{Equation 2-14}$$

Where K is the permeability (mD), P_c is the capillary pressure (psia), (S_{Hg}/P_c) is the mercury saturation/capillary pressure apex and A is the apex, the point on log(P_c) vs log(S_b) curve at the 45 degree line becomes tangent.

Jennings (1987) used the capillary pressure corresponding to 50th percentile of mercury saturation to estimate permeability:

$$K = e^{[-2.5\ln(P_2)+11.9]} \qquad \text{Equation 2-15}$$

Where K is permeability (mD); P_2 is the 2nd quartile of pressure (psi) corresponding to 50% mercury saturation. Jennings (1987) noted that equation (6) does not work for rocks that have permeability values below one mD.

Kamath (1992) reviewed the work of Swanson, Thompson and Walls and Amaefule to introduce a new correlation to estimate permeability from capillary pressure data. The equation proposed was for tight gas sands having permeability less than one mD.

$$\mathrm{K_{Kammath}} = 413\left[\frac{\mathrm{S_b}}{\mathrm{P_c}}\right]^{1.85}_{\mathrm{Apex}} \qquad \text{Equation 2-16}$$

Winland proposed a method of estimating permeability based on 202 samples from 14 formations. A regression analysis was used to develop an empirical relationship for absolute permeability, effective porosity and a capillary pressure parameter (R_{35}). R_{35} is the pore throat radius at mercury saturation of 35%, where this is a function of both pore entry size and the sorting of the pore throat sizes.

$$\log\left(K_{winland/air}\right) = -1.25 + 1.469\log(\emptyset) + 1.7\log(R_{35}) \qquad \text{Equation 2-17}$$

$$K_{winland} = 49.4R_{35}^{1.7}\emptyset^{1.47} \qquad \text{Equation 2-18}$$

Dastidar (2007) introduced another method of estimating permeability from mercury injection by using the weighted geometric average of the pore throat radius (R_{WGM}). They suggest that by considering the weighted geometric mean, it includes the whole spectrum of the pore throats in the sample by multiplying each pore throat by its fractional contribution.

$$K_{OU} = 4073 R_{wgm}^{1.64} \emptyset^{3.06}$$ Equation 2-19

$$\log(K) = -2.51 + 3.06 \log(\emptyset) + 1.64 \log(R_{wgm})$$ Equation 2-20

Where weighted geometric average pore throat radius (R_{WGM}) is:

$$R_{wgm} = \exp\left[\frac{\sum_{i=1}^{n} w_i \ln(R_i)}{\sum_{i=1}^{n} w_i}\right]$$ Equation 2-21

Timur (1968) model suggests the use of FFI (free fluid index) obtained from nuclear magnetic logs to estimate the irreducible water saturation which would later be used for permeability estimation(Timur 1968Timur 1968). Using 155 Sandstone samples of the different fields, permeability was believed to be best estimated through the formulated equation:

$$K = 0.136 \frac{(100\emptyset)^{4.4}}{(100 S_{wir})^2}$$ Equation 2-22

Where the S_{wir} is the irreducible water saturation, $\emptyset$ is the porosity and K is the permeability in micro Darcy.

2.3 Nuclear Magnetic Resonance

2.3.1 Introduction to NMR

The NMR tool was initially used as a spectroscope for the medical industry. It was discovered in 1946 and was primarily used for understanding molecular composition and molecule structure. NMR has become a key practice for description of porous media in recent years, since it was proposed in the 80s (Beilby, 1998; Cohen & Mendelson, 1982). It is a powerful way for computing and characterizing the properties of the fluid rock systems and obtaining information such as porosity, pore size distribution and permeability, and has become a popular tool in the industry (Coates et al., 1999; Hidajat et al., 2003).

2.3.2 Fundamentals of NMR

NMR measures the amount of protons in a given sample (Figure 2- 8). Protons are positively charged small particles. In terms of core samples, the protons are the "hydrogen nuclei" that are found in reservoir fluids—water and hydrocarbons (oil and gas). A nucleus of this type has the property called spin (Hornak, 2011) which can be assumed to be a small magnetic field and will cause the nucleus to produce an NMR signal. In the absence of an external magnetic field, the magnetic moments of all the atoms are random within a body. When an external static magnetic field is applied, the moments will rearrange themselves in parallel to the direction of the field, with the objective of creating a net magnetization within the body. The individual proton precesses at a frequency called Larmor Frequency, and it is proportional to the magnitude of the static magnetic field and to the gyromagnetic ratio of the given nucleus. Different nuclear types have different Larmor frequencies (Coates et al., 1999), because of different gyromagnetic ratios; hence different nuclei can be distinguished on the basis of these frequencies.

Figure 2-8: Low field Maran Ultra-Spectrometer 2 MHz used in this study to measure the amount of hydrogen protons in a given sample

At equilibrium, the net magnetization vector lies along the direction of the applied magnetic field Bo and is called the equilibrium magnetization Mo (Figure 2-9). In this configuration, the Z component of magnetization M_Z equals M_o. M_Z is referred to as the longitudinal magnetization. The time constant which describes how MZ

returns to its equilibrium value is called the spin lattice relaxation time or the longitudinal relaxation time T_1 , the first cycle in making NMR measurements, and it does not occur instantly but rather develops with a time constant (Hidajat et al., 2003; Hornak, 2011; Puddephat, 2001) and is given by:

$$M_z(t) = M_o(1 - e^{-t/T_1})$$ Equation 2-23

where Mz(t) is the magnitude of the magnetization at time t, t is the time that protons are exposed to the static magnetic B_0 field, and M_o is the final and maximum magnetization in a given magnetic field.

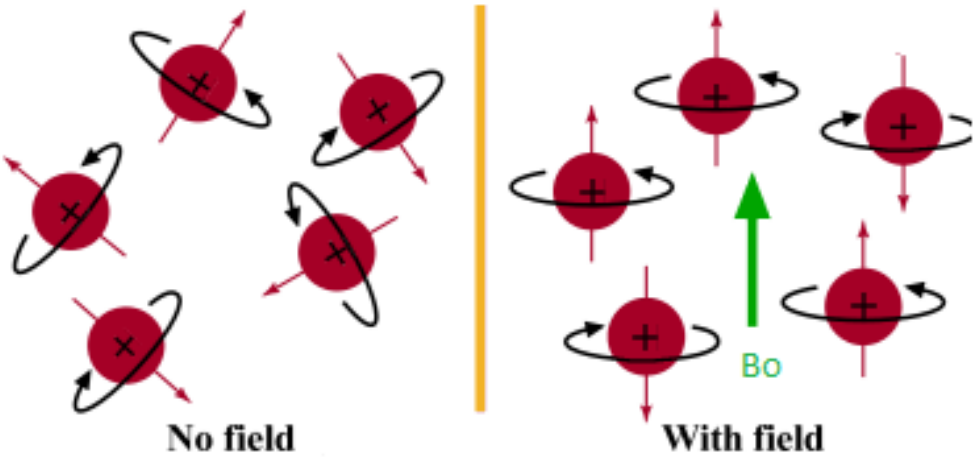

Figure 2-9: (left) in the absence of a magnetic field the hydrogen nuclei are randomly oriented. (Right) when an external magnetic field is applied the hydrogen nuclei are aligned with respect to the magnetization field (B0). Modified from Education (2000)

The second cycle in making NMR measurements is to apply a second magnetic field B_1 perpendicular to B_o (i.e. tipping the magnetization from the longitudinal direction to a transverse plane). When the B_1 field is switched off, the proton population begins to dephase, the precessions of the protons will no longer be in phase with one another and a decaying signal will be detected. This decay is usually exponential and is called free induction decay (FID) (Coates et al., 1999).

The time constant of the transverse magnetization decay is called the transverse relaxation time, referred as to T_2. For a single pore the magnetization decay as a function of time is given by

$$M(t) = M_o \exp\left(\frac{-t}{T_2}\right)$$ Equation 2-24

(Oren et al., 2002, Talabi et al., 2009), where M(t) is the magnetization at time t, Mo is the magnetization at initial time (t=0) and T_2 is the transverse relaxation time.

For fluids in rock pores, there are three independent mechanisms that act parallel: (1) bulk fluid process (2) surface relaxation and (3) diffusion in the presence of magnetic field gradient. The times are given (Coates et al., 1999) by:

$$\frac{1}{T_2} = \frac{1}{T_{2bulk}} + \frac{1}{T_{2surface}} + \frac{1}{T_{2diffusion}}$$ Equation 2-25

$$\frac{1}{T_1} = \frac{1}{T_{1bulk}} + \frac{1}{T_{1surface}}$$ Equation 2-26

Where,

T_2 = transverse relaxation time of the pore fluid

T_{2bulk}= T_2 relaxation time of the pore fluid as it would be measured in a container so large that container effects would be negligible (Coates et al., 1999). The bulk relaxation is a fluid property and mainly influenced by the physical nature of the fluid such as viscosity and chemical composition.

$T_{2surface}$=T_2 relaxation time of the pore fluid resulting from surface relaxation. It occurs at the fluid solid interface (grain surface) and varies with minerology.

$T_{2diffusion}$ = T_2 relaxation time of the pore fluid as induced by diffusion in the magnetic field gradient.

T_1 = the measured longitudinal relaxation time of the pore fluid.

T_{1bulk} = T_1 relaxation time of the pore fluid as it would be measured in a container so large that container effects would be negligible.

$T_{1surface}$ = T_1 relaxation time of the pore fluid resulting from surface relaxation.

Gas T_{2bulk} relaxation (Coates et al., 1999) is given by :

$$\frac{1}{T_{2bulk}} \cong 2.5 \times 10^4 \left(\frac{\rho_g}{T_K^{1.17}} \right)$$ Equation 2-27

Where,

T_K = temperature (°K)

ρ_g = gas density (gm/cm3)

$T_{2surface}$ relaxation (Beilby, 1998) is given by:

$$\frac{1}{T_{2surface}} = \rho_2 \left(\frac{S}{V} \right)_{pore}$$ Equation 2-28

Where,

ρ_2 = $T_{2surface}$ relaxivity (T_2 relaxing strength of the grain surfaces)

(S/V)pore = ratio of pore surface to fluid volume

The diffusion relaxation rate ($1/T_{2diffusion}$) is given by:

$$\frac{1}{T_{2diffusion}} = \frac{D(\gamma GTE)^2}{12}$$ Equation 2-29

Where,

D = molecular diffusion coefficient

γ = gyromagnetic ratio of a proton

G = field-strength gradient (G/cm)

TE = inter-echo spacing used in the CPMG sequence.

The molecular diffusion for gas decreases with increase in pressure, due to the increase in gas density as pressure increases; the diffusion coefficient is given by:

$$D_g \cong 8.5\times10^{-2}\left(\frac{T_K^{0.9}}{\rho_g}\right)\times10^{-5} cm^2/s \qquad \text{Equation 2-30}$$

Hence, the transverse relaxation mechanism for fluids in rock pores, which we are interested in, can be written as:

$$\frac{1}{T_2}=\frac{1}{T_{2bulk}}+\rho_2\left(\frac{S}{V}\right)_{pore}+\frac{D(\gamma GTE)^2}{12} \qquad \text{Equation 2-31}$$

The last member of the equation (2-12) represents the diffusion aspect of the spin-echo, with D for the molecular diffusion coefficient (in cm2/s), γ a constant of the gyromagnetic ratio of a proton in (in MHz/tesla), G the field-strength gradient (in G/cm) and TE the inter-echo spacing used in the CPMG sequence. Since no static magnetic gradient field was applied during the CPMG sequence, equation 2-31 can be simplified to the second member of the equation as a function of the pore geometry and surface relaxivity.

2.3.3 NMR petrophysics

Porosity

Porosity is defined as the ratio of the volume of space between the grains of the rocks to the whole bulk volume. In NMR, porosity is directly related to the number of hydrogen atom (protons) present in the sample. The hydrogen atoms are proportional to proton density which corresponds to the initial amplitude of the spin. The initial NMR signal corresponds to the porosity which can be found by equation 2-32 (Wang et al., 2006):

$$\phi=\frac{V_\phi}{V_T}\times100\%=100\times\frac{a.T}{rg.ns.V_T} \qquad \text{Equation 2-32}$$

Where ϕ porosity and V_T is volume of the standard sample, r_g is the receiver gain for the sample, ns is the number of scans used and *a* is the amplitude of the signal from

the tool. Furthermore, through mathematical conversions, the raw NMR signal can be represented in terms of T_2 distribution, and the Maran spectrometer used for the measurements does the conversion through its software. The conversion is not discussed in this research. The total area under the T_2 relaxation time distribution is the total porosity of the sample (Figure 2-10).

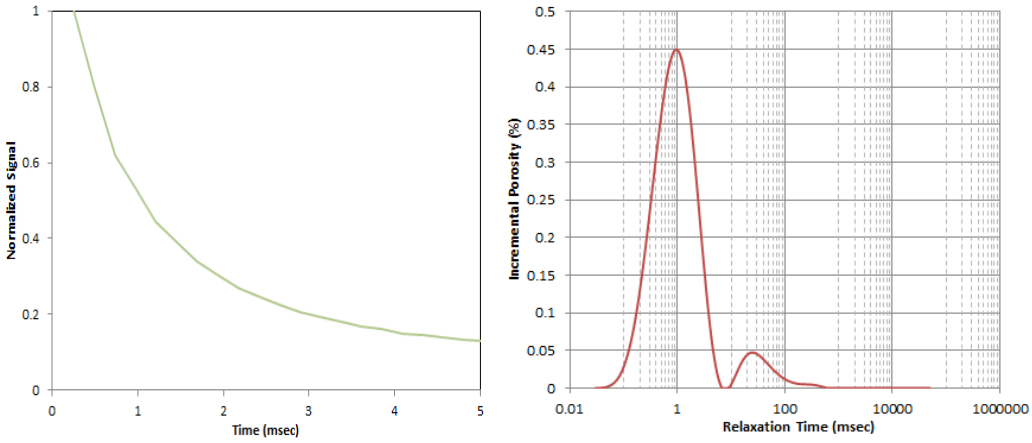

Figure 2-10: (left) raw NMR T_2 signal; (right) converted NMR signal (amplitude) to T_2 relaxation distribution in terms of porosity

Permeability model

Permeability can be measured from NMR measurements using theoretical models such as the Coates equation (Coates et al., 1999).

$$K = \left[\left(\frac{\emptyset}{C}\right)^2 \left(\frac{FFI}{BVI}\right)\right]^2 \qquad \text{Equation 2-33}$$

The Coates model requires defining the free fluid (FFI) and bound fluid (BVI) from the T_2 distribution, i.e. determining the cut-off time. To extract the cut-off, on a commutative NMR signal curve as a function of T_2 relaxation time, the NMR signal is therefore common along a short T_2 range, where the same irreducible water signal is recorded from both hydration states of the sample, until a point of divergence where only the mobile water acts from the saturated sample condition. This point of divergence corresponds to T_2 cut-off (Figure 2-11).

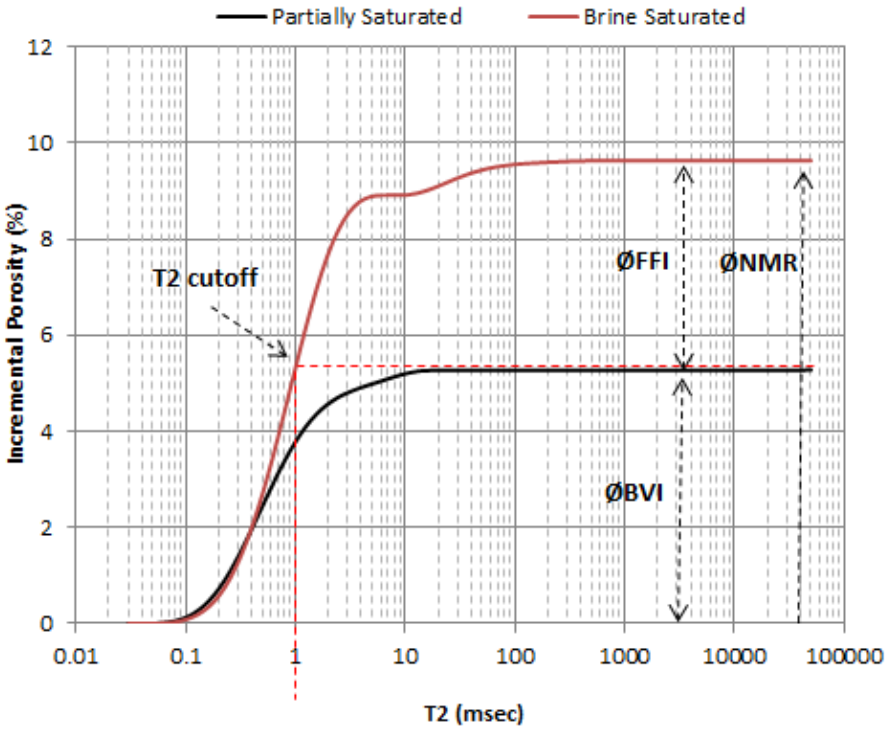

Figure 2-11: Cumulative plot of both partially and brine saturated sample as a function of T_2 relaxation time. This is used to determine the T_2 cut off that is required to define FFI & BVI

2.4 Nitrogen adsorption

2.4.1 Introduction

Pore system characterization is an important step for evaluation of gas shale reservoirs. Therefore it is necessary to use new and more effective techniques to understand the pore structure, gas storage mechanisms and the relationship between pore size and gas storage capacity. The gas is stored in the gas shale reservoirs in the form of free gas and adsorbed gas. The adsorbed gas is the gas which can be attached to the surface of the clay minerals or organic materials.

The low pressure adsorption measurement allows us to understand the pore size distribution (PSD) and study the parameters which control the adsorbed gas capacity, such as surface area and microporosity. Low pressure adsorption measurement has been used extensively in surface chemistry analysis for characterization of porous

materials, and has been adopted for characterization of the nanopores in the shale samples recently (Ross and Bustin, 2009; Kuila and Prasad, 2011; Chalmers et al., 2012)

2.4.2 Analysis Approach

Surface Area

The Brunauer-Emmett-Teller (BET) method is the most widely used procedure for determination of the surface area of porous samples. The basic principle of the method is that the samples are degassed at high temperature then evacuated. The samples are then cooled at 77K and the amount of nitrogen is dosed down. The pressure is then measured when it reaches equilibrium. After the pressure reaches atmospheric pressure, the procedures are repeated again the other way around.

Equivalent surface area is calculated using the BET equation (Brunauer et al., 1940):

$$\frac{1}{W\left(\frac{P}{P_0}-1\right)}=\frac{1}{W_mC}+\frac{C-1}{W_mC}\left(\frac{P}{P_0}\right) \qquad \text{Equation 2-34}$$

where W is the weight of gas adsorbed at a relative pressure P/P_o (where P is the gas vapour pressure in the system and P_0 is the saturation pressure of adsorbent); Wm is the weight of monolayer nitrogen adsorbed to the sample. The C constant is related to the energy of adsorption and its value shows the magnitude of the adsorbent/adsorbate interactions.

A linear plot of $1/[W(P_o/P)-1]$ versus P/P_o using nitrogen as the adsorbate, is typically in the region P/P_o of 0.05-0.35 for microporous materials. The weight of a monolayer of adsorbate W_m can then be obtained from the slope s and intercept i of the BET plot. From equation (2-15), $s=(C-1)/W_mC$) and $i=(1/W_mC)$. Thus combining gives $W_m=(1/s+i)$. The second step in the application of the BET method is the calculation of the surface area. This requires knowledge of the molecular cross-sectional area of the adsorbate molecule. The total surface area St of the sample can be expressed as:

$$S_{BET}=\frac{V_m n_a a_m}{mV_L} \qquad \text{Equation 2-35}$$

where n_a is Avogadro's number ($6.023x10^{23}$ molecules/mol) and a_m is the cross-sectional area occupied by each nitrogen molecule (0.162 nm^2), m is the weight of the sample and V_L the molar volume of nitrogen gas (22414 cm^3).

Isotherms

To gain a better understanding of the porosity and surface area of an adsorbent (rock), construction of isotherms is required. An adsorption isotherm is created when the amount of nitrogen is measured on the surface over a wide range of relative pressure at constant pressure. All isotherms fall into one of the following groups (De Boer, 1958) (Figure 2-12):

Type I: are concave to the P/P_o axis and the amount of adsorbate approaches a limiting value as P/P_o approaches 1. They are commonly related to micropores having small external surface area.

Type II: isotherms are the normal form of isotherm obtained with a nonporous or macroporous adsorbent.

Type III: isotherms are convex to the P/P_o axis over its entire range and are rarely encountered.

Type IV: isotherms are associated with capillary condensation in mesopores, indicated by the steep slope at higher relative pressures.

Type V: isotherms are uncommon, corresponding to the type III, except that pores in the mesopore range are present.

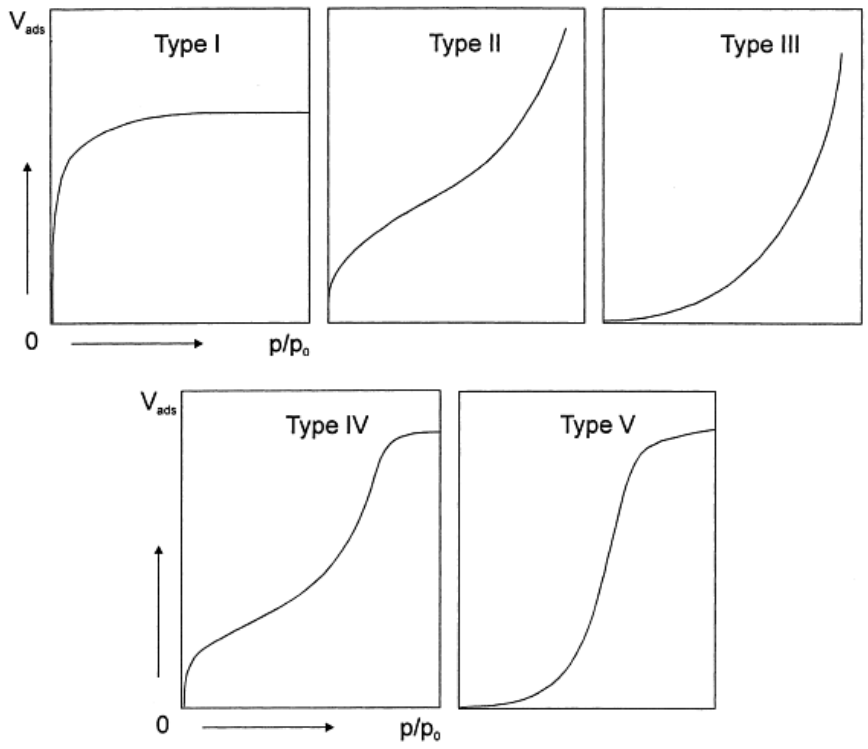

Figure 2-12: Plots of the total amount of nitrogen versus the relative pressure. The various adsorption isotherm types allows better understanding of porosity and surface area of an adsorbent (Brunauer et al., 1940)

Average pore radius

The total pore volume is derived from the amount of vapour adsorbed at a relative pressure close to unity, by assuming that the pores are then filled with liquid adsorbate. The average pore size could be estimated from the total pore volume determined at maximum pressure, by assuming that the pores which would not be filled below a relative pressure of 1 have a negligible contribution to the total pore volume. For example, assuming cylindrical pore geometry, the average pore radius (rp) can be expressed as:

$$r_p = \frac{2V_{ads.}}{S} \qquad \text{Equation 2-36}$$

where Vads. is the total amount of nitrogen adsorbed and S is the surface area (Quantachrome, 2008).

The distribution of pore volume with respect to pore size is called pore size distribution (PSD). Usually the BJH model (Barret et al., 1951) and DH model (Dollimore and Heal, 1964) are used for determining pore size distribution using nitrogen adsorption for the shale layers. The actual pore size in both of these models is calculated using the thickness of the adsorbed layer and the Kelvin equation (Gregg & Sing, 1991):

$$\ln\left(\frac{P}{P_o}\right)=\frac{2\gamma V_m}{RTr_K}\cos\theta \qquad \text{Equation 2-37}$$

where P is the gas vapour pressure, $P_o$is the saturation pressure of adsorbent, γ is the surface tension of nitrogen at its boiling point (77 K), θ is the contact angle between adsorbate (liquid nitrogen) and adsorbent, Vm is the molar volume of liquid nitrogen, R is the gas constant, T is the boiling point of nitrogen (77 K), and r_K is the Kelvin radius of the pore.

The BJH (Barret et al., 1951) and DH (Dollimore and Heal, 1964) models are appropriate for determining mesopore and macropore size distribution; therefore these theories could not give a realistic description of micropore filling because the Kelvin equation is inapplicable for micropores. Thus using them for characterization of microporous materials leads to an underestimation of pore sizes for micropores and even smaller mesopores (Ravikovitch et al., 1998). DFT is a technique that uses modern statistical thermodynamics. It provides a much more accurate approach for pore size analysis and it can be used for PSD determination in micropore scale as well as mesopore. Thus, in this study the DFT model was used for PSD determination because micropores have an important role in the pore structure of the shale layers, and the BJH and DH models could not determine the pores in this interval accurately.

2.5 Focused Ion Beam/Scanning Electron Microscopy

2.5.1 FIB/SEM overview

The application of the Focused Iron Beam (FIB) method includes failure analysis, micro-machining, mask repair, sample preparation for transmission electron microscopy (TEM) and cross sectional imaging through semi-conductor devices.

Also, other applications include sectioning and imaging of powders and particulates, observing the presence of corrosion, nanofabrication & nano-prototyping and many more (Fibics, 2011).

Visualization of core material at the pore scale has been applied positively in the oil & gas industry for many years. The understanding of the internal structure and the geometry of the pore is critical for qualitative and quantitative analysis of the connected andd unconnected pores (Sisk et al., 2010), mineral composition, pore size distribution (Siddiqui et al., 2005), permeability, saturation, gas storage content and absorption capacity of the rock (Lu et al., 1992) and pore types (Heath et al., 2011).

In addition, most research methodologies are based on one type of experiment or a combination of two technologies to understand porous media, such as: X-ray computed tomography scanning to study gas storage and transport in Devonian shales (Lu et al., 1992); NMR to model transport mechanism (Kanj et al., 2009; Osment et al., 1990); nuclear magnetic resonance (NMR) and micro-CT scanning as a validation for pore network models (Talabi et al., 2009); and NMR and X-ray small angling scattering to characterize pore system and flow characteristics (Bustin et al., 2008). Combined methods include: a combination of scanning electron microscopy (SEM) and thin section analyses to determine mineral content; distribution and pore structure of Baker dolomite, Bera sandstone and Indiana limestone samples (Churcher et al., 1991); mercury injection (MICP) and scanning electron microscopy for petro-physical characterisation of shale (Kale et al., 2010a, 2010b); and focused ion beam (FIB) and MICP to compare pore bodies of mudstones (Heath et al., 2011)

2.5.2 Working Principles

The FIB instrument works in a similar way to SEM (Figure 2-13); instead of a beam electron, FIB uses a Ga+ primary ion beam that hits the surface of the sample and sputters a small amount of materials that leaves the surface as either secondary ions (i^+ or i^-) or neutral atoms (n_0). The signal from the sputtered ions or secondary electrons is collected to form an image of the surface of the sample and gives information on the topography and material characteristics (Fibics, 2011).

The main advantage of using an FIB as compared to SEM is that the gallium ion is much heavier than electrons; this allows the interaction between the ion and the

sample to be much more pronounced. The precise location/target to be sputtered (knocked off) on the sample can be achieved. The gallium beam is the most commonly used ion source as opposed to metals such as In, Bi and Au, because of its low melting temperature, low volatility, low vapor pressure and greater stability (Volkert & Minor, 2007).

The system works repetitively; firstly the images are registered and are interpolated normally to the slice (direction) and the SEM beam creates a 2D image of the sample. The ion beam removes a thin layer of material on the surface of the sample, creating a new surface that is aligned with the previous slice, the SEM generates an image again and the process is repeated (Butcher & Lemmen, 2011).

When the instrument is in operation (Volkert & Minor, 2007), the metal (Ga) flows to the tip of the needle — approximately 10um end radius) where it is extracted by field emission. At the needle tip, an electrical field is generated because of the negative potential between the needle and the extraction electrode.

The basic image resolution and micromachining precision is determined by the shape and size of the beam intensity. In general, the smaller the beam diameter the better the resolution achieved (Volkert & Minor, 2007). However, the final resolution is limited by the sputtering and hence the sample type.

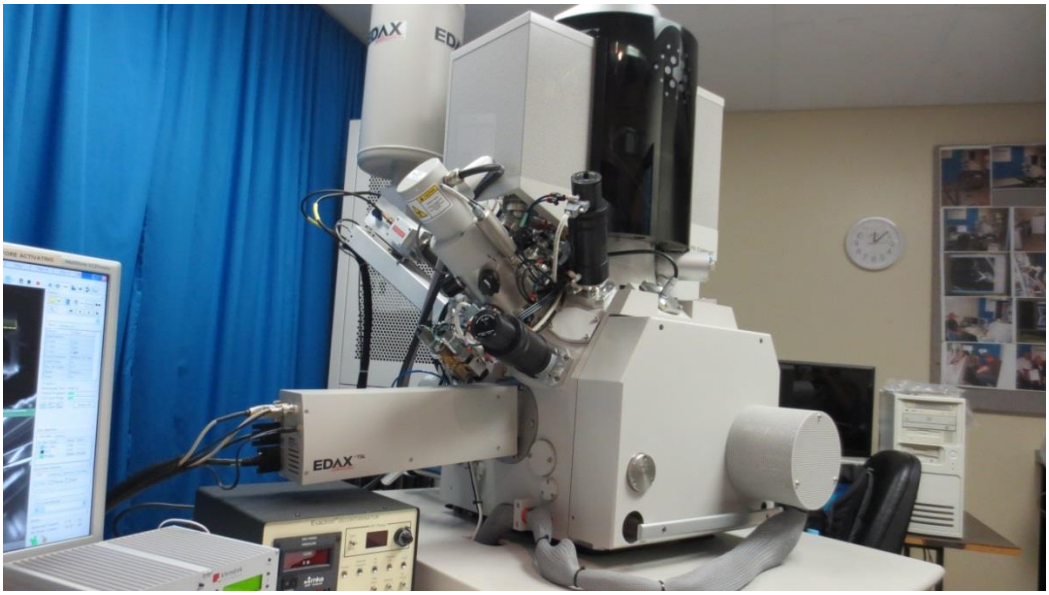

Figure 2-13: FIB/SEM Instrument used in the study to image the pore structure at sub-micron level

2.5.3 FIB/SEM Image Analysis

The general steps involved in pore space image analysis are described as follows. Images are acquired from X-ray CT or FIB/SEM (Figure 2-14). Filtering (Talabi et al., 2008) is applied to the sample to improve the image quality and to reduce/remove noise. For the analysis, image cutting removes any surface patched and removes the outer edges of the sample that might have been mishandled.

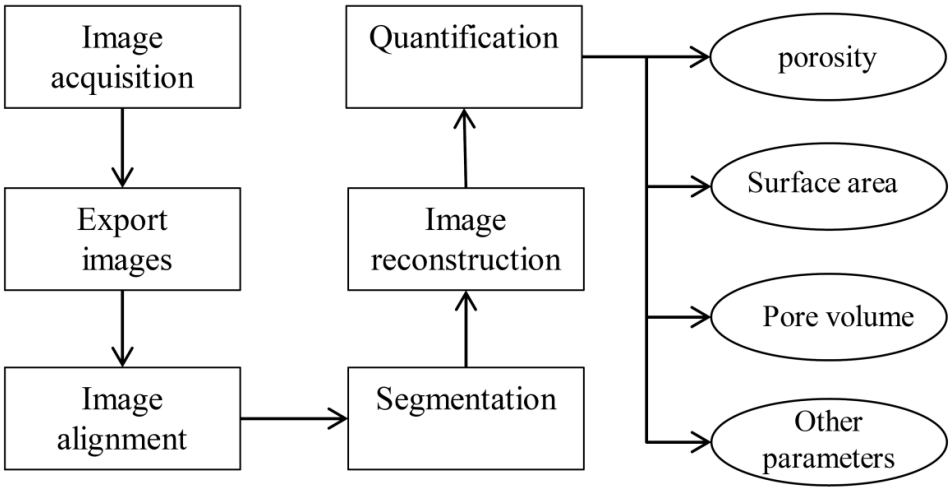

Figure 2-14: Flowchart of general image analysis procedures required to determine various quantifiable pore structure parameters

The objective of segmentation is to simplify and/or alter the representation of an image, to make it more meaningful and easier to analyze. The process involves converting the gray-scale image to a binary image composed of two pixels; black and white (Dougherty & Lotufo, 2003) by categorizing two populations based on their intensity (i.e. diving the images into two phases, pores and solid phase). This is achieved by thresholding, utilizing two coefficients (Prodanovic et al., 2006) T_0 and T_1, of lower and higher attenuation respectively, and any attenuation values between the threshold are based on the estimation. T_0 and T_1 values correspond to phase one or phase two. Once the image is segmented, image analysis can be done.

Porosity can be determined directly from the segmented image, counting the sum of the segmented voxels of the pore space divided by the total image volume.

$$\phi = \frac{\mathrm{V_{segmented\ pores}}}{\mathrm{V_{total\ image}}} \times 100\% \qquad \text{Equation 2-38}$$

The pore surface area is found by counting the number of surface voxels (volume elements) between void and solid in each element. The slice of the CT image would be made up of voxels, hence the volume can be determined by counting the void blocks. In other words, the number of voxels belonging to the body (Boudier, 2014) can be calculated as the sum of 2D areas multiplied by the Z spacing, using image analysis software such as imageJ or Avizo. The 3D sphericity of an object can be assumed as an extension of 2D circularity, and can be determined from the ratio of volume over area. The sphericity, as well as the circularity, is maximal and equals 1 for a sphere:

$$S^3 = \frac{36\pi V^2}{A^3} \qquad \text{Equation 2-39}$$

Where S is the sphericity, V is the volume and A is the area.

In image analysis, the shape factor, a dimensionless quantity, is determined to describe the shape of the element (independent of its size). The measure signifies the degree of deviation from an ideal shape; i.e. for pore space an ideal shape would be a circle where the value of the shape factor would be 1. The shape factor is given by:

$$G = \frac{VL}{A_S^2} \qquad \text{Equation 2-40}$$

where As is the surface area of the pore or throat block, V is the block volume and L is the block length. This is equivalent to

$$G = \frac{A}{P^2} \qquad \text{Equation 2-41}$$

where A is the cross-sectional area and P is the perimeter.

2.6 Pore Size Distribution

2.6.1 Types of Porosity

A porous material (Rouquerol et al., 1994) can be considered as any solid that comprises pores, channels or apertures. In this thesis, the term pore properties refer to both the solid grains (matrix) and the non-solid (pore space), as shown in Figure 1. Care must be taken when describing a porous material as similar terminology could have various meaning. With the aid of Figure 2-15, the pores can be classified according to their accessibility to an exterior fluid.

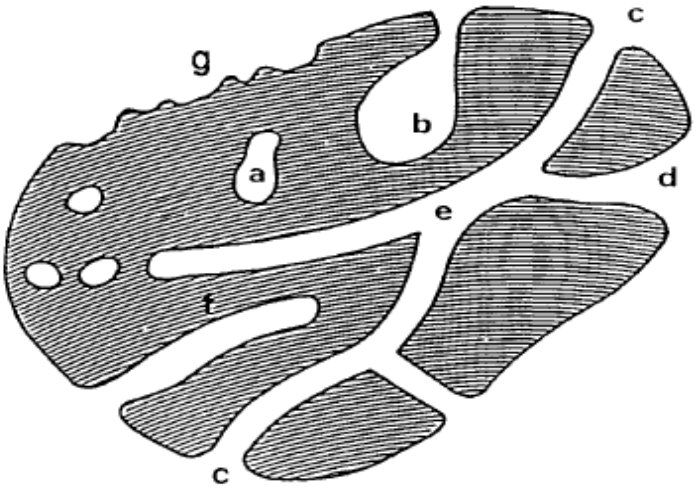

Figure 2-15: Schematic cross-section of a porous material illustrating the various pore shapes (Rouquerol et al., 1994)

In (a), assuming the pore contents, it is completely isolated (i.e. there is no connection to the other pores). (b) (c) (d) (e) and (f) have unbroken conduits and are in connection with the external surface of the body (for this description it can be considered as a grain). However, (f) is connected/opened at one end and closed at the other end, and is described as blind or dead-end. (c) is considered as through pores which are open at both ends. The pores may also be categorized by their shapes: open (d) and dead-end (f) can be assumed as cylindrical, dead-end (b) as ink-bottle shape and (e) slit -shaped. Based on this description, the total porosity is the sum of connected and isolated porosities.

2.6.2 Advantages and disadvantages of PSD methods

In some instances, it is difficult to obtain suitable core plugs for evaluating the petrophysical properties of reservoir rocks. In this situation, MICP and N_2 adsorption tests can be carried out. The advantages of the MICP technique are: it directly measures the pore volume through the mercury volume injected; it requires small rock cuttings or fragments; results are obtained relatively quickly with reasonable accuracy; and very high capillary pressure ranges can be achieved. The measurement does not require a completely symmetrical sample, but is commonly limited to 1 cm^3.

MICP and N_2 are destructive techniques but quite often used as relevant PSD measurements for gas shales (Clarkson et al., 2013). They are intrusion or fluid penetration practices, where mercury is injected into the samples in the former and nitrogen in the latter. MICP is capable of characterizing the PSD in the range of meso-pores (5 nm < pore diameter > 50 nm: intra- and inter-clay) to macro-pores (pore diameter > 50nm: inter-grains and discontinuities) while N_2 relates to pores less than 2 nm. The pore diameter classification in this study is based on IUPAC classification (Rouquerol et al., 1994). The samples must be dry before measurement because the intrusion fluids cannot fill samples containing other liquids. Samples with fine pores like gas shale are difficult to fully degas before intrusion by mercury or nitrogen (Allen, 1997).

The N_2 method also requires crushing the sample into powder to fully wet the surface of the sample, which could affect the original pore structure of the solid matrix. Another inconvenience of the MICP and N_2 methods for evaluating the properties of shale is the occurrence of a double layer (or Stern layer). This layer is directly related to the surface clay-bound water that reduces porosity in pore diameter and pore radius values (i.e. effective porosity) that are strongly bound, and therefore impossible to remove unless the sample is exposed to temperatures >> 100 degree C to evaporate it. Constant surface tension and contact angle values are used with MICP (Allen, 1997) but such constants may be different from one shale to another, due to different wetting intensity of clays and minerals.

NMR is a non-destructive technique that is performed under room conditions. It supposes that the sample is fully or partially water saturated (i.e. in a preserved

condition) for proper porosity assessment and that no mechanical relaxation from in situ stress conditions occurs, which is rarely the case in shales. In contrast with MICP PSD that provides only "connected" pore throats as tube shapes and no pore body sensu-stricto, NMR PSD provides full experimental characterization of pore geometry (Chen & Song, 2002), the size of the pore body behind the throats (Burdine et al.; 1950, Churcher et al.; 1991, Heath et al., 2011) and the isolated pores (e.g. if the sample kept its original fluid).

2.6.3 Pore Size Classification

The word ‘‘size’’ is associated either with diameter, if a pore throat is considered as cylindrical, or with width, if a pore throat is characterized as a thin slot. Generally, characterization of the pore-throat size of a rock sample (Nelson, 2009) requires the choice of (a) a method of measurement, (b) a model for converting the measurement to a dimension, and (c) a parameter to represent the resulting pore size distribution. For instance, MICP uses the Washburn equation to determine a dimension associated with a specific saturation of the invading fluid or an inflection point on a graph of pressure vs. the volume of the invading fluid.

A range of classifications is available in the literature to describe the pore system. In general, they can be categorized based on; petrographic, depositional and hydraulic rock types. Petrographic rock types are geologically classified using image acquisition techniques. The depositional types are explained by their core, categorized by sedimentary structure, composition and sequence stratigraphy that are determined by the depositional environment. Hydraulic rock types are defined in terms of the physical rock property characteristics, such as flow and storage properties, which are controlled by the pore geometry (Rushing et al., 2008a). In this study, the pore size classification (Figure 2-16) has been adopted from the International Union of Pure and Applied Chemistry (IUPAC), which was established by Rouquerol et al. (1994). The classification is based on three groups: micropores which include pores less than 2 nm diameter, mesopores which comprise pores with diameters between 2 and 50 nm, and macropores which include pores with diameters larger than 50 nm.

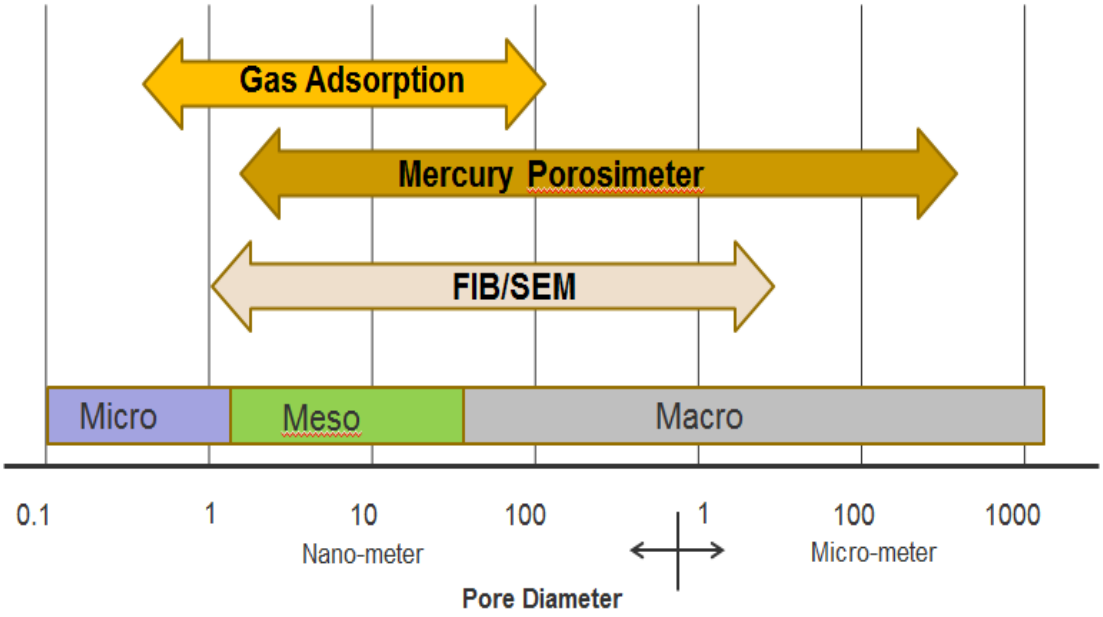

Figure 2-16: Pore size scale based on the methodology utilized to characterize the pore size distribution. The values are based on IUPAC Classification; micro pores < 2nm diameter, meso pores 2nm – 50nm diameter and macro pores > 50nm diameter.

2.6.4 Interchanging MICP with NMR data

In general, geological mapping and petrophysical, core and fluid analyses are carried out in order to estimate the volume of hydrocarbons in a particular field. Key information for successful volume estimations from these analyses involves the determination of fluid pressure regimes that enable recognition of the various fluid contacts and especially the water saturation. The fluid distribution estimation needs to take into account the interaction between the rock and the fluid in this study. Such complex interactions can be understood in terms of capillary pressure and pore geometry. Thus, pore volume information such as porosity and saturation act as inputs to volumetric estimates of hydrocarbon.

Porosity is a measure of the free space in the rock. That is, the total pore volume and total bulk volume ratio, known as absolute porosity (Ø). Furthermore, it is important to know about the pores that are interconnected and influence fluid flow. This type of porosity is known as the effective porosity: the ratio of interconnected pore volume

and the total bulk volume ($Ø_e$). Various methods are available to measure porosity, including MICP and NMR.

In fact, there is more than one type of fluid in the pore space in any given reservoir. To be able to know the fractions of each type of fluid, fluid saturation calculations are necessary, defined as the ratio of the total fluid volume (gas, oil or water) divided by the pore volume. This fluid saturation certainly cannot be reduced to 0% when displaced by another fluid. It is mainly controlled by the capillary pressure and gravity. The attraction (surface tension) that occurs between the rock surface and the fluids is also one of the reasons why saturation cannot be 0. Assuming the displaced fluid is water, the remaining water that has not been displaced by the displacing fluid is known as connate water, sometimes called irreducible water saturation (S_{wi}). Generally, irreducible water saturation is obtained from capillary pressure measurements such as MICP.

Porosity provides information about what volume of hydrocarbons can be stored, and saturation tells us the amount of each fluid present in the system. One needs to know the rate at which the fluids can flow, the permeability (k) and if it is mainly controlled by the pore geometry. MICP curves can reveal the pore throat size distribution and NMR data can indicate the pore body size of a rock sample.

It is believed that it is possible to integrate mercury injection capillary pressure (MICP) data with nuclear magnetic resonance (NMR) data. Through the estimation of the surface relaxivity parameter, NMR T_2 equivalent capillary pressure and MICP equivalent T_2 can be estimated. Also, obtaining permeability estimates by using theoretical models that incorporate water saturation parameters of gas shale samples' T_2 relaxation times can be illustrated in terms of size or radius, as equation 2-9 suggests. (Granier, 2003; Howard, 1991) introduced a graphical approach and established the following:

$$MICP_{peak}value = \rho_e(T_{2\,peak}value) \rightarrow \rho_e = \frac{MCIP_{peak}value}{T_{2\,peak}value} \qquad \text{Equation 2-42}$$

Where ρ_e is surface relaxivity (um/sec) and the peaks correspond to the peak pore throat radius and T_2 relaxation time. Figure 2-17 shows a graphic representation of NMR correlated with MICP.

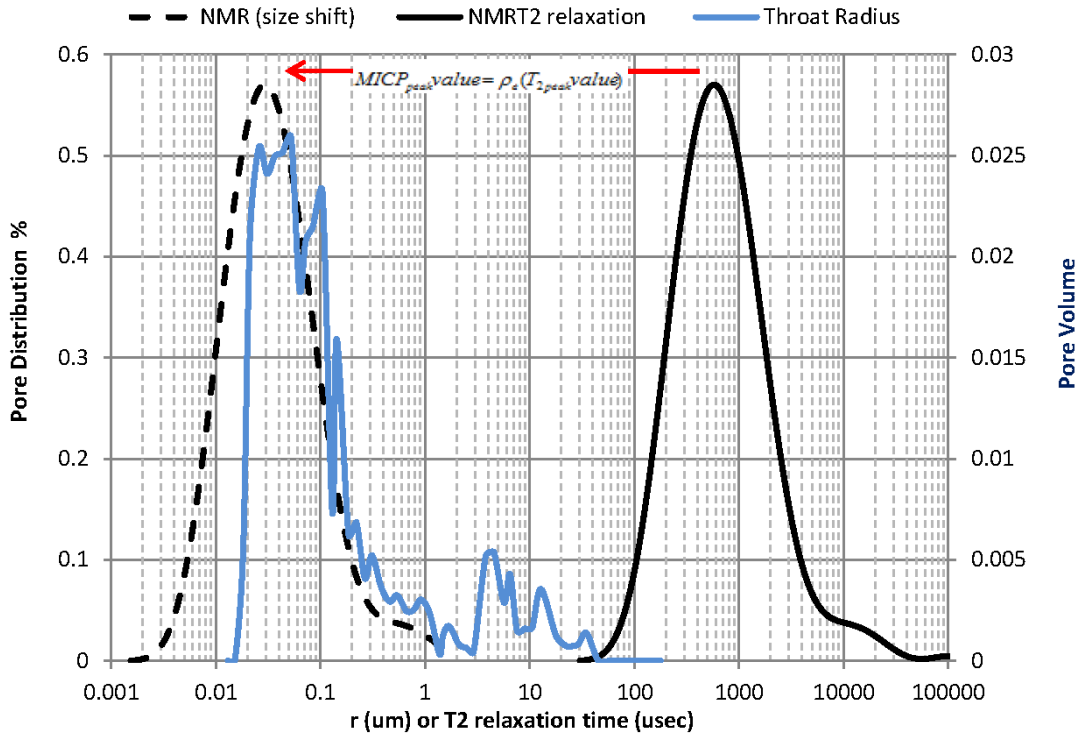

Figure 2-17: Graphical representation of correlating NMR T_2 relaxation time to MICP pore size thru the estimation of surface relaxivity

Marchall et al.'s (1995) results showed surface relaxivity ranging from 1 to 25 μm/msec, with the lowest, ρ_2, being those samples with the lowest porosity (6.4%) and permeability (0.287 md); these are mainly sandstone and limestone. Volokitin et al. (1999) developed a method to convert T_2 distributions to capillary pressure of sandstones at any water saturation, and found a constant of 3 $T_2=3/P_c$ for sandstones. Zhi-Qiang et al. (2005) proposed the elimination of the bound water T_2 contribution and used free water to construct capillary pressure curves.

3. CHAPTER 3: GEOLOGICAL DESCRIPTION

3.1 Perth Basin

Australia's first commercial gas shale region was most likely to be in the northern Perth Basin, and the gas shale volumes for the onshore Perth basin highlighted relate to the Carynginia (PCM) and Kockatea (PKM) Formations. The Perth Basin is a north–south elongated trough along the south-western coast of Western Australia, about 172,300 sq km in area (Kuuskraa et al., 2011), containing a Silurian to Pleistocene sedimentary succession (Figure 3-1). About one half of the Basin is located onshore and extends from the south coastline to near the Murchison River, demarcated by the Yilgarn Craton to the east and the coast to the west, and covering an area approximately 220 km long and 90 km wide. Within this area are the Dongara Terrace Dandaragan Trough, Beagle Ridge and a number of small, newly recognized sub-basins.

The Perth Basin is a simple North West trending half-graben structure which allows shale gas development. The Bunbury and Dandaragan Troughs are two vast sedimentary sub-basins covering more than half of the basin, with nearly 33,400 sq m of on-shore area, split by the Harvey Ridge (Kuuskraa et al., 2011). The structure of the Perth Basin is complex, formed through the parting of Australia and Greater India in the Permian to Early Cretaceous era (Mory & Iasky, 1996). It contains an important onshore factor, and ranges offshore to the edge of the mainland crust in water depths of up to 4500 m. This Permian basin extends to a depth up to 15 km between the north and south trending rift basins of the Bunbury aquarium, Dandaragan, and along the western edge of Yilgarn Craton. The Abrolhos sub-basin characterizes a north-western division of the Permian rift organization beside the south-western boundary of the Northampton complex, which is divided from the Dandaragan Trough by a high point within the basin marked by the Beagle Ridge, Dongara Terrace and Greenough Shelf. The large syncline of the Dandaragan trough in the north of the Perth basin comprises greater thickness and depth, and more potential for gas shale formation.

The PCM Formation is predominantly inter-bedded siltstone, sandstone, and coarse-grained quartz sandstone, with thin beds of a fine conglomerate with minor shale

above the Irwin River Coal Measures (Figure 3-2). Kuuskraa et al. (2011) reported that the rich organic shale of the PCM formation has a thickness of approximately 240 to 330 metres, with deeper marine shale in the base of the unit, and siltstone and sandstone inter-bedded layers.

The PKM Shale is located at the Lower Triassic; it is considered to be major oil source-rock and seal in the basin (Mory & Iasky, 1996). It has a maximum thickness of 1,060 m in Woolmulla 1 (Kuuskraa et al., 2011). Moreover, several elements are contained in the PKM shale. For example, the part of the unit with the most likely sources is basal shale, rich in sapropel, with an average TOC of 2.0%, associated with an overall TOC typical for the unit of 0.8%, and type II kerogen in its mature stage for generating hydrocarbon.

3.2 Regional Stratigraphy

The stratigraphy and elements of the petroleum system in the Perth Basin vary greatly according to the tectonic development of the basin from north to south (Figure 3-2). The initial cracking established a series of early Permian Triassic Depocentres and marine siliciclastic rocks with slight carbonate and coal deposits in the north, while in the south, fluvial and coal deposits prevailed. Associated with these deposits, the Permian Rift sag of the early Triassic age has a main petroleum structure in the North Perth Basin, especially in the PKM shale rock, which is a significant source of oil and seals the underlying regional reservoirs (Mory & Iasky, 1996).

Furthermore, the Perth Basin, at another early stage of rifting in the Late Triassic and Jurassic periods, is associated with deposits of fluvial and deltaic rock on a large scale, counting a series of thick siliciclastic and coal layers that topped the Central Jurassic marine shale ‘Cadda Formation’ in the North Perth Basin. These early layers of internal Jurassic formation are proven from the second petroleum system in the North Perth Basin of a certain system. This system is associated with the final rift stage of disintegration in the Middle Jurassic to Early Cretaceous periods, with deposits of Siliciclastic fluvial and marine layers such as the Parmelia and Warnbro groups, which make up the main oil system in the Vlaming sub-basin. It is uncertain whether these are connected with the petroleum system elements in the Zeewyck

sub-basin. However, they may contain a Middle Jurassic to Cretaceous basis, because of the rocks' early age.

Late Cretaceous and Tertiary sedimentations have fallen under unchanging conditions, and negative margins have produced a thin cover of mainly marine carbonates. Potential traps contain tilted block faults, anticlines, compressional rollovers and structural/stratigraphic traps. In summary, the PKM formation presents three main successions in the stratigraphic column of the Perth Basin. Firstly, the lower Permian argillaceous to deltaic rocks, which is seen as potential PCM shale. Secondly, continental shoreline siliclastics to shelf carbonate of the Upper Permian era. And finally, the Triassic to the lower cretaceous formation, composed of shallow to non-marine siliclastics, represented by the potential PKM shale (Mory et al., 1996).

Figure 3-1: Map of location and shale prospective area of the Perth Basin, modified from (HIS, 2014)

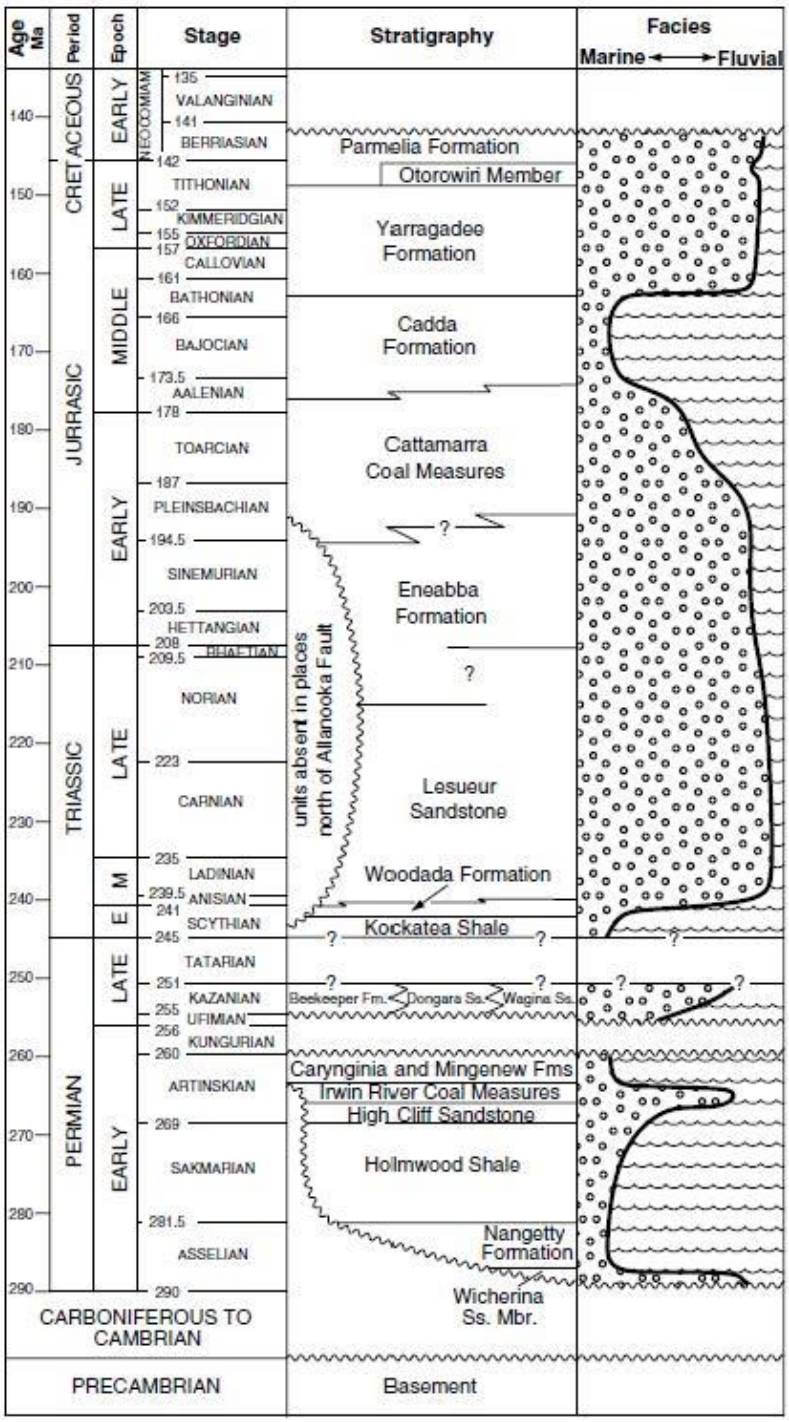

Figure 3-2: Regional stratigraphy of the Perth Basin (Mory & Iasky, 1996)

3.3 Sample Collection

The samples originate from the prospective part of the Northern Perth Basin. Three gas shale formations have been sampled in this study; Carynginia (PCM), Kockatea (PKM) and CCM shale formations. The sample collection and sequence of laboratory experiments conducted are shown in Table 3-1.

Table 3-1: Laboratory methods applied on the sample collection

Formation	Sample Num.	Depth (m)	XRD	Rock eval	MICP	N_2	NMR	SEM
PCM	1	1618	x	x	x			
	2	1614	x	x	x			
	3	400.8		x	x			
	4	2650		x	x			
	5	3771	x	x	x			
	6	3792	x	x	x			
	7	2294		x	x			
	8	2780	x	x	x	x	x	x
	9	2782			x	x	x	x
	10	2790			x		x	
	11	2817	x	x		x		
	12	2825			x	x	x	
	13	2794	x		x	x	x	
	14	2806	x	x	x	x	x	x
	15	2813	x	x		x	x	
	16	2831	x	x		x		x
CCM	17	1947	x		x	x	x	
	18	1246	x		x	x	x	x
	19	1384	x		x	x		
	20	1152	x		x	x	x	x
	21	1160	x		x	x	x	
	22	1650	x			x		x
	23	1454	x		x	x	x	
	24	1410	x		x	x	x	
	25	1855	x		x	x	x	
	26	1436	x		x	x	x	
	27	1949	x		x	x	x	
PKM	28	3793			x			x
	29	3799			x			x
	30	3800	x	x	x			
	31	3793	x	x	x			

3.4 Mineral composition

Bulk X-ray diffraction (XRD) analysis was performed on 23 samples, using a Siemens D500 automated powder diffractometer to characterize their mineral composition and content. The samples were first cleaned of observable contaminants and disaggregated in a mortar with a pestle. A split of each sample was then transferred to distilled water and pulverized, using a McCrone micronizing mill. The resultant powder was dried, disaggregated, and packed into a metal sample holder to produce random whole-rock mounts. A separate split of each sample was dispersed in distilled water using a sonic probe. The suspensions were then size fractionated with a centrifuge to isolate clay-size (<4 micron equivalent spherical diameter) materials for a separate clay mount. The suspensions were then vacuum deposited on nylon membrane filters to produce oriented clay mineral mounts. The clay mineral mounts were attached to glass slides and exposed to ethylene glycol vapour for approximately 12 hours.

The XRD results show that all the gas shale collections are siliceous matrix dominated, with the highest quartz content in the CCM and PCM formations compared to PKM, at 53.28%, 36.75% and 19.4% respectively (Figure 3-3). Formations CCM and PCM also record occurrence of K-feldspars while PKM is rich in pyrite. The remaining mineral contents are clay minerals; formations PCMand PKM are mostly composed of mixed Illite/Smectite, with averages of 15.5% and 26.4% respectively, while formation CCM exhibits a high presence of Kaolinite of approximately 20%, and about 6% mixed Illite/Smectite. Detailed XRD results are shown in Appendix 1.

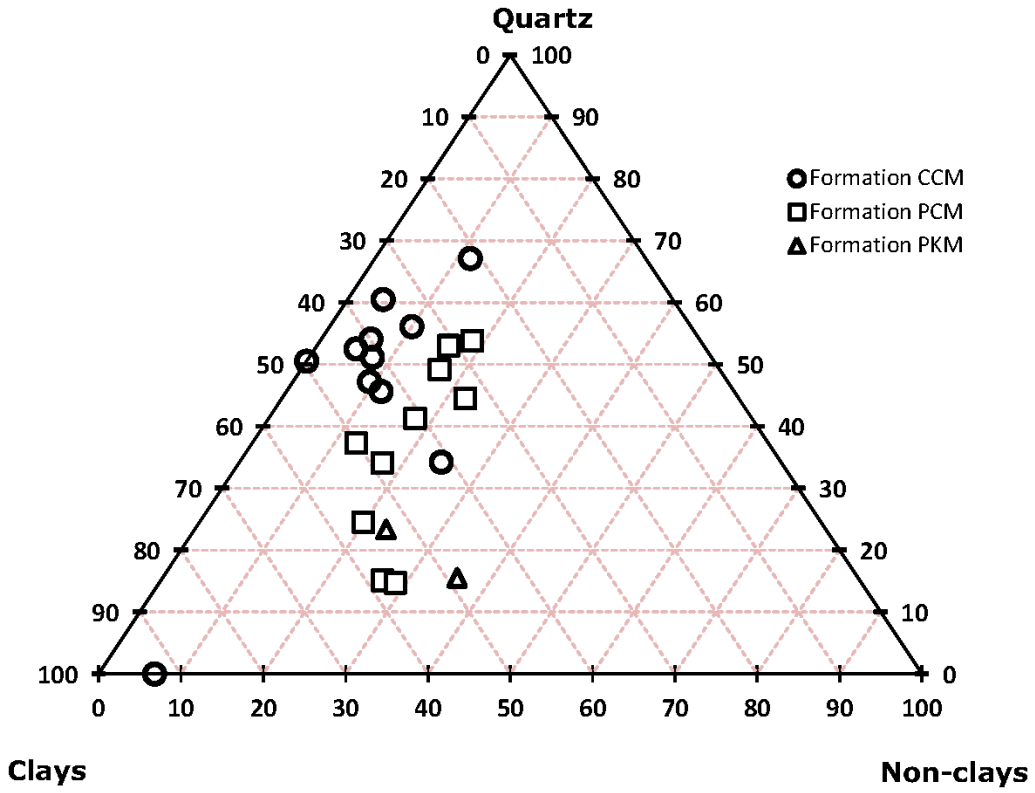

Figure 3-3: Ternary plot of the average weight percentage of mineral composition of the CCM, PCM and PKM formations

4. CHAPTER 4: EXPERIMENTAL RESULTS

4.1 Pore Size Distribution from MICP Experiments

A Micrometrics Autopore IV Porosimeter was used to record the volume of injected mercury at every increasing pressure step on each of the dry shale offcuts. The capillary pressure curve of each tested sample summarizes the relationship between the volume of mercury intrusion and the pressure applied on the sample at different stages of increasing pressure. Mercury saturation started at low pressure, entering the large pores, and progressively invaded smaller and smaller pores as the pressure increased. Most of the samples collected exhibited 100% mercury saturation, close to 60,000 psi (413 MPa) and close to the instrument's testing limits (i.e. 3 nm pore throat diameter). Four samples (20, 21, 23 and 24) did not reach saturation beyond 60,000 psi. These special samples also show a distinctive profile at low pressure. Indeed, they recorded a much lower entry pressure (< 200 psi) starting to invade their pore structures, while the other samples needed an entry pressure that is an order higher (> 1000 psi) (Figures 4-1 to 4-3). The individual capillary pressure curves for each sample is in Appendix 2.

PCM and PKM samples recorded a porosity range of 3 to 7.7%, with a questionable sample 4 showing up to 13.8% (Table 4-1). CCM samples have higher porosity values compared to PCM and PKM, ranging from 4.2 to 9%. The general modal pore throat radius size shows PKM at 3 nm, smaller than PCM which has values around 6 ± 2 nm (Figures 4-5 to 4-7). More specifically, pore throat distribution reveals a second minor population in PKM that have a pore throat size > 1 µm that is easily invaded by mercury injection at low pressure. If all the PCM samples record similar porosities around 3.2 %, differences appear in their pore throat sizes. The samples 1 and 2 have the smallest pore throat at 4.7 nm, with low MICP permeability at around 144 nD, while the other samples are > 6 nm, with twice as much MICP permeability at 238 nD.

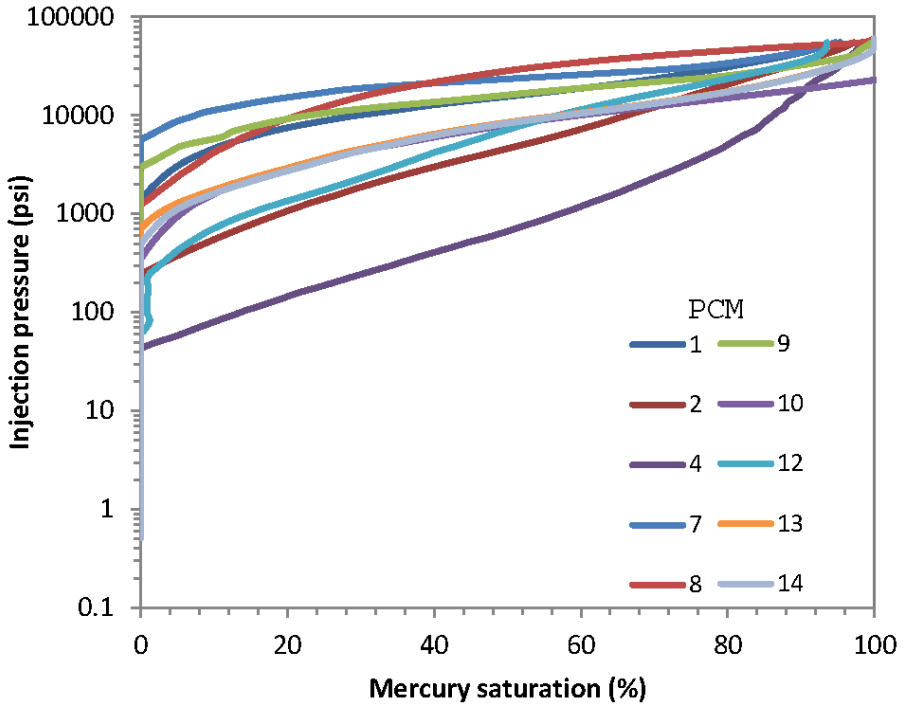

Figure 4-1: MICP results from PCM: mercury injection pressure as a function of mercury saturation. The samples reached 100% mercury saturation close to the instrument testing limits (i.e. 60,000 psi)

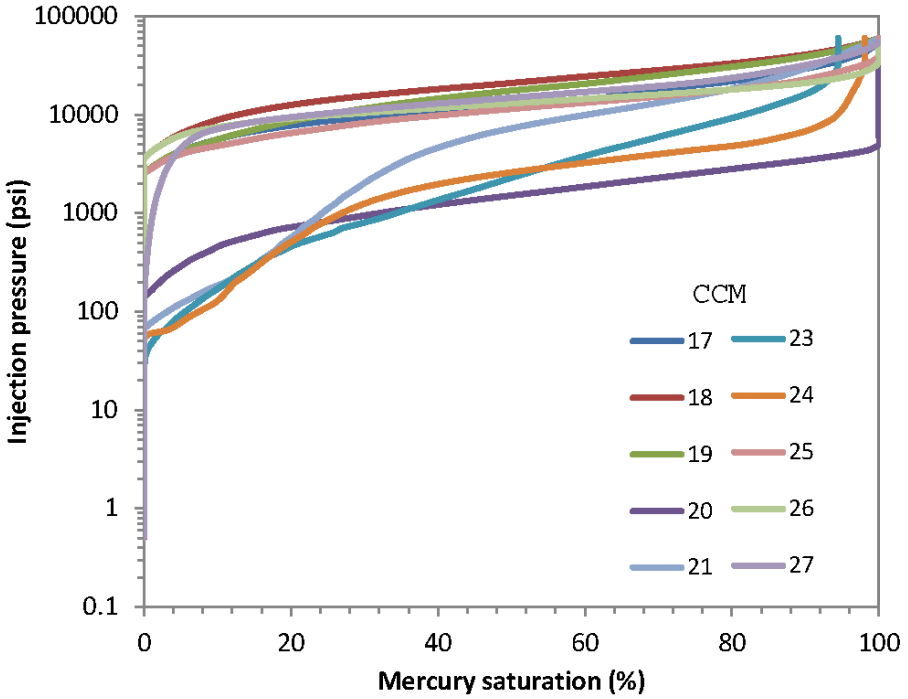

Figure 4-2: MICP results from CCM: mercury injection pressure as a function of mercury saturation. Most of the samples reached instrument testing limit except samples 20, 21, 23 & 24.

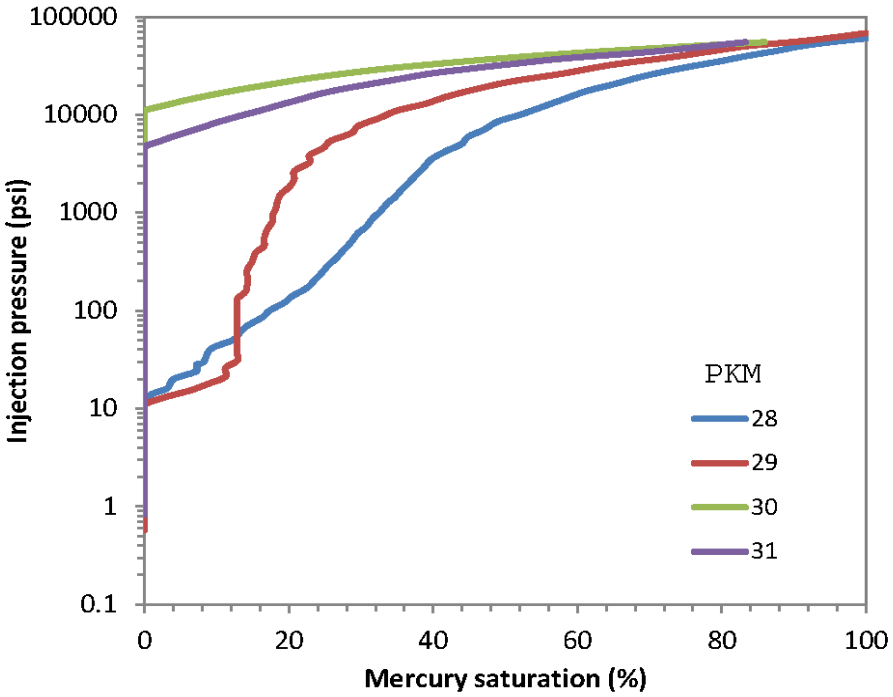

Figure 4-3: MICP results from PKM: mercury injection pressure as a function of mercury saturation. The samples reached 100% mercury saturation.

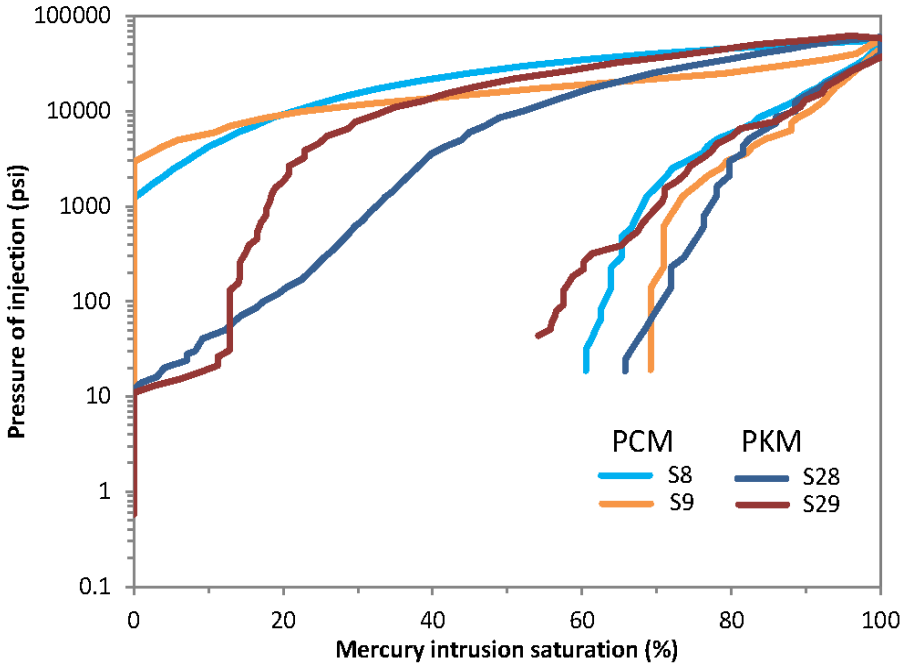

Figure 4-4: MICP injection-withdrawal capillary curves on selected samples 8, 9, 28 and 29. The non-wetting phase fails to completely discharge from the system.

The mercury withdrawal tests on samples 8, 9, 28 and 29 (Figure 4-4) show that the non-wetting phase (mercury) fails to completely discharge from the system down to 10 psi mercury pressure. It is apparent that about 50-70% of the mercury is still trapped in the pore network. Several reasons can be proposed to explain such fluid trapping:

1) the pore structure has been altered or partly destroyed by the high pressure applied during injection, inducing new inter-particle pores (pores between the grains or grain discontinuities) and cracks that caused the blockage;
2) the entrapment of mercury could be due to kinetic effects and surface chemistry of the porous media under capillary and/or electrical forces. The measured bulk porosity from MICP takes into account these newly introduced pores in the calculation of porosity. This type of phenomenon is also found in the literature (Giesche, 2006; Quantachrome; Yao & Liu, 2012);
3) pore geometry and surface rugosity enhances fluid trapping inducing strong capillary forces on the fluid.

Table 4-1: Supplement data extracted from MICP

Formation	Sample ID	Porosity MICP (%)	Peak Radius (um)	Threshold Pressure (psi)
PCM	1	6.2	0.007	1394
	2	7.7	0.03	246
	4	13.8	0.2	45
	7	5.7	0.005	5701
	8	3.78	0.005	6196
	9	3.05	0.005	5783
	10	3.17	0.007	2377
	12	3.03	0.006	680
	13	3.54	0.008	1795
	14	3.57	0.007	1701
CCM	17	7.22	0.005	6115
	18	8.43	0.003	10027
	19	6.52	0.004	7347
	20	8.5	0.026	469
	21	9.02	0.008	1259
	23	8.08	0.057	218
	24	8.14	0.021	1019
	25	4.18	0.006	4460
	26	7.41	0.006	6725
	27	6.98	0.005	5895
PKM	28	2.87	0.004	1355
	29	6.79	0.003	5261
	30	2.4	0.002	11585
	31	2.4	0.003	4942

Excluding samples 3, 4, 20, 23 and 24, an average modal pore throat radius for the whole data set was found to be around 5.2 ± 1.8 nm, with some differences between each formation, at 6 nm for PCM, > 5 nm for CCM, and > 3 nm for PKM (Figures 4-5 to 4-7). The five samples were excluded from the average calculation because they anonymously showed pore throat sizes > 20nm. For all the three formations, the meso-pores ranged from 62 to 75% of the total volume and the remaining 25% to 38% belong to the macro-pore volumes (Table 4-2).

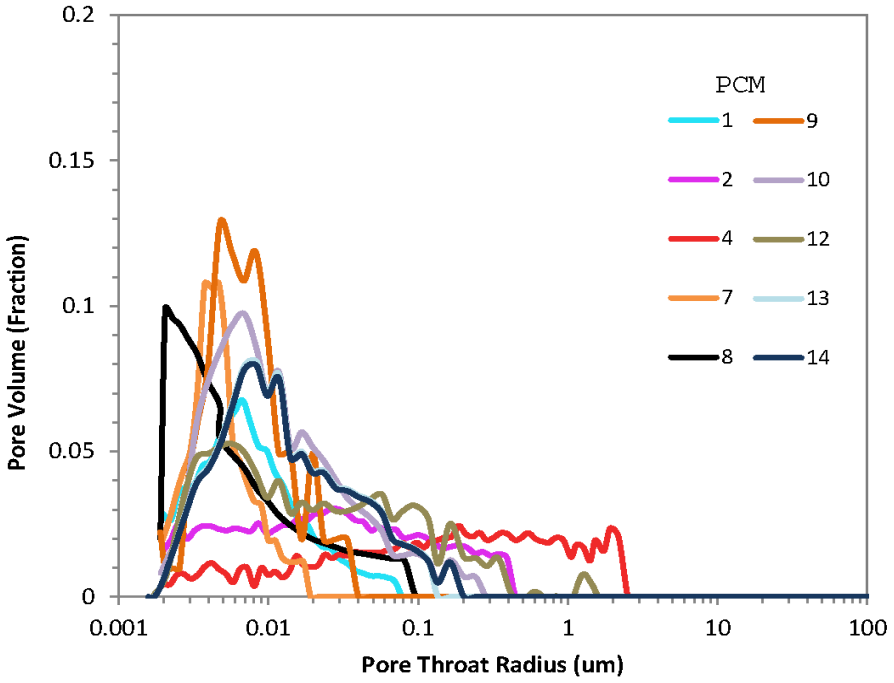

Figure 4-5: Converted previous capillary pressure curves into equivalent pore throat radius as a function of the pore volume fraction or porosity for PCM samples.

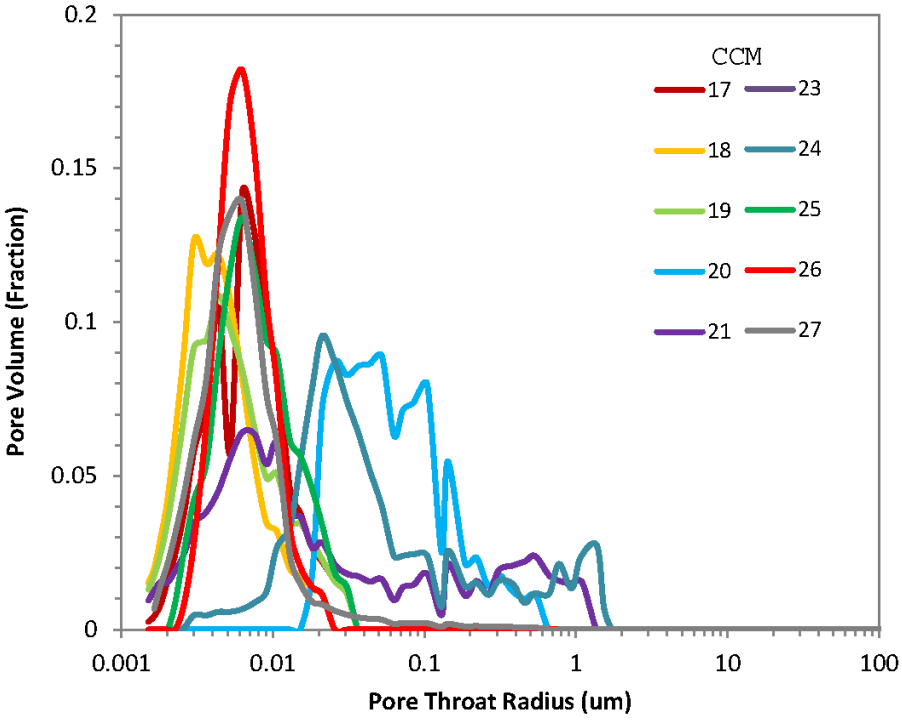

Figure 4-6: Converted previous capillary pressure curves into equivalent pore throat radius as a function of the pore volume fraction or porosity for CCM samples.

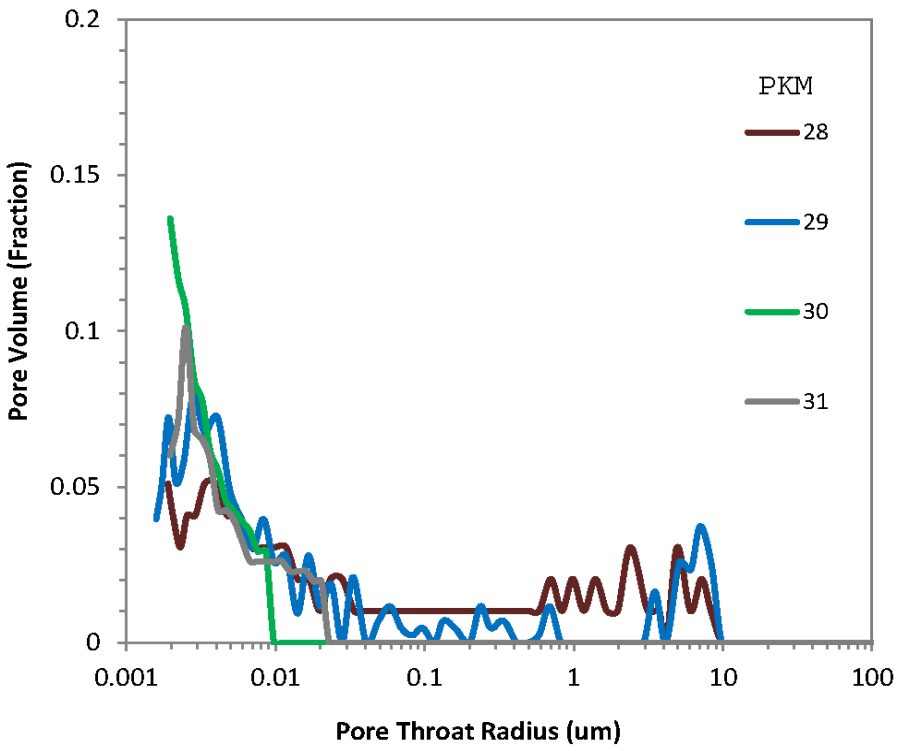

Figure 4-7: Converted previous capillary pressure curves into equivalent pore throat radius as a function of the pore volume fraction or porosity for PKM samples.

There is no relationship between MICP porosity and the modal pore throat radius (Figure 4-8). However, a general trend exerts an expected relationship between the entry pressure and the modal pore throat radius. The previously excluded samples (3, 4, 20, 23 & 24) also exhibit a higher macro-porosity contribution obtained from pore throat radius > 50 nm (Table 4-2), based on the IUPAC classification. Note that micro-porosity (< 2 nm pore size following IUPAC) is not achievable by MICP method.

Table 4-2: MICP pore volume percentages based on IUPAC classification from the full sample collection

						Percentage of Pore Volume	
Formation	**Sample ID**	**Porosity (%)**	**Peak Radius (um)**	**Median diameter by volume (um)**	**Threshold Pressure (psi)**	**Meso-pores**	**Macro-pores**
PCM	1	6.2	0.007	0.01	1394	93	7
	2	7.7	0.03	0.05	246	51	49
	4	13.8	0.2	0.32	45	21	79
	7	5.7	0.005	0.01	5701	>95	0
	8	3.78	0.005	0.01	6196	83	17
	9	3.05	0.005	0.02	5783	85	15
	10	3.17	0.007	0.01	2377	68	32
	12	3.03	0.006	0.08	680	45	55
	13	3.54	0.008	0.03	1795	63	37
	14	3.57	0.007	0.03	1701	64	36
CCM	17	7.22	0.005	0.02	6115	86	14
	18	8.43	0.003	0.01	10027	88	12
	19	6.52	0.004	0.01	7347	86	14
	20	8.5	0.026	0.15	469	15	85
	21	9.02	0.008	0.03	1259	59	41
	23	8.08	0.057	0.12	218	38	62
	24	8.14	0.021	0.11	1019	34	66
	25	4.18	0.006	0.02	4460	80	20
	26	7.41	0.006	0.01	6725	91	9
	27	6.98	0.005	0.01	5895	90	10
PKM	28	2.87	0.004	0.06	1355	50	50
	29	6.79	0.003	0.04	5261	52	48
	30	2.4	0.002	0.01	11585	>95	0
	31	2.4	0.003	0.01	4942	>95	0

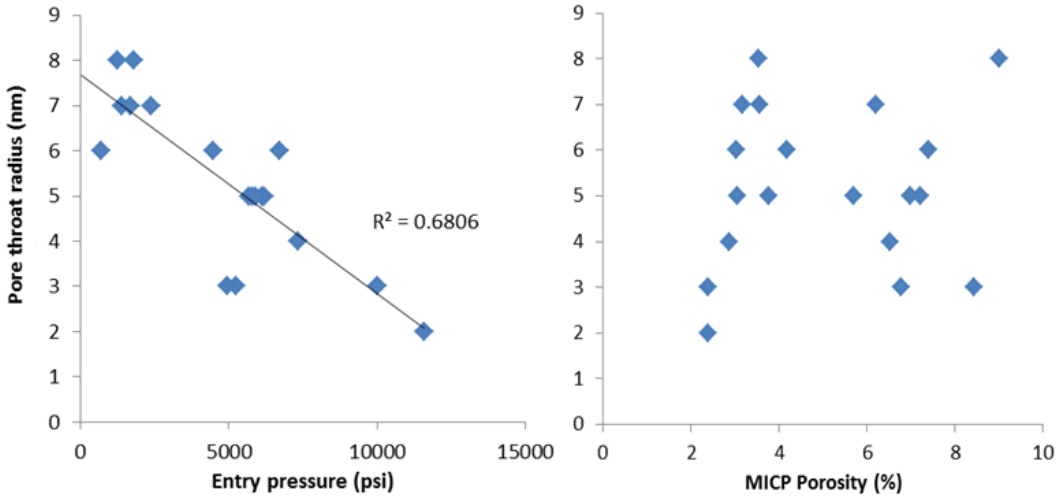

Figure 4-8: (left) A general trend exerts an expected relationship between the pore throat radius and the entry pressure, (right) No relationship between the pore throat radius and porosity

4.2 Nuclear Magnetic Resonance T_2 Relaxation Time

Only T_2 relaxation time was conducted on partially saturated and brine saturated core-plugs (1.5 inch diameter and 4 to 8 cm long), using a low field Maran Ultra-Spectrometer 2 MHz with a Carr-Purcell-Meiboom-Gill (CPMG) spin-echo pulse sequence; more details on the settings and procedure are described in Josh et al. (2012).

The core-plugs were first measured as received (i.e. partially saturated) before performing injection under a hydrostatic pressure of 3.5 MPa of brine (20 g/l KCl) over several days to re-saturate the core plugs and repeat NMR acquisition (Figure 4-9). Prior to weighing, the excess fluid on the surface of the core plug was removed by rolling the sample on white printing paper twice along the landscape length. White paper was used opposing to paper towel because the paper towel could draw more of the fluids in the pores close to the surface of the plugs.

The plugs were then wrapped tightly with a transparent plastic wrap to keep the fluids intact with the plugs and to prevent the fluid spreading through the container. The Maran was calibrated with a known volume of doped water before any core-plug measurements to compute the water content in the core plugs and so their porosity.

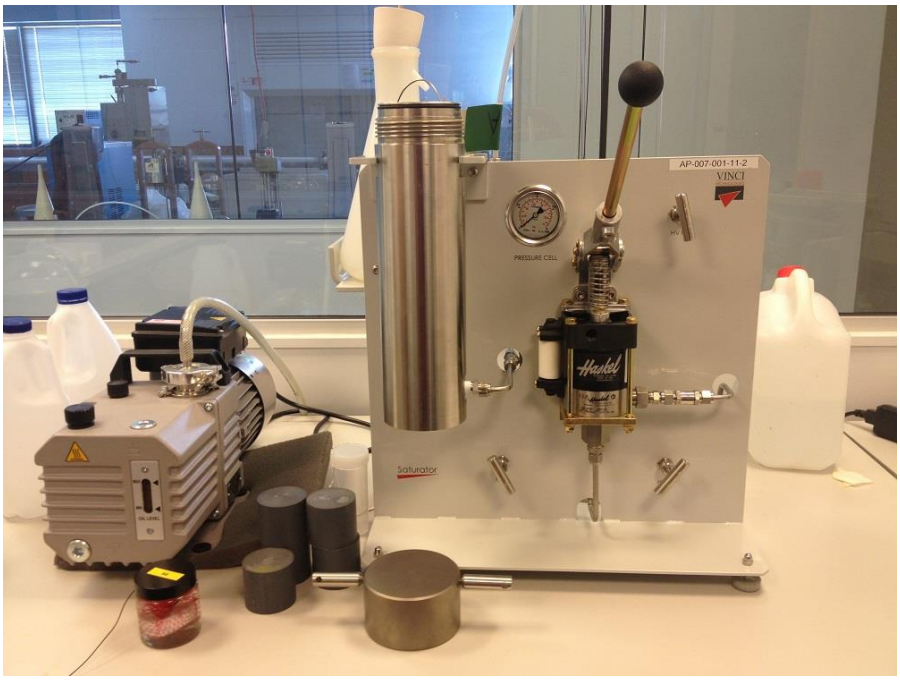

Figure 4-9: Instrument used to saturate the core plugs under 3.5 MPa hydrostatic pressure

In NMR, porosity is directly related to the amount of hydrogen atom (protons) present in the sample. The hydrogen atoms are proportional to proton density and correspond to the initial amplitude of the spin (Figures. 4-10 to 4-13). Under partially-saturated conditions, the average porosity was found to be 4 ± 1.3%. The samples have systematic mono-modal distribution with a relaxation time (T_2) centred around 0.35 ± 0.03 ms (Figures 4-14 and 4-15 and Table 4-3).

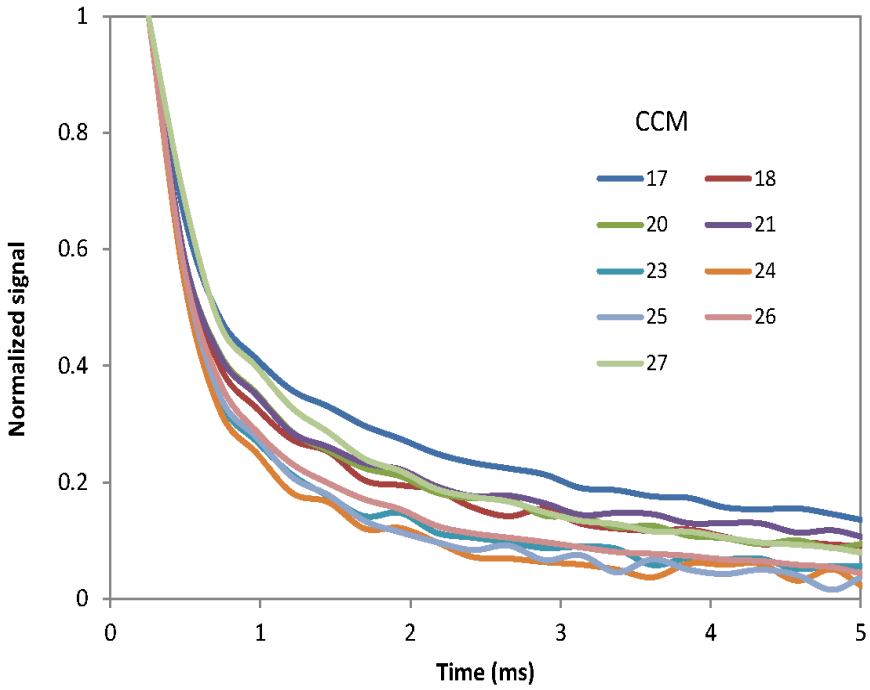

Figure 4-10: Raw NMR signals for partially saturated CCM samples

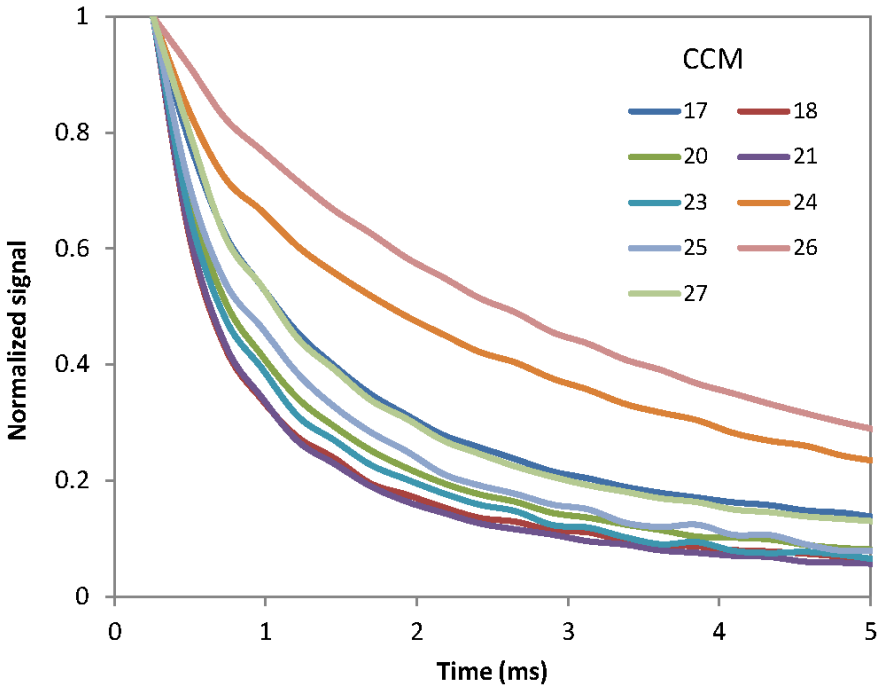

Figure 4-11: Raw NMR signals for saturated CCM samples

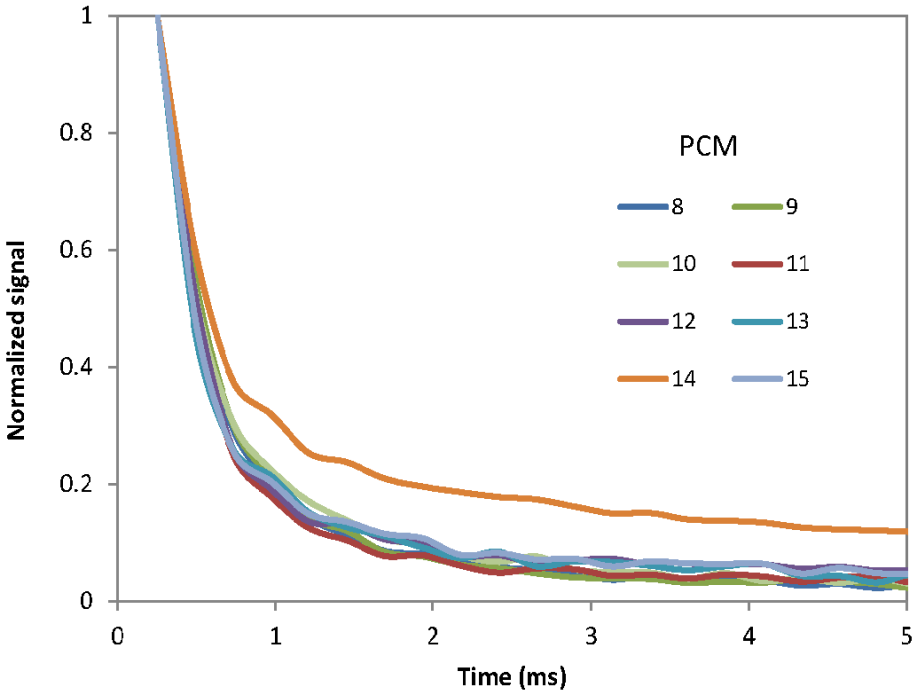

Figure 4-12: Raw NMR signals for partially saturated PCM samples

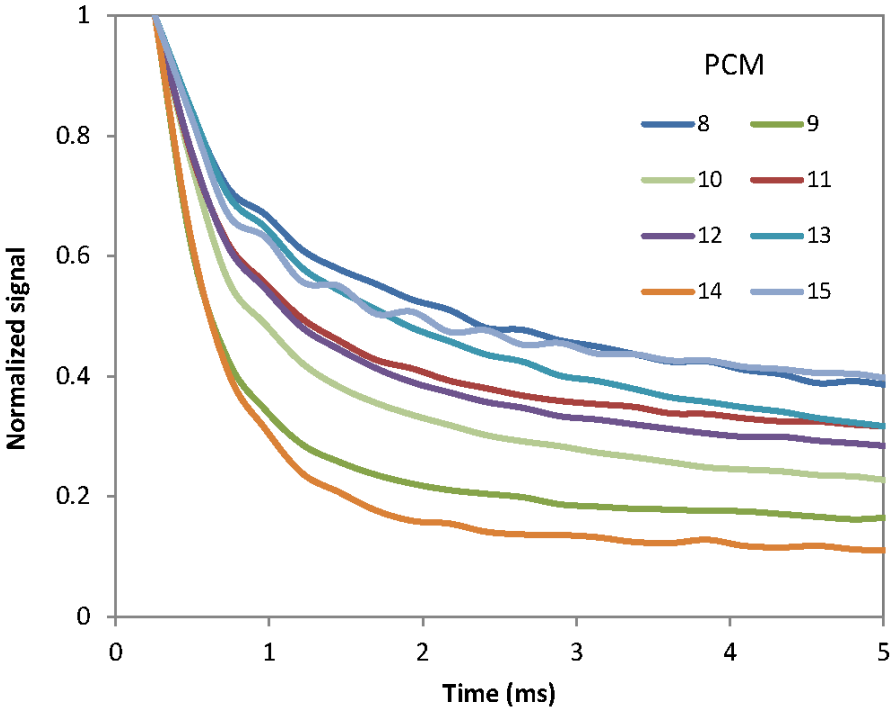

Figure 4-13: Raw NMR signals for saturated PCM samples

After saturation, the previous population showed a shift towards longer T_2, centred between 0.5 and 0.6 ms, with the exception of samples 24 and 26 which showed a shift up to 3 ms (Figures 4-16 & 4-17). This first population is defined as the short relaxation time (T_{2s}). A second population defined by long relaxation time (T_{2L}) was also recorded for some of the samples: PCM samples recorded a T_{2L} at 24.5 ± 6.5 ms while CCM had a T_{2L} around 18.2 ± 9 ms (Figures. 4-16 and 4-17). Individual samples T_2 distributions are shown in Appendix 3.

Saturated samples recorded total NMR porosity of 12.3 ± 3%. The average total NMR porosity contribution of the T_{2s} is 87% and 93% for PCM and CCM, respectively. TheT_{2L} contributed 13% and 7% for PCM and CCM, respectively. This secondary population T_{2L} is assigned to be the effect of the macro-pores filled by brine during the saturation process, with porosity reaching values > 10 % when it was only 4 ± 1.5 % under partial-saturation conditions.

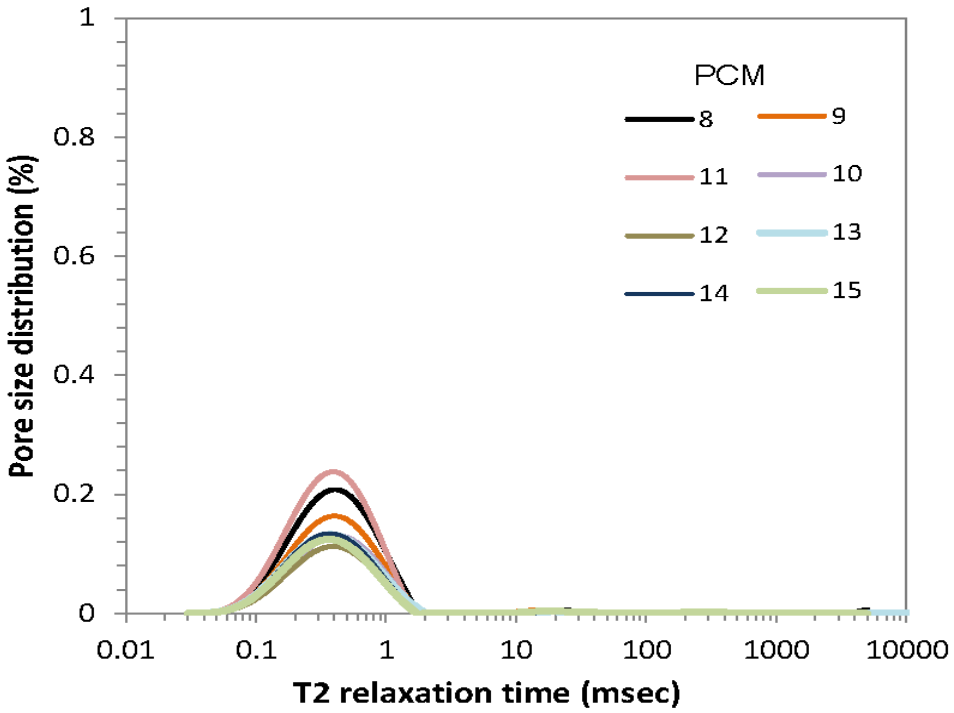

Figure 4-14: NMR T_2 relaxation time distribution of partially saturated PCM samples. The average relaxation time is centered around 0.35 msec

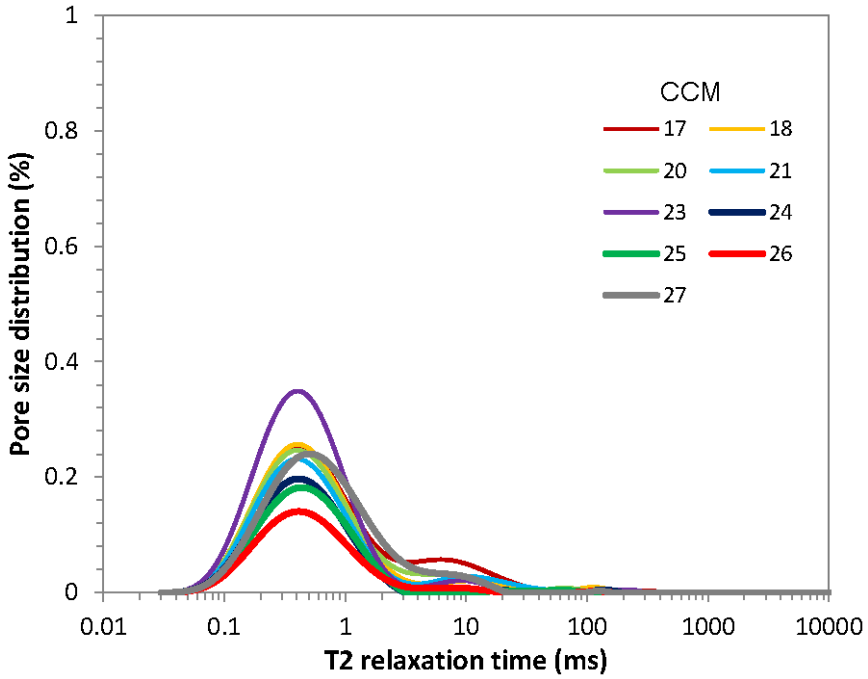

Figure 4-15: NMR T_2 relaxation time distribution of partially saturated CCM samples. The average relaxation time is centered around 0.35 msec.

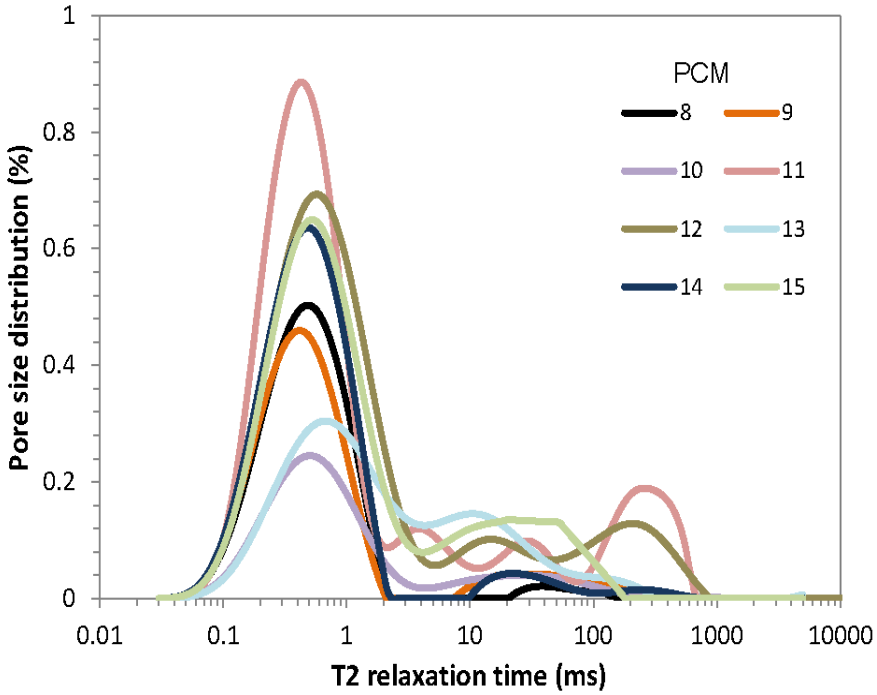

Figure 4-16: NMR T_2 relaxation time distribution of fully saturated PCM samples. Two average relaxation time populations centered around 0.5 msec (T_{2s}) and 24.5msec (T_{2L}).

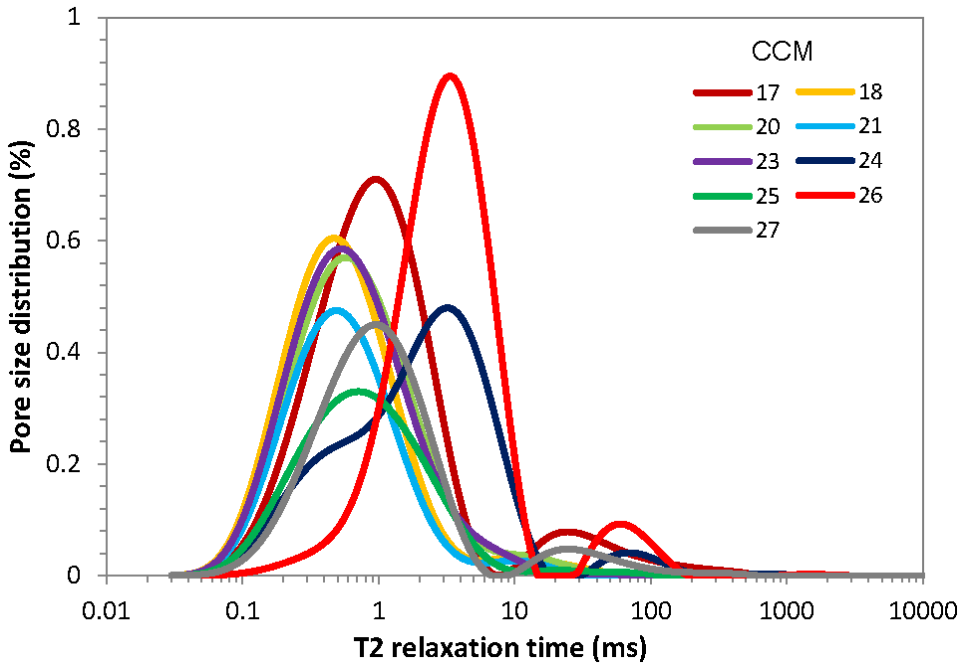

Figure 4-17: NMR T_2 relaxation time distribution of fully saturated CCM samples. Two average relaxation time populations centered around 0.5 msec (T_{2s}) and 18.2 msec (T_{2L}).

Table 4-3: NMR CPMG T_2 relaxation times results from the PCM and CCM samples collection. Two T_2 populations are recorded: a short T_{2s} and a long T_{2l}

	Partially Saturated		Brine Saturated				
Samples	**T_2s (ms)**	**Total porosity (%)**	**T_2s (ms)**	**Porosity Contribution @ T_2s (%)**	**T_{2l} (ms)**	**Porosity Contribution @ T_{2l} (%)**	**Total porosity (%)**
8	0.29	3.2	0.46	97	30.1	3	11.4
9	0.38	5.2	0.43	89	27.3	11	10.8
10	0.4	2.2	0.43	82	22.6	18	6.7
12	0.32	1.9	0.5	80	12	20	14.2
13	0.36	2.3	0.56	68	29.2	32	11.55
14	0.32	2.7	0.51	93	20.6	7	14
15	0.32	2.5	0.56	79	30.2	21	18.5
17	0.35	5.8	0.89	92	26.1	8	15.75
18	0.35	5.2	0.4	96	12	4	10.80
20	0.35	5.2	0.5	100	-	-	12.76
21	0.36	4.8	0.45	96	8.4	4	14.20
23	0.36	6.5	0.45	100	-	-	11.30
24	0.36	3.6	2.73	96	64.3	4	14.00
25	0.4	3.5	0.63	100	-	-	18.50
26	0.36	2.8	3.06	85	64.3	15	9.63
27	0.36	5.3	0.89	93	26.1	7	11.40

Table 4-4: Supplemental data extracted from NMR and MICP

Sample ID	**Rho (um/msec)**	**FFI Porosity (%)**	**T_2 Cutoff (msec)**	**Swirr (NMR Plot)**
8	0.005	8.18	0.63	28.12
9	0.012	5.55	0.45	48.37
10	0.014	4.48	0.50	32.93
12	0.013	12.30	0.55	13.38
13	0.018	9.25	0.56	19.91
14	0.003	11.30	1.24	19.29
15	-	16.00	0.63	13.51
17	0.002	9.95	1.11	36.83
18	0.007	5.60	0.29	48.15
20	0.060	7.56	0.38	77.61
21	0.015	9.40	0.20	33.80
23	0.019	4.80	0.43	57.52
24	0.041	10.40	0.25	25.71
25	-	15.00	0.25	18.92
26	0.007	6.83	1.11	29.08
27	0.011	6.10	0.35	46.49

4.3 Pore Size Distribution from Nitrogen Adsorption Experiments

Micromeritics TriStar II 3020 was used to determine the quantity of nitrogen adsorbed. The samples were prepared by sieving crushed samples less than 250 um. The samples were initially treated by heat and vacuum to remove contaminants. After cooling the sample under vacuum, nitrogen was dosed into the sample at controlled increments. The total pore volume from the adsorption tests was found from the quantity of vapour adsorbed at relative pressure. An assumption here is that the pores were filled with liquid adsorbate. Average pore size was then approximated by the total pore volume determined at maximum pressure, assuming that the unfilled pores below a very low relative pressure make a negligible contribution to the total pore volume.

Low pressure nitrogen isotherms for the samples in study are shown in Figure 4-18 to 4-20. The shapes of these curves suggest type II isotherms for the analyzed samples. Type II isotherms could be interpreted as the micropore filling at low relative pressures, and due to the presence of macropores in the samples, the adsorption isotherm rises rapidly near $P/P_o=1$. It is worth mentioning that the amount of adsorbed gas at low relative pressures is correlated with micropore volume, and at high relative pressures correlates to macro-pores, and all of the samples show the hysteresis type B (Appendix 4). Based on the classification by De Boer (1958), the pores can be interpreted as the slit-type pores.

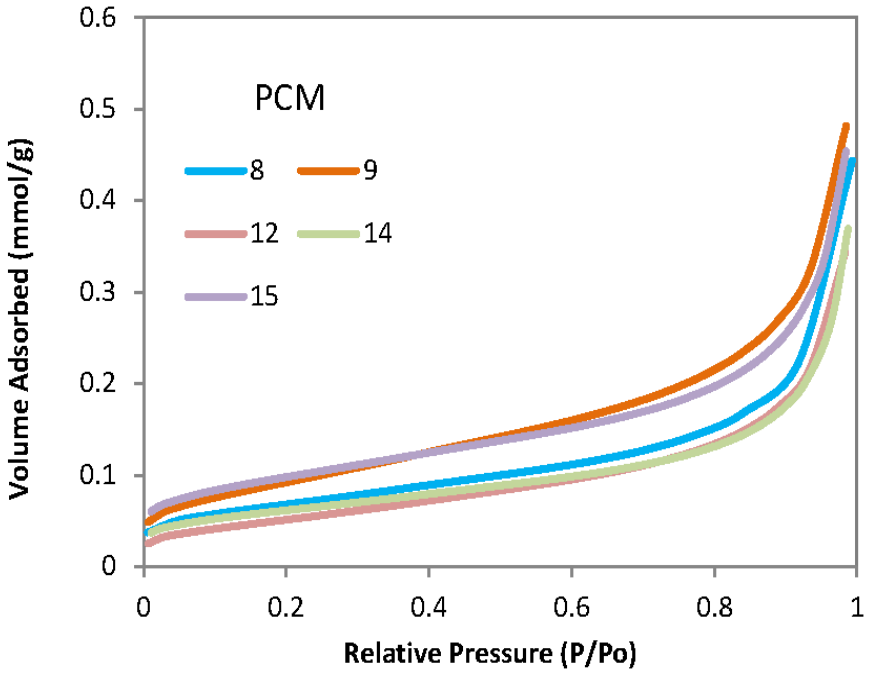

Figure 4-18: Low pressure nitrogen adsorption isotherms for PCM samples. The shapes of the curves suggest a type two isotherms.

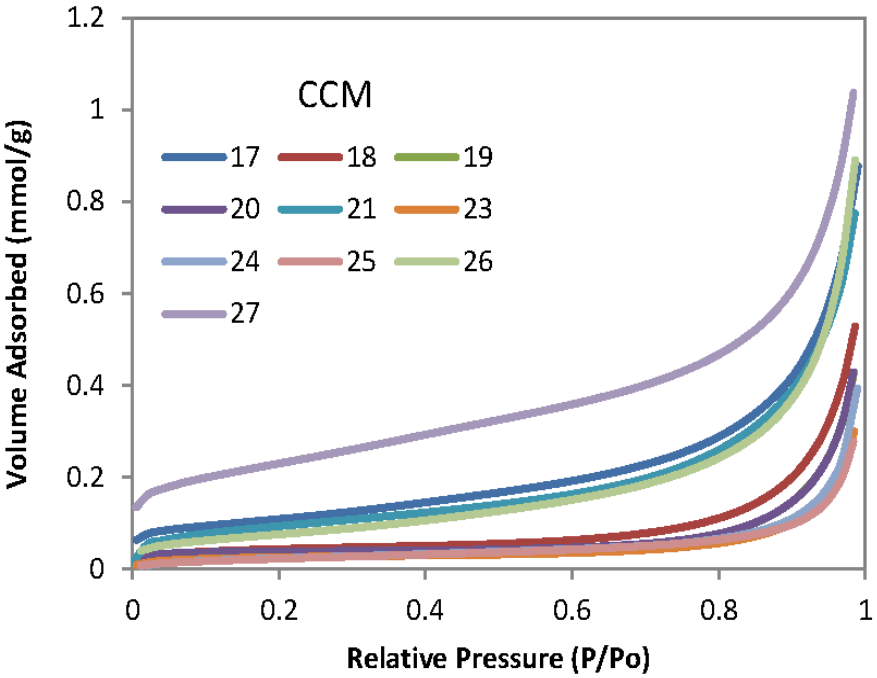

Figure 4-19: Low pressure nitrogen adsorption isotherms for CCM samples. The shapes of the curves suggest a type two isotherms.

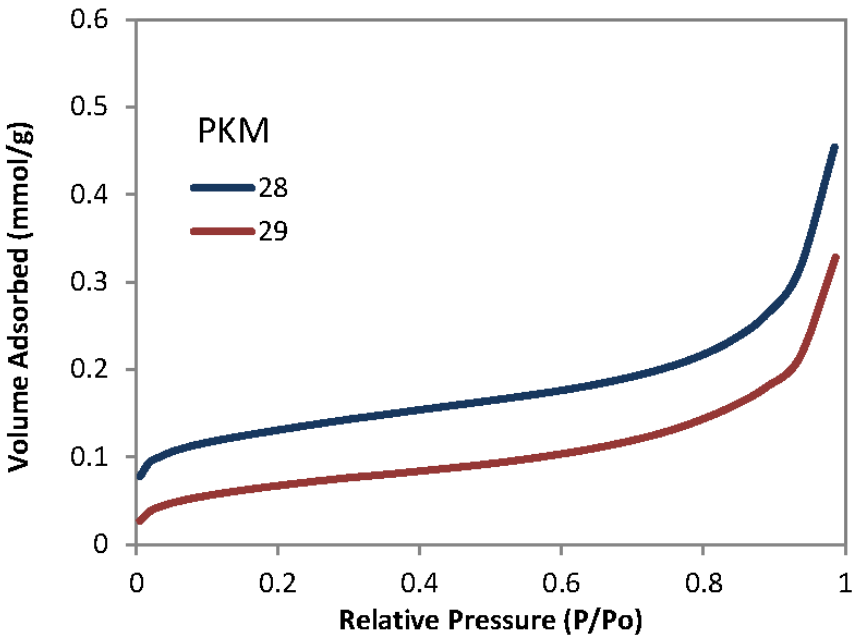

Figure 4-20: Low pressure nitrogen adsorption isotherms for PKM samples. The shapes of the curves suggest a type two isotherms.

A summary of the results collected from low pressure adsorption measurements and the IUPAC pore percentages are shown in Table 4-5. The average pore radius for the whole data set was found to be around 7.5 ± 2.9 nm, with CCM showing larger pore sizes (9.2 ± 2.4 nm) compared to PCM (5.2 ± 1.5 nm). Pore volumes and surface areas obtained from N_2 tests show a relatively narrow range for both formations PCM and CCM, with the exception of samples 17 and 27 from formation CCM. The average BET surface area is similar for the two tested formations (CCM and PCM) at around 5. 5 ± 2 mm^2/g. But the total pore volume for CCM is higher than PCM at 2 ± 0.9 $cm^3/100g$ and 1.39 ± 0.2 $cm^3/100g$ respectively. All of these samples are characterized by a very high contribution of the meso-pore size, at 78.5 ± 7.3% of the total porosity (Figures. 4-21 to 4-23). Individual samples N_2 adsorption and desorption graphs are shown in Appendix 4.

Table 4-5: Nitrogen adsorption results and pore volume percentages based on IUPAC classification from the gas shale collection

					% DFT Model (Porosity)		
Formation	**SAMPLE ID**	**BET Surface Area (m^2/g)**	**Total Pore Vol. ($cm^3/100g$) at maximum pressure**	**Average Pore Radius (nm)**	**Micro-pore Vol.**	**Meso-pore Vol.**	**Macro-pore Vol.**
PCM	8	5.4	1.54	5.7	5.4	85.7	8.9
	9	7.6	1.67	4.4	4.4	93.0	2.7
	11	2.3	0.99	8.5	1.1	84.0	15.0
	12	4.3	1.19	5.6	1.0	93.0	6.3
	13	4.9	1.28	5.2	5.6	72.0	22.5
	14	7.8	1.57	4.0	11.2	78.6	10.3
	15	6.0	1.28	4.3	10.1	75.8	14.0
	16	7.8	1.55	4.0	11.3	75.8	13.0
CCM	17	8.7	3.04	7.0	3.0	78.2	18.8
	18	3.4	1.83	10.8	1.9	63.7	34.4
	19	2.8	1.49	10.8	2.7	76.2	21.1
	20	2.8	1.42	10.5	2.6	77.2	20.2
	21	7.7	2.69	7.0	2.5	81.8	15.7
	22	3.4	1.39	8.2	3.0	77.9	19.1
	23	2.0	1.04	10.3	2.9	74.7	22.4
	24	2.1	1.36	13.1	0.0	66.4	33.6
	25	2.0	0.96	9.6	0.0	78.2	21.8
	26	6.3	3.09	9.9	0.0	80.0	20.0
	27	18.0	3.6	4.0	11.7	79.3	9.1
PKM	28.0	10.0	1.6	6.3	14.8	82.9	2.4
	29.0	5.4	1.1	8.4	9.3	87.0	3.7

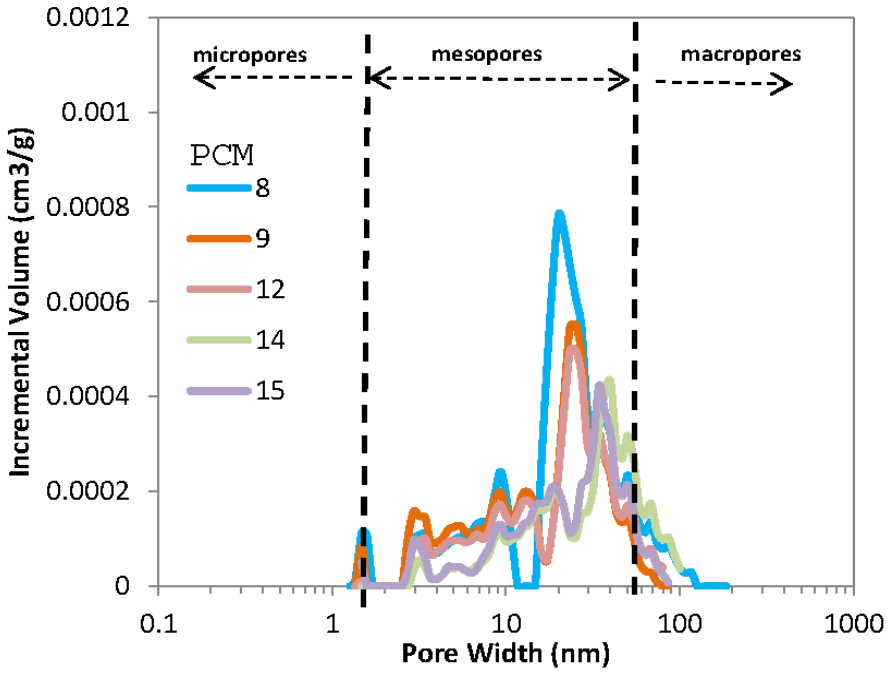

Figure 4-21: Pore size distribution from nitrogen adsorption tests with IUPAC boundaries of micro-, meso- and macro-pores for PCM samples. The average pore size is 5.2 nm.

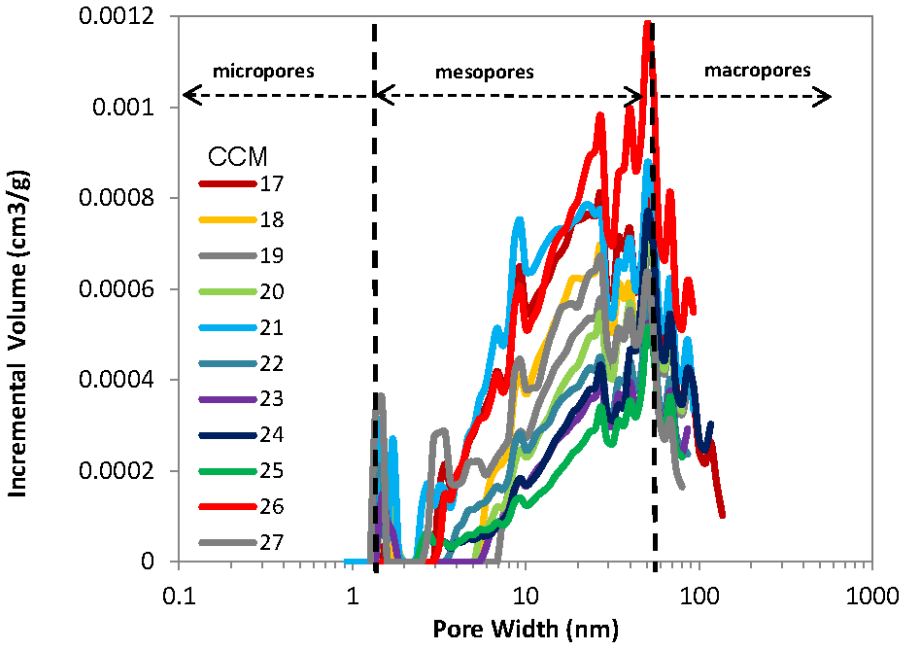

Figure 4-22: Pore size distribution from nitrogen adsorption tests with IUPAC boundaries of micro-, meso- and macro-pores for CCM samples. The average pore size of 9.2 nm.

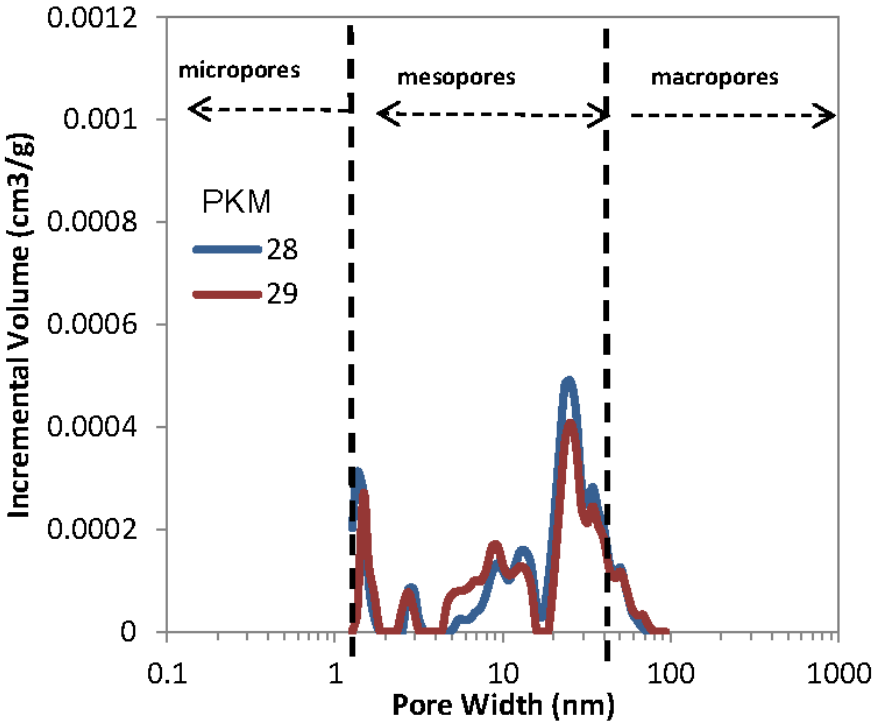

Figure 4-23: Pore size distribution from nitrogen adsorption tests with IUPAC boundaries of micro-, meso- and macro-pores for PKM samples. The average pore size is 7nm.

Considering the extracted micro-, meso- and macropore volumes using the DFT model and other parameters extracted using low pressure adsorption analysis, the following results can be summarized:

- There is an inverse relationship between pore size and BET surface area (Figure 4-24)
- The BET surface area shows an increasing trend with increasing micropore volume, while there is not any conclusive relationship between macropore volume and BET surface area (Figure 4-25)
- All samples show an increase in micropore volume and decrease in macropore volume with decreasing average pore diameter (Figures 4-26 & 4-27).

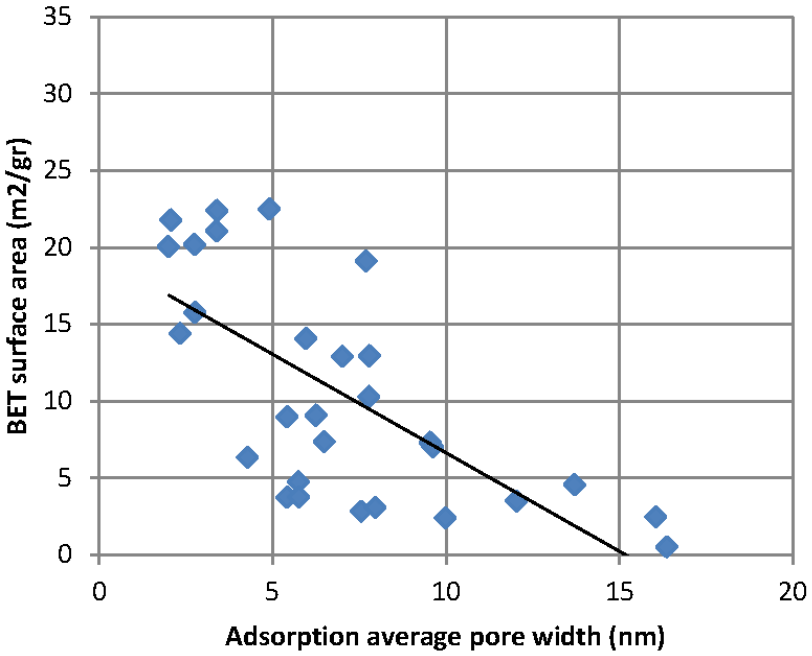

Figure 4-24: The figure shows an inverse relationship between pore size and BET surface area

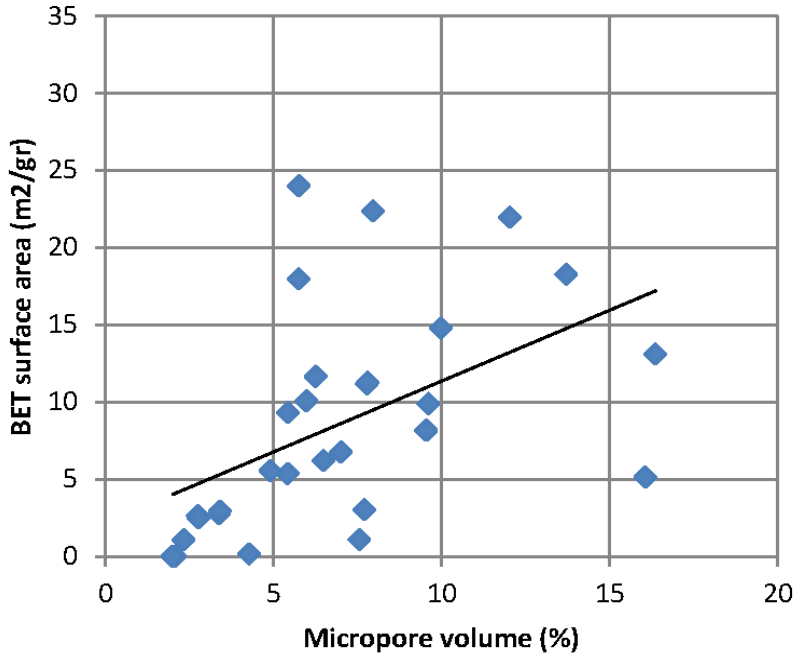

Figure 4-25: Relationship between BET surface area and micropore volume

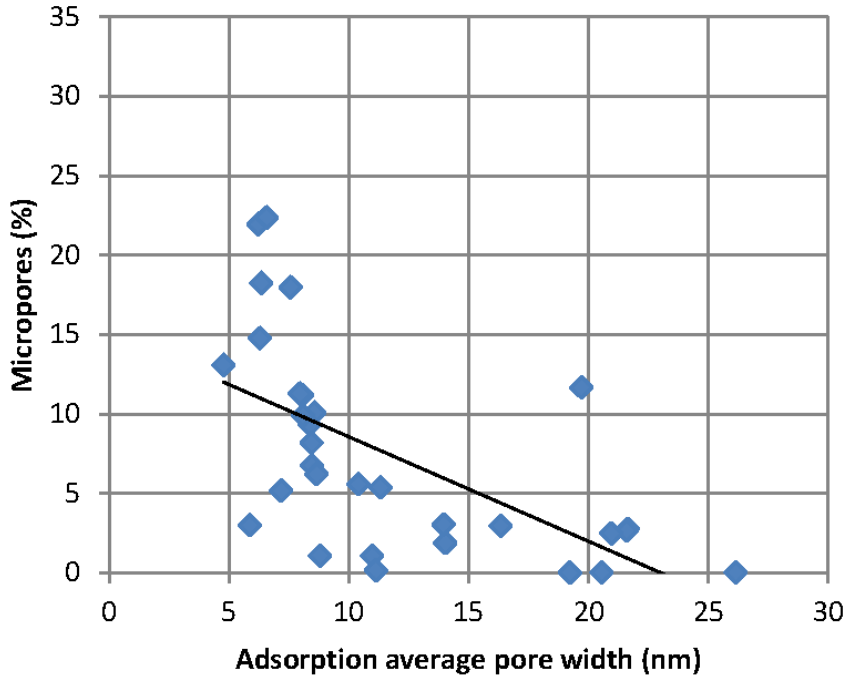

Figure 4-26: Relationship between pore size and micropore volume

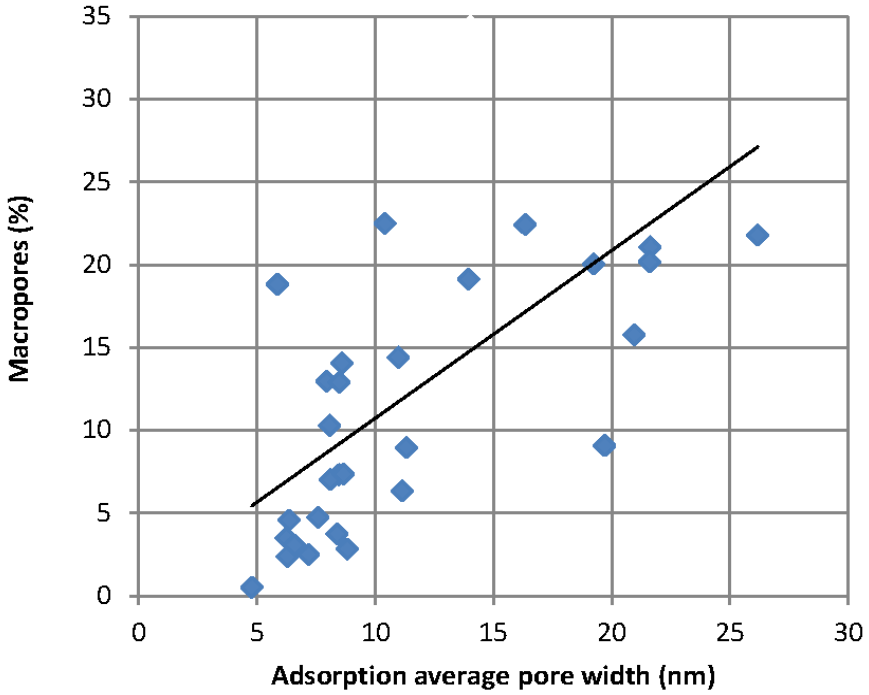

Figure 4-27: Relationship between pore size and macropore volume

4.4 Scanning Electron Microscopy

SEM imaging was conducted on PCM samples using a Zeiss Neon 40EsB. The Zeiss Neon 40EsB is equipped with a field emission gun with a maximum EHT voltage of 30 kV. Individual samples were mounted upon pin type mounts prior to coating with a thin layer of platinum, to ensure surface conductivity. Samples were introduced into the SEM for secondary electron imaging using an EHT of 5 kV. Mineralogy and pore size were visually identified with the resultant images.

SEM imaging and energy dispersive x-ray spectroscopy (EDS) was conducted on CCM samples using a Philips XL40 equipped with a Bruker Quantax EDS detector. The Philips XL40 is a controlled pressure SEM equipped with a tungsten filament with a maximum EHT voltage of 30 kV. Individual samples consisted of polished shale chunks that were impregnated with epoxy prior to carbon coating, to ensure surface conductivity. Samples were introduced into the SEM for back scattered imaging using an EHT of 30 kV. Additionally, the SEM was typically operated at a chamber pressure between 0.1 to 0.5 mBar to assist in charge reduction. Mineralogy and pore size were visually identified with the resultant images. Mineralogy was reaffirmed with the resultant EDS spectra.

The visual interpretation of mineralogy and porosity in PCM and CCM was conducted using two distinctive SEM imaging modes. The SEM imaging, consisting of both SE and BSE images, reveals quartz and clay particles as the dominant components of the shale (Figure 4-28). These results are in agreement with the XRD results. The images suggest that quartz is typically found as large discrete particles intermixed with clay. The clay particles are displayed as repeating layers of flat platelets, typical of Illite and/or Kaolinite. Secondary minerals, such as iron rich materials, are visible within the images and are typically highlighted during BSE imaging. Additionally, the images suggest that macro-pores were found at the boundaries of individual particles. Furthermore, meso-pores between the layers of the clay platelets were witnessed. Additional SEM images are shown in Appendix 5.

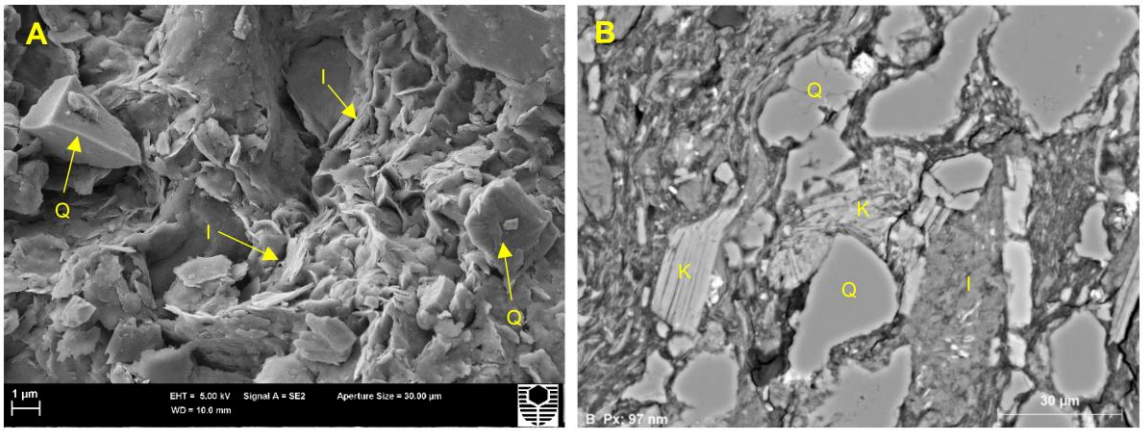

Figure 4-28: (A) SE image of sample 14 displaying dominant illite & quartz particles (B) BSE image of sample 20 displaying dominant kaolinite, illite and quartz particles.

4.5 Focused Ion Beam/ Scanning Electron Microscopy

A chunk of ± 20 x 5 mm size from the sample 10 was embedded in resin and the surface was polished up to 1200 grit. The sample was placed on an aluminium stub using a silver dab and coated with silver and carbon to reduce electron charging and energy drift. The sample was placed on the dual beam stage at an angle of 52 degrees and a working distance of 4mm, and the chamber was vacuumed (Figure 4-29). Platinum (20 x 20 x 2.5 µm) was deposited on the region of interest using 30 KV and 0.28 nA energy beam (Figure 4-30).

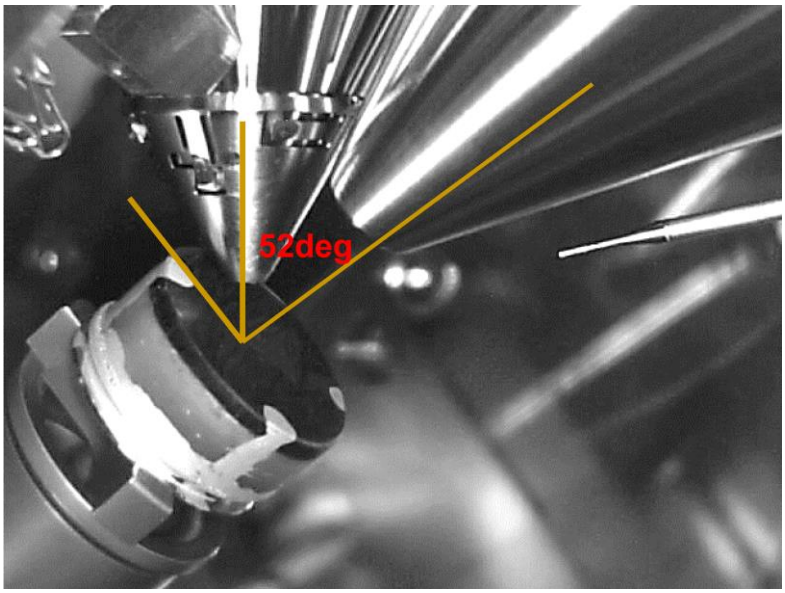

Figure 4-29: Illustration of the sample stage tilted at an angle 52 degrees in the FIB/SEM instrument

A large trench was removed around the platinum coat at various beam currents and voltages (Figure 4-30). The large trench reduces the debris around the surface to be imaged. The final cut was performed at 30 KV and 0.93 pA energy beam to provide a fine clean cut. The milling process for a 10 x 10 x 7 µm specimen size was carried out at an energy beam of 2 KV and 1.4 nA using back-scattered electrons. The FIB/SEM image acquisitions and pore size analysis focus on a small volume area of the sample that is not necessarily representative of the core-plug results from laboratory methods.

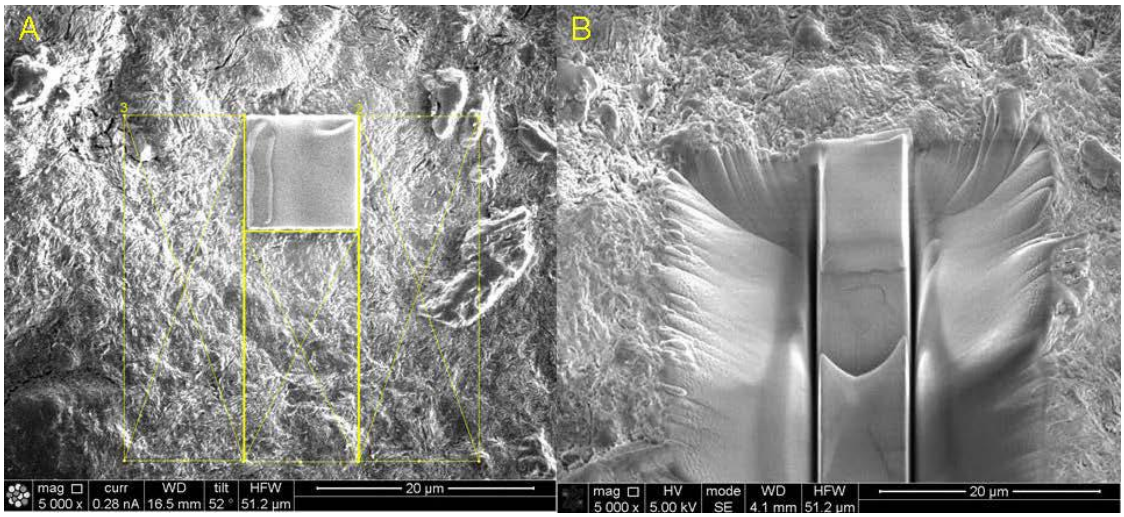

Figure 4-30: (A) Image from FIB/SEM showing the platinum coating (rectangular section) (B) Image showing the rough cut of the trench around the platinum deposit.

FIB/SEM image acquisition and analysis was conducted on sample 10 from PCM formation to visually inspect the pore characteristics and to support experimental analysis. Figure 4-31 provides a brief illustration of the image analysis conducted for sample 10 following the general image analysis procedures (as shown in Figure 6). The total porosity from sample 10 was found to be 3.56% and the majority of the pore sizes was in the range of 0.05 um (Figure 4-32), comparable to what was obtained from MICP porosity (3.17%). From the image example, it is obvious that the pores are not an ideal shaped circle. Hence, the average shape factor was found to be 0.35, where a circle equals to 1. In addition, the average eccentricity was found to be 0.86, which describes how elongated the pores are. An object can have an eccentricity value between 0 –1, where 0 is a perfectly round object while 1 is a line shaped pore.

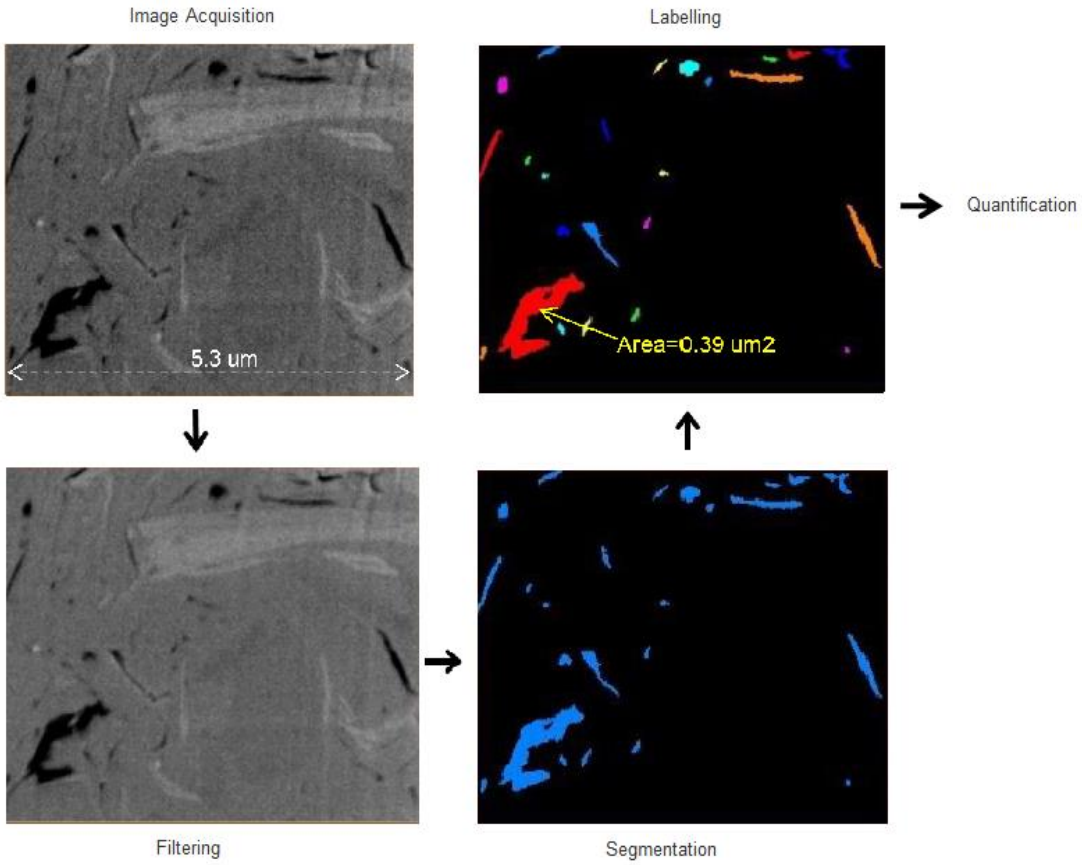

Figure 4-31: Illustration of the image analysis conducted for sample 10 following the general image analysis procedures. From top left, the raw FIB/SEM image acquired contains background noise. It is fitered to enhance the image quality. The image is then segmented to simplify the representation to make it more meaningful (binary image). Then it is labelled to assign a particular pore size range to a colour. The labelled image can further be used for quantification of various parameters.

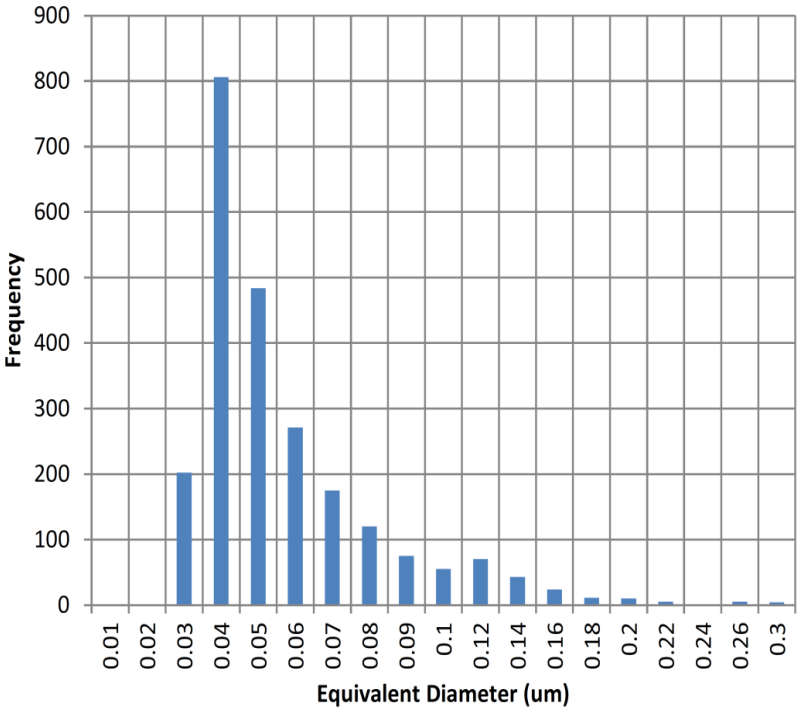

Figure 4-32: Pore size distribution of sample 10 from image analysis. Majority of the pore size diameter are centred around 0.045 microns.

4.6 Capillary Pressure and Permeability

Generally, permeability is measured in laboratories using core plugs. In some cases, however, it is difficult to obtain suitable core plugs. In these instances, other approaches can be used to predict permeability, which are chiefly based on mathematical and theoretical models. Predicted mercury injection capillary pressure (MICP) permeabilities are compared with those measured permeabilities. Models evaluated in this study include the Kozeny-Carman (Wylllie and Gregory,1955) and Swanson (1981), Winland (Kolodzie, 1980), Jorgensen (1988), Pape et al (1999), Rezaee et al (2006), Katz-Thompson (1986), Pittman (1992) and Dastidar et al (2007) methods.

The generated data set consists of 10 samples from the PCM formation. The dimensions of the core samples are either 2.5 or 3.8 cm in diameter at various cylindrical lengths. End trims of six samples with various sizes were used for MICP

measurements, and a total of 10 samples were used for permeability measurements (Figure 4-33).

Generally, for gas shale formations, the accuracy of the mercury injection capillary pressure-based permeability methods is expected to be low. As a quantitative comparison, the authors rank the mean square error (MSE) and the standard deviation (σ) in ascending order, and coefficient of determination (R^2) in descending order. The final ranking of the suitable model is done through a cumulative rank of each MSE, σ and R^2. Table 4-6 summarises the ranking of each MICP permeability method.

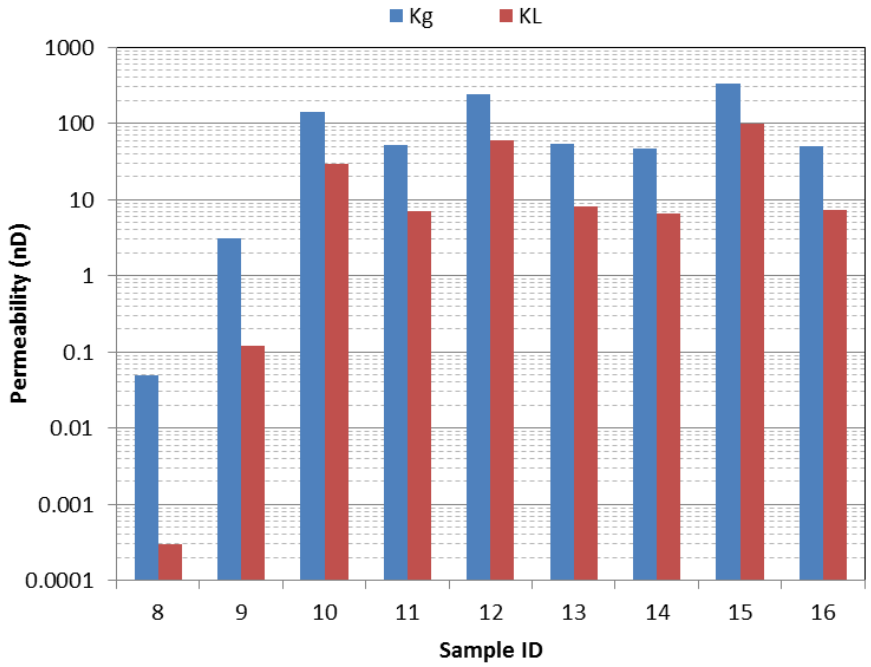

Figure 4-33: Bar chart of the measured gas permeability (blue) and the corrected liquid permeability (red) on selected PCM samples

Table 4-6: Ranking of predicted MICP permeability

Rank	Method	Equation Reference	MSE	Std Devi.	R^2	SUM
1	Rezaee R_{50}	(Rezaee et al. 2006)	2	1	4	7
2	Pittman R_{25}	(Pittman 1992)	3	4	1	8
3	Winland R_{35}	(Kolodzie 1980)	5	3	2	10
4	Datidar (OU Method)	(Dastidar et al. 2007)	6	2	3	11
5	Pape	(Pape et al. 1999)	7	6	5	18
6	Kozney-Carman	(Wyllie and Gregory 1955)	1	5	8	14
7	Swanson	(Swanson 1981)	4	8	7	19
8	Jorgensen	(Jorgensen 1988)	8	7	6	21

5. CHAPTER 5: DISCUSSION

5.1 Porosity and Pore Size Distribution

The bulk porosity from MICP, N_2 and NMR presents some differences (Table 4-1 & 4-3). Indeed, the porosities from MICP and N_2 are mostly constant around 3-3.5%, with more variability recorded from the N_2 method. The porosities from NMR are much higher, between 6 and 15%, which corresponds to three times higher than for the MICP or N_2 methods. This scale of difference with NMR has been described by other research that has analyzed mudstones (Hildenbrand & Urai, 2003). Possible explanations of these higher values of porosity from NMR come from the fact that

i. NMR measures both connected and dead pores (un-connected) that can belong to any pore sizes in the micro- to macro-pore range. Further, MICP porosity measures the porosity involved in the fluid transport (effective porosity) and misses out on the pores located within the grains and the clay bound water porosity.
ii. Samples were dried out for MICP experiments, inducing potential clay skrinkage, while the NMR re-saturation with artificial brine was prone to generate clay swelling and cracks.

The MICP PSD did not seem to be able to record three types of pores as the N_2 did, with micro-, meso- and macropore distribution (Tables 4-2 & 4-5). MICP advocates substantial pore volume percentages in the meso- and macro-pore range. Samples 7, 30 and 31 obtained from MICP analysis, have the largest meso-pore volume and the least macro-pore volume. The slight inconsistency between MICP and N_2 is because MICP only quantifies pore throat sizes and not the pore bodies, whereas N_2 quantifies both of them.

PSD analysis using NMR and MICP methods gives similar results, with pore distribution made of meso- and macro-pores. While N_2 was able to record the micro-porosity (pore size < 2 nm), the pressure injection of mercury was not strong enough to over-ride the strong capillary pressure of such small pore throat sizes. Considering that partial saturation of the core plugs kept the fluids inside the micro- and meso-pores intact due to strong capillary pressure and clay bound water, the NMR was also not able to record the micro-porosity. The general contributions of MICP and NMR

to analysis of meso- and macro-pores are similar. MICP showed 68% meso-pores and 32% macro-pores, and NMR showed 63% meso-pores and 37% macro-pores. A drawback of the NMR T_2 measurements is that some of the nano-pore signals (i.e. micro-porosity) that are typical in shales cannot be detected by the low field NMR, with $T_2 < 0.03$ ms (or 30 µs).

Macro-porosity, defined by long T_2 and pore > 0.6 µm using MICP, usually controls the bulk porosity results, where a high contribution of macro-pore volumes, such as in sample 4, records high porosity; and inversely if the macro-pore contribution is low. From this, MICP and NMR PSD being similar, T_2 distribution could be converted into pore body size distribution sensu-stricto, using MICP as calibration.

5.1.1 NMR and MICP porosity relationship

Furthermore, we have looked for a relationship between NMR and MICP porosities. The approach is as follows:

1. Determine the open pore volume (V_o), that is, the difference between the brine saturated mass and the partially saturated mass of the core plugs.
2. Determine the total volume (V_T) of the plug.
3. Calculate open pore porosity:

$$\emptyset_{NMRO} = \frac{PV_o}{V_T} \qquad \text{Equation 5-1}$$

The first approach is as follows: to find the isolated pores, determine the T_2 cut-off, as outlined above, to find meso-pore porosity minus the open pore porosity.

The determined values are shown in Table 5-1. This shows a reasonable correlation between NMR open porosity and MICP porosity, with a coefficient of correlation > 60%, excluding samples 21 and 26, where the MICP porosities are high compared to other samples (Figure 5-1). This provides further support that both MICP and NMR can be integrated to understand the pore geometry of gas shale and inter-use their parameters.

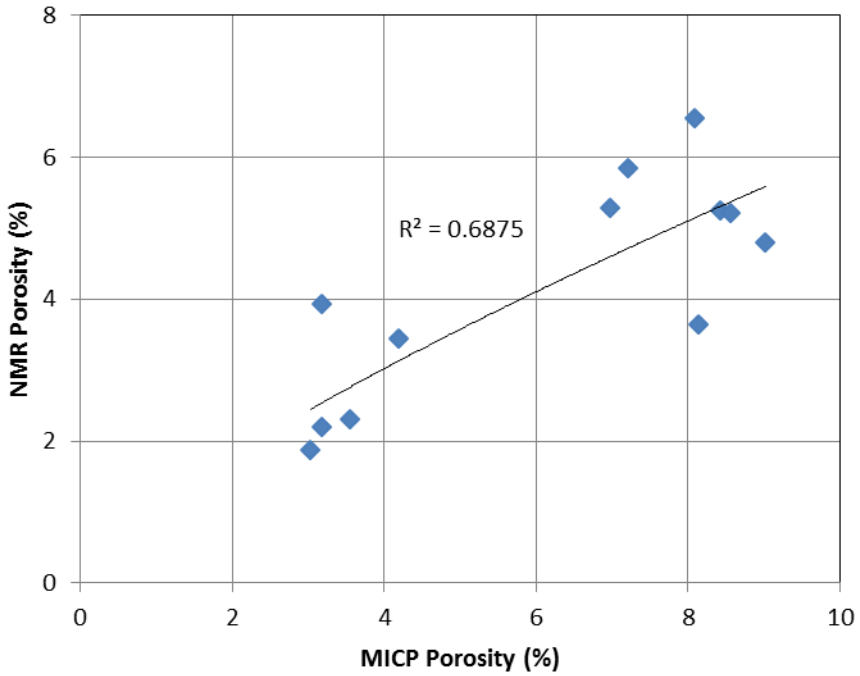

Figure 5-1: NMR open pore porosity versus MICP porosity

Table 5-1: Supplementary determined data from NMR

Sample ID	Total Volume (cc)	Saturated Mass (g)	Partially saturated mass (g)	Open Pore Volume (cc)	Open Ø %	MICP Ø (%)
8	44.24	117.37	115.84	1.53	3.45	3.78
9	58.00	154.10	152.75	1.35	2.32	3.05
10	64.44	170.83	167.25	3.58	5.55	3.17
11	63.63	170.43	167.33	3.10	4.87	3.03
12	56.85	153.81	148.17	5.64	9.91	3.54
13	55.43	145.85	144.42	1.43	2.57	3.56
14	60.98	163.62	158.46	5.17	8.47	-
17	55.26	139.78	135.60	4.18	7.56	7.22
18	33.69	75.01	72.82	2.19	6.49	8.43
19	36.85	81.93	78.77	3.16	8.58	8.55
21	42.28	89.02	87.36	1.67	3.95	9.02
23	21.54	45.36	44.20	1.16	5.39	8.08
24	25.02	60.58	58.34	2.24	8.96	8.14
25	26.02	64.60	63.35	1.25	4.82	4.18
26	73.36	185.38	175.50	9.88	13.40	7.01
27	77.55	217.23	212.49	4.74	6.11	6.98

5.1.2 Pore body-to-pore throat size ratio: pore geometry complexity

The complex pore geometry, previously observed from FIB/SEM images, can be evaluated from NMR measurements. Pore body to pore throat ratio is one of the most important characteristics that control fluid flow. The connectivity in the pore system can be represented by the pore body to pore throat size ratio: the lower the ratio, the lower the connectivity; and so the lower the permeability/fluid flow will be. In a complex pore system such as gas shale, the pores exhibit an irregular shape (Figure 4-31). Determining the exact physical shape of the pores is difficult, time consuming and requires demanding test equipment.

Table 5-2: Computed pore body to pore throat size ratio (C) on the Cmf samples from NMR dataset calibrated against gas permeability measurements

Sample ID	Kg (nD)	NMR porosity (%)	C (constant)
8	0.05	11.38	0.001
9	3.10	10.75	0.29
10	29.90	6.68	4.47
12	61.00	17.65	3.46
14	8.20	11.55	0.71
15	46.60	10.57	4.41

The pore body to pore throat size ratio was derived from the Coates equation (Coates et al., 1998). Indeed, the permeability can be computed from NMR T_2 distribution following the Coates equation:

$$k_{Coates} = \left[\left(\frac{ø}{C} \right)^2 \left(\frac{FFI}{BVI} \right) \right]^2$$

Equation 5-2

with ø for total porosity (%), FFI for the Free Fluid index (or movable water), BVI for the Bound Volume of Irreducible water. C is a constant parameter usually used to "tune" the NMR log analysis from the Coates equation. But behind this constant lies the concept of pore geometry defined as: pore throat to pore body size ratio. A "strong" geometry will be characterized by low C, representing a very small pore throat compared to the pore body size that will require a lot of pressure to overcome the strong induced capillary pressure and will increase the fluid trapping effect during/after flow experiments. The results will be a very low permeability when C is

low, and vice versa. Typically, sandstones have C = 10, which can decrease when clay minerals occur. Clay rich rocks should have a very low C, a strong complex pore geometry.

Equation 5-2 implies the T_2 cut-off that separates the capillary and clay-bound water (BVI), residing in small pores and intra- and inter-clay layers, from the movable water (FFI) residing in large pores. Based on the literature, the classical T_2 cut-off is set at 33 ms for sandstone reservoirs (Coates et al., 1999). For these gas shale samples, we based our assumption that T_2 relaxation response from the partially saturated samples is due to irreducible fluids (CBW and capillary bound water), where all the mobile water was evaporated. The difference in T_2 response between brine saturated and partially saturated is mostly due to mobile fluids. On a commutative NMR signal curve as a function of T_2 relaxation time, the NMR signal is therefore common along a short T_2 range, where the same irreducible water signal is recorded from both hydration states of the sample, until a point of divergence where only the mobile water acts from the saturated sample condition. This point of divergence corresponds to the T_2 cut-off.

The best C parameter from the Coates equation can then be derived to match the computed permeability from NMR against the measured gas permeability (Kg). All the C constants are relatively low, at << 10 (Table 5-2), demonstrating a complex geometry of the pore network, as expected from clay rich rocks. However, among the Cmf sample collection, the range of gas permeability is directly a function of the pore geometry C, with the highest permeability exhibiting the highest C constants. This illustrates weaker geometry and/or higher pore connectivity that ease the fluid to flow through the pore network in some samples from the same formation.

The modified equation was found to be:

$$K = \left[(0.277\emptyset)^{0.005}\left(\frac{FFI}{BVI}\right)\right]^{3.2} \qquad \text{Equation 5-3}$$

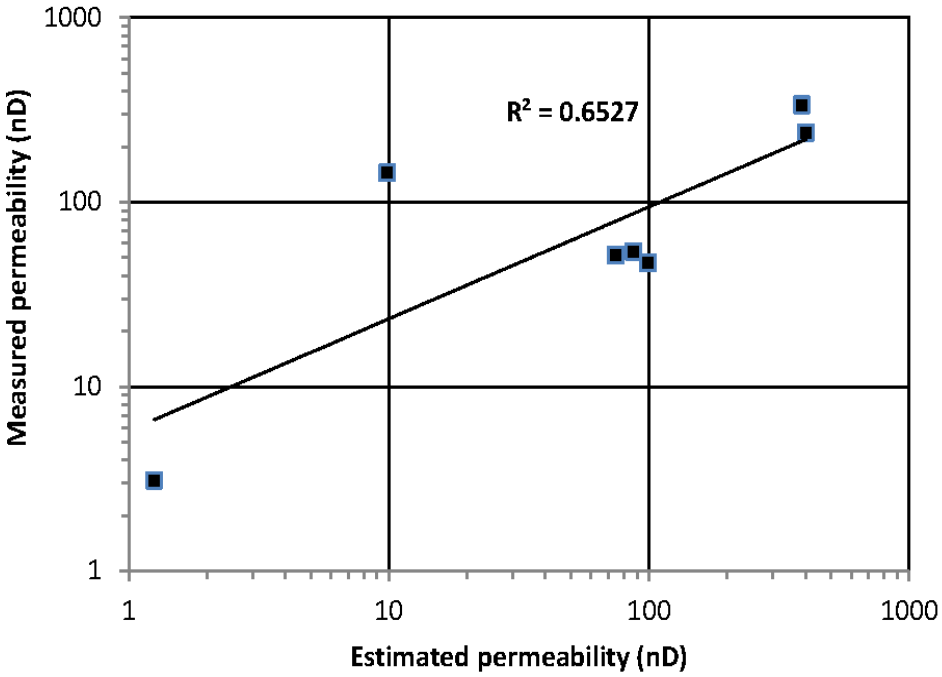

Figure 5-2: Cross plot of measured and predicted permeability from modified Coates equation with C= 3.6, a=0.002 and b=3.2

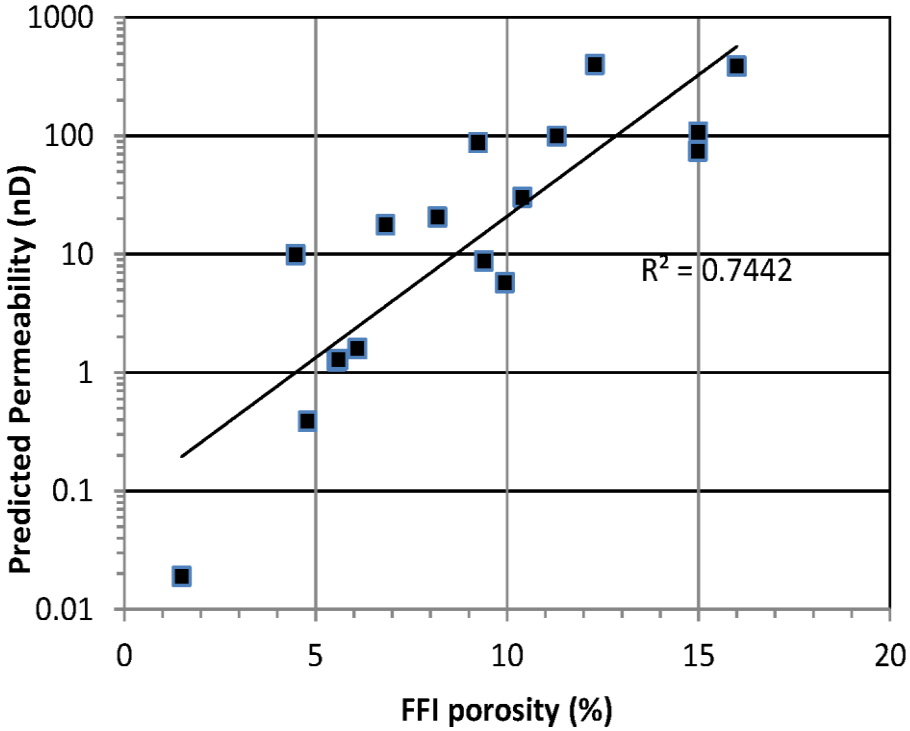

Figure 5-3: Estimated permeability versus FFI porosity from NMR using the modified equation

5.2 Interchanging MICP with NMR data

5.2.1 Correlating NMR and MICP

Fluid distribution analysis needs to take into account the interaction between rock and fluid. Such complex interactions can be understood through capillary pressure and pore geometry. The focus of this study is to integrate mercury injection capillary pressure (MICP) data with nuclear magnetic resonance (NMR) data. Through the estimation of the surface relaxivity parameter, the NMR transverse relaxation time (T_2)-equivalent capillary pressure and MICP-equivalent T_2 were successfully estimated on gas shale samples from Western Australia.

The procedures we used to determine the NMR T_2 equivalent pore diameter are similar to those suggested by Lowden (2009) with slight modifications. The approach is based on a single phase, where the wetting phase is similar to the saturating phase. No static magnetic gradient field was applied during the CPMG sequence, and $1/T_2$ bulk is so small that equation (2-31) can be reduced to the second part of the equation as a function of the pore geometry and surface relaxivity. Based on equation (2-12), samples with small pores will relax much faster compared to samples with larger pores. The T_2 distribution then defines the pore size distribution (PSD):

$$\frac{1}{T_2} = \rho_2 \left(\frac{S}{V} \right)$$ Equation 5-4

1. Determine the T_2 equivalent pore diameter (size) using the following formula:

$$D = T_2 . \rho_2 ,$$ Equation 5-5

where D is the MICP pore throat diameter (μm), ρ_2 is the surface relaxivity (commonly denoted as the scaling factor) (μm/msec), and T_2 is the transverse NMR relaxation time (msec). The scaling factor in this study was obtained from NMR and MICP laboratory measurements. It was found by taking the dominant pore diameter (MICP) and dominant T_2 relaxation time (NMR). The procedures are as follow:

2. Determine the weighted incremental pore volume from the T_2 distribution. This is found by multiplying the pore volume at each data point by the ratio of MICP/NMR bins (pressure points). This weighted incremental volume versus the T_2 equivalent pore diameter can be plotted along the same axis with pore diameter versus normalized incremental volume from the MICP data (Figure 5-4).
3. Determine the cumulative pore volume from the NMR data and find the NMR capillary pressure derived from:

$$P_{NMR} = \frac{4.\sigma.\cos\theta.b}{T_2 eqv.\,\text{pore diameter}} \qquad \text{Equation 5-6}$$

where b is a shifting factor to shift the T_2 equivalent capillary pressure up or down.

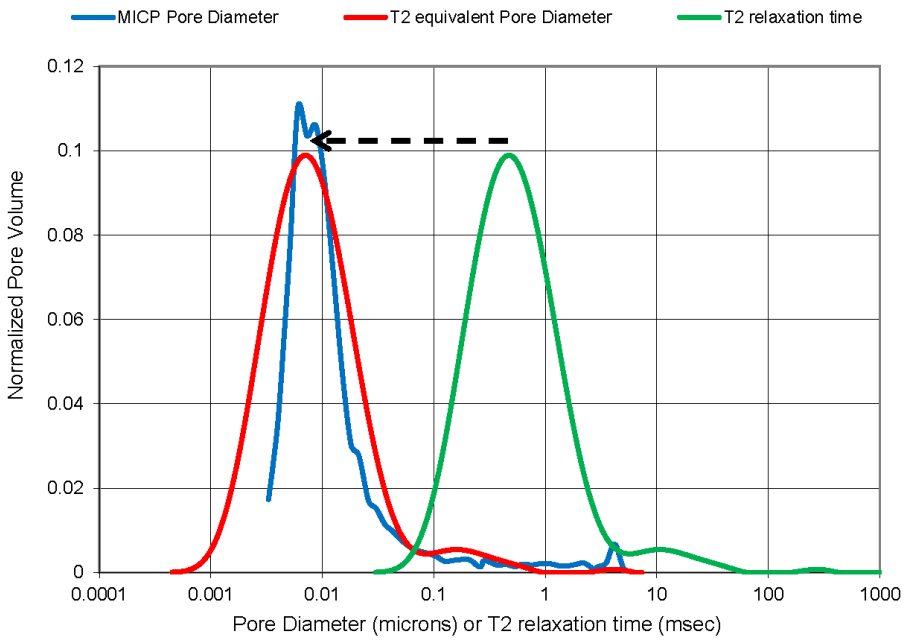

Figure 5-4: Graphical representation of correlating MICP and T_2 relaxation time to obtain T_2 equivalent pore size distribution

Figures 5-5 and 5-6 show the results of the T_2 equivalent pore diameter and T_2 equivalent capillary pressure, respectively. The average surface relaxivity for the samples was 0.02 µm/ms (Table 5-3). Such a low value was expected for these clay-

rich samples. Having a larger surface–volume ratio would produce a lower surface relaxivity. Looyestijin (2001) proposed using a single value of the scaling factor (ρ_2) for the whole data set as opposed to taking an individual scaling factor for each sample. In some instances it may be necessary to use a value for each sample because of the large variation in (ρ_2) and formation type, as in our case.

Lowden (2009) suggested that the clay-bound water portion from the NMR T_2 distribution be removed when deriving the capillary pressure, because when computing the cumulative pore volume (NMR), porosity at the maximum diameter should equal zero, and porosity at the minimum diameter should equal the total NMR porosity.

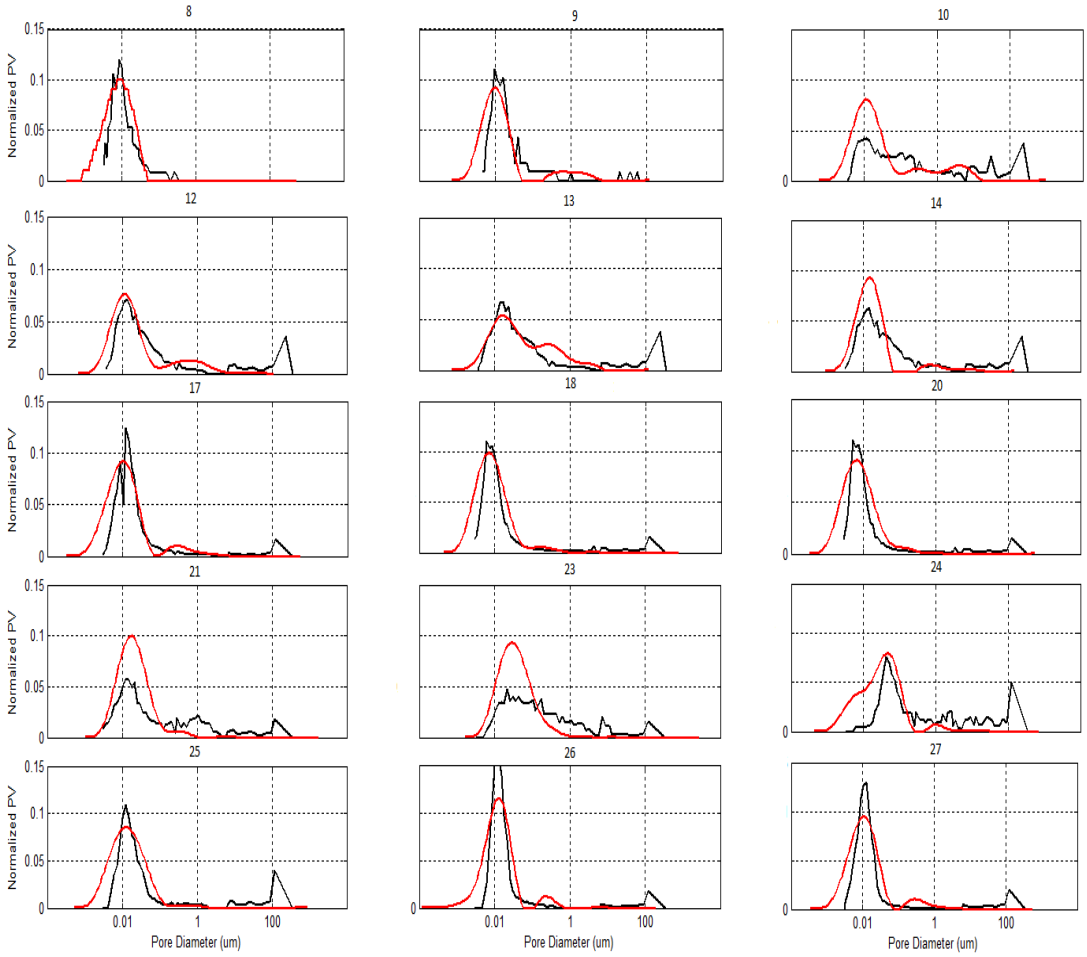

Figure 5-5: Pore diameter. NMR T_2-equivalent pore diameter extracted from equation (5-5) (red) and MICP pore diameter (black)

However, the T_2 relaxation times (PSD) for shales are so low that it is difficult to distinguish or separate the clay-bound water from the capillary-bound water. Furthermore, these high clay content materials have kerogen, a material that contains hydrogen atoms that could possibly be picked up by the NMR signals. The approach described by Zhi-Qiang et al. (2005) is also not applicable for the shale samples in our study because their samples had dominant T_2 relaxation times above 10 msec, whereas the dominant T_2 relaxation time in our study was about 1 msec.

5.2.2 T_2 relaxation time from MICP data

One could also extract the T_2 relaxation time from the MICP data. There are two approaches that would give the same results. The first is through the use of equation (5-4).

1. Multiply the T_2 relaxation time with surface relaxivity.
2. Plot T_2 versus weighted incremental pore volume (from NMR) and MICP Pc equivalent T_2 versus normalized intrusion volume (from MICP) on the same plot. The x-axis will be illustrated in terms of time (μm/ms).

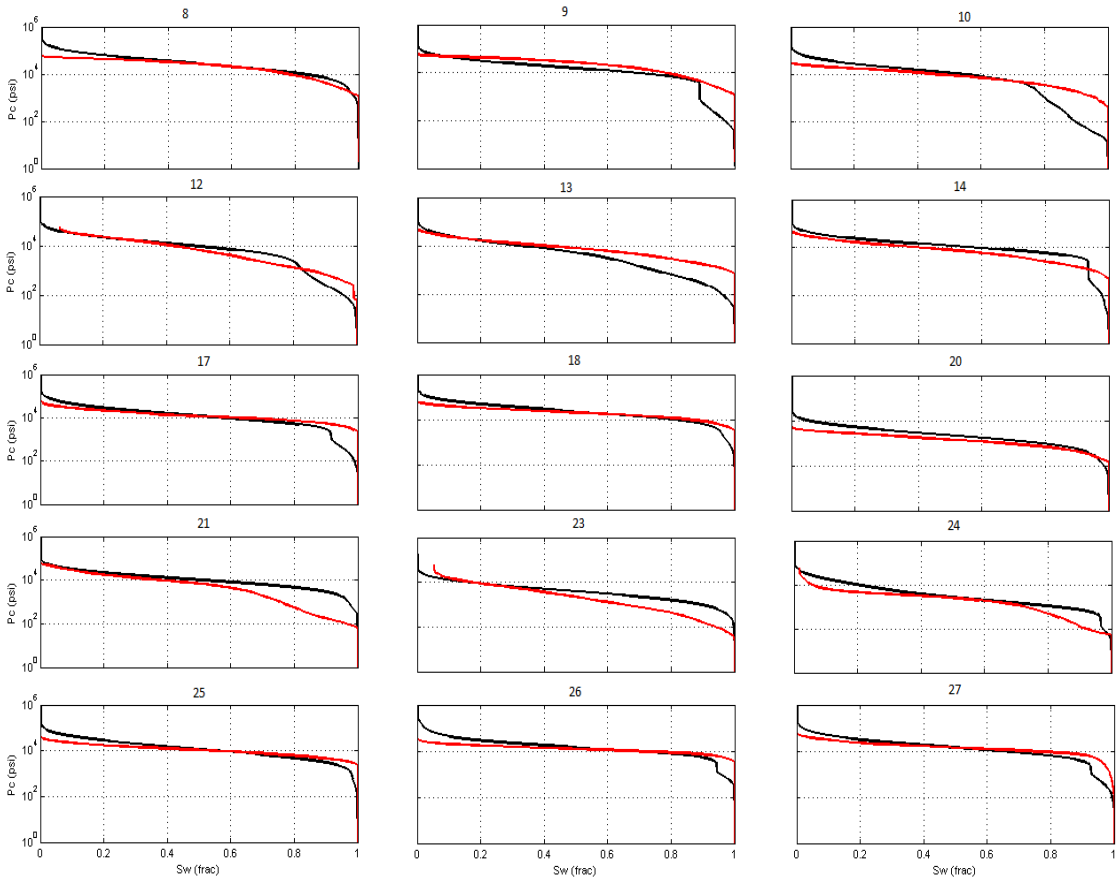

Figure 5-6: Capillary pressure curves. NMR T_2-equivalent Pc extracted from equation (5-6) (red) and MICP intrusion pressure (black)

Table 5-3: Extracted supplemental parameters from NMR and MICP tests

Sample Num.	P_{MICPTh} (psi)	P_{NMRTh}	ρ2 µm/ms	Shift Factor (b)	Scaling Factor (c)
8	6169	5633	0.020	0.11	3.60
9	2337	3390	0.021	0.11	3.50
10	680	1203	0.032	0.11	4.00
12	1795	1382	0.023	0.11	3.70
13	1795	430	0.029	0.19	3.90
14	1701	2850	0.027	0.11	3.90
17	6115	2384	0.011	0.11	3.90
18	10027	5203	0.015	0.11	3.60
20	469	427	0.104	0.01	2.20
21	1259	838	0.036	0.09	4.00
23	218	294	0.253	0.08	3.80
24	1019	1279	0.015	0.09	4.00
25	4460	2506	0.019	0.10	3.60
26	6725	8242	0.004	0.11	3.80
27	5895	2625	0.011	0.11	4.20

P_{MICPTh} is the threshold pressure from MICP, P_{NMRTh} is the threshold pressure from T_2 equivalent pressure, ρ_2 is the surface relaxivity and b and c are shifting factors.

The second approach is based on the use of the surface–volume ratio. This ratio can be determined from the MICP data and then substituted into equation (5-6). The steps are as follows:

1. Determine the surface–volume ratio from the MICP data.
2. With the known surface relaxivity, determine the MICP-equivalent T_2 relaxation time with a scaling factor of c = 3.6.

$$MICP\ equiv.T_2 = \left[1/\left(\rho_2 . \frac{S}{V}\right)\right].c \qquad \text{Equation 5-7}$$

3. Plot NMR T_2 versus the weighted incremental pore volume (from NMR) and the MICP Pc-equivalent T_2 versus the normalized intrusion volume (from MICP) on the same plot.

For the majority of the samples, threshold pressure from the NMR-derived capillary pressure was slightly higher compared to the MICP-derived result (Table 5-3). However, a good trend was observed between MICP and NMR (Figure 5-7).

The advantages of predicting capillary pressure from NMR is that the capillary pressure readings can be continuously determined with depth (Volokitin et al. 1999), and permeability models requiring capillary pressure can be used to estimate permeability. The method is also nondestructive compared to MICP. On the other hand, deriving the T_2 relaxation time from MICP data brings certain advantages, particularly in cases where it is difficult to obtain suitable core plugs for evaluating petrophysical properties of reservoir rocks. The MICP technique measures the pore volume directly and only requires a small rock cutting or fragments; results are obtained relatively quickly with reasonable accuracy, and very high capillary pressure ranges can be achieved.

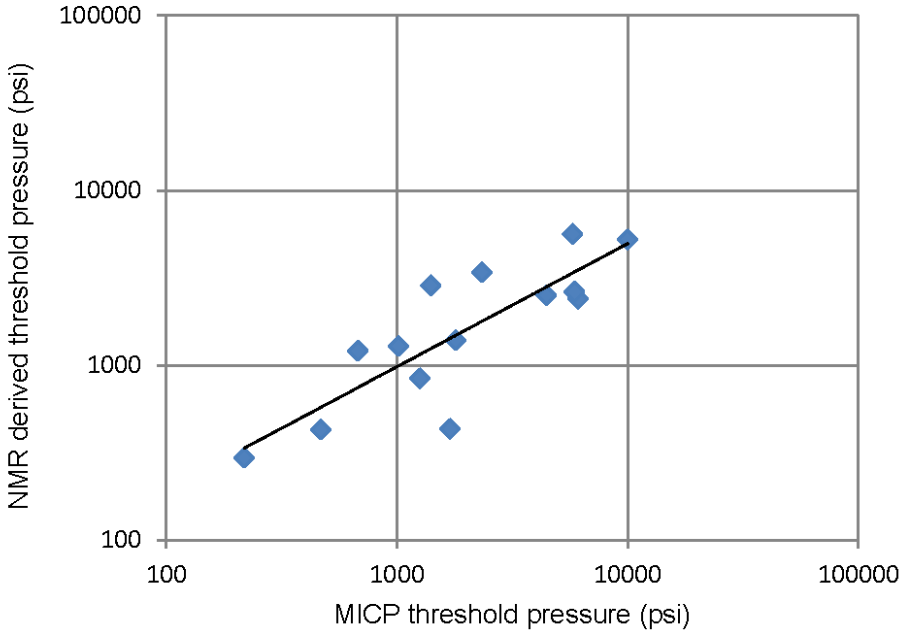

Figure 5-7: Threshold pressure of selected samples directly from MICP experiments and indirectly from NMR derived threshold pressure

5.3 MICP Permeability

Porosity and permeability relationships are qualitative in nature; particular rocks may exhibit high porosity, but ultra-low permeability. Porosity and measured permeability of the samples in the study exhibit a weak correlation (Figure 5-8). This is not unexpected, given that the porosity symbolises the pore volume and the permeability reflects the pore throat size in the system (Al Hinai et al., 2013).

It is believed that transport properties of a tight rock are dictated by the pore structure (Bustin et al., 2008). Many researchers have attempted and developed mathematical models to predict permeability based on pore size such as MICP tests (Pittman, 1992; Rezaee et al., 2006; Dastidar et al., 2007). The aim here was to provide an understanding of the interrelation between fluid flow and the physical properties (pore geometry) of gas shale rocks.

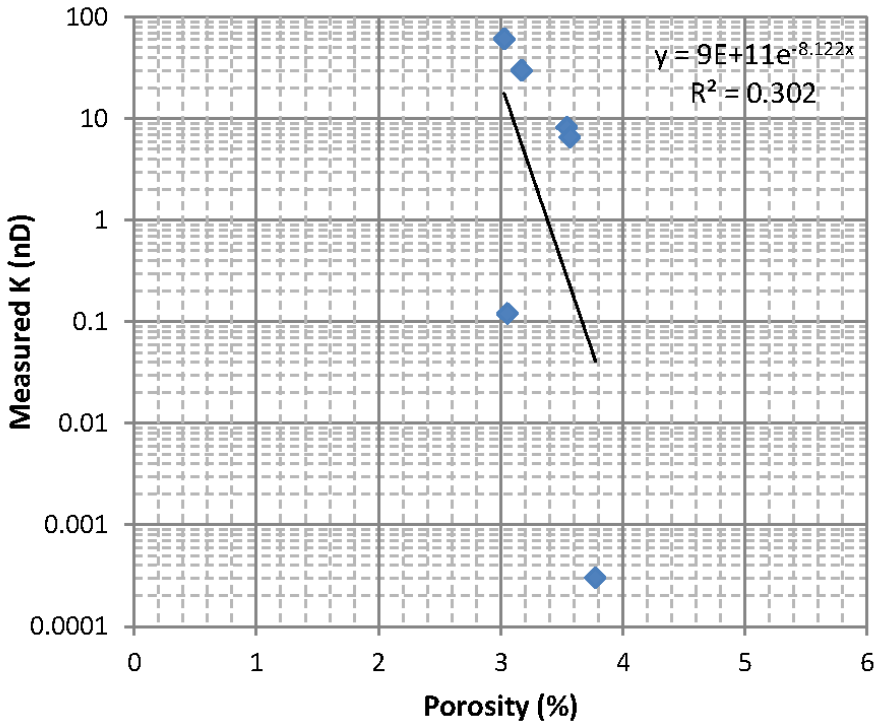

Figure 5-8: Cross plot of MICP porosity versus measured gas permeability

The key objectives of the study are to compare the results of the MICP permeability prediction methods versus laboratory measured permeabilities and to develop an improved relationship between permeability and pore throat size. The results are displayed as log-log plots of measured permeability versus the predicted permeability (Fig 5-9).

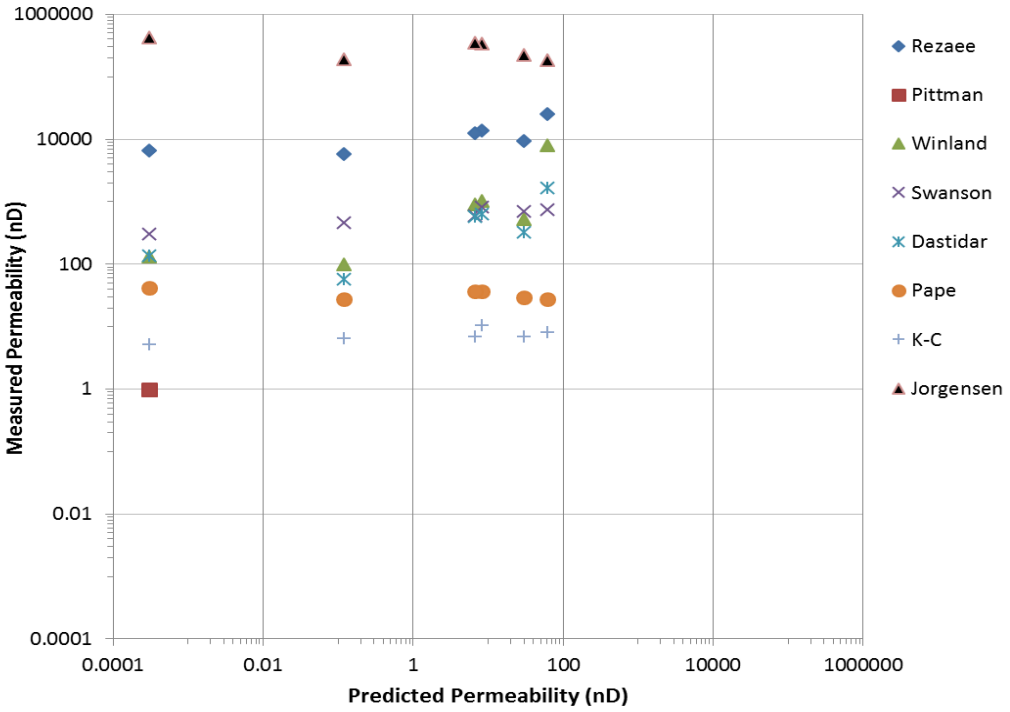

Figure 5-9: Measured permeability vs predicted permeability

The weak correlation between porosity and permeability is not something unexpected, given that the porosity symbolizes the pore volume and permeability reflects the pore throat size in the system. We have tabulated R^2 in increments of 5 (pore throat radius at 15% mercury saturation to 75 mercury saturation) to obtain the best throat size and permeability correlation. R_{75} shows a stronger influence of permeability (Fig 5-10).

The equation found to be suitable for the area studied is given by:

$$\mathrm{LogK} = 37.255 - 6.345\mathrm{Log}\emptyset + 15.227\mathrm{Log}R_{75} \qquad \text{Equation 5-8}$$

where K is measured in nano Darcy, porosity in percentage and R is in micrometers. Most of the permeability estimations from the capillary pressure data [in other studies] are based on a single point on the curve or the full range of the data points. The majority of the techniques in other studies were based on conventional reservoirs, while this study examines rocks with extremely low permeability.

One disadvantage of the Winland equation is that it is based on a simple assumption for a simple pore network such as sandstone (interparticle porosity). In other words, there is a linear relationship between the pore throat size at 35% mercury saturation, porosity and permeability. Similarly, Rezaee (2006) suggested at a throat size at 50% mercury saturation is ideal for carbonates. Permeability values estimated here show that most of the theoretical and empirical values overestimate permeability of shale rocks. This is expected as most of the models are based on sandstone, carbonates and tight sand and these rocks have pore throat radiuses larger than shale. The relationship takes into account both porosity and pore throat size at 75 % mercury saturation. Pore throat radius does not display exclusivity at some definite mercury saturation levels. Every rock may vary in R values depending on its pore structure and geometry.

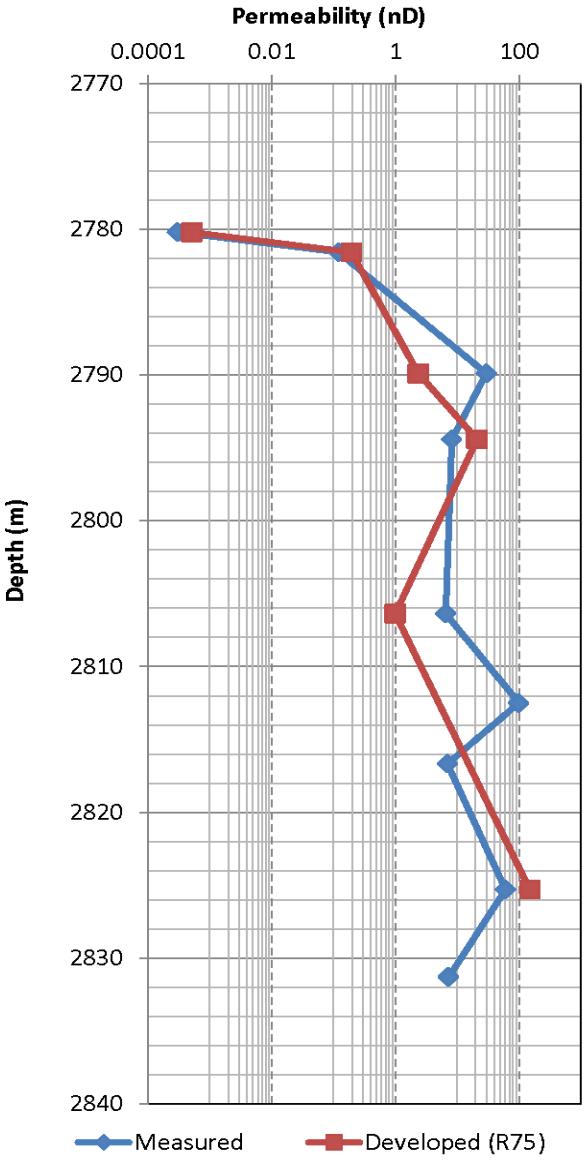

Figure 5-10: Comparison of measured permeability and developed prediction equation vs depth of the analysed samples

5.4 Influence of Clay Types on Pore Size

These siliceous and organically rich gas shales are marked by a strong component of clay minerals, with up to 56% Kaolinite and Illite/Smectite (I/S) mixed layers. It is commonly known that Kaolinite and Illite often control the ability of a fluid to pass through a porous media, and its storage capacity depends not on the amount of these clays sensu-stricto but is strongly dependent on their locations within the pore

network. The small sizes and non-swelling attributes of these clays in the presence of water make them easy for pore filling (typical of Kaolinite) or pore bridging (typical for Illite). However, Smectite is a strong swelling clay when in contact with water and is the origin of many problems during well drilling and production.

The Illite/Smectite mixed layers are therefore slightly swelling clays with structural attributes from both Illite and Smectite clay minerals. Three types of gas shales can be classified according to their clay contents: (i) low I/S but high Kaolinite (CCM); (ii) high I/S but low Kaolinite (PCM); and (iii) high I/S and high Kaolinite (PCM and PKM). The images obtained from SEM show that Kaolinite, dominant in the formation of CCM and the top of PCM, are filling the pores. The I/S clays dominant in the formations of PCM and PKM are mostly found around the pores and coating the grains or often plugging the pore throats. It is therefore expected to see I/S clay bearing formations that are fluid trapping mechanisms leading to degraded flow dynamics. Kaolinite rich formations would be expected to control the water retention amount, depending on the pore size and the amount of Kaolinite that will more or less fill the pore network.

5.4.1 MICP porosity and the presence of clays

Two groups of samples were identified from capillary pressure profiles, showing distinct entry pressures at low pressure and pore saturation at the highest pressure of mercury injection. These two groups are distinctive in their content of I/S clays. The dominant group, mostly composed of PCM and PKM, with high I/S content, records high entry pressure consequent on low pore throat radius. The second group of samples (CCM) with low I/S (but high Kaolinite) has lower entry pressure and never reaches full saturation, up to 60,000 psi of pressure applied on the mercury. This illustrates that I/S clays are prone to degrade fluid flow efficiency much more than Kaolinite rich clay formations, as shown in the I/S that clogs part of the pore throats, leading to a “tight” pore structure (Figure 5-11). This contrasts with the Kaolinite rich formations that record the lowest entry pore pressure and the highest porosities (Table 5-4).

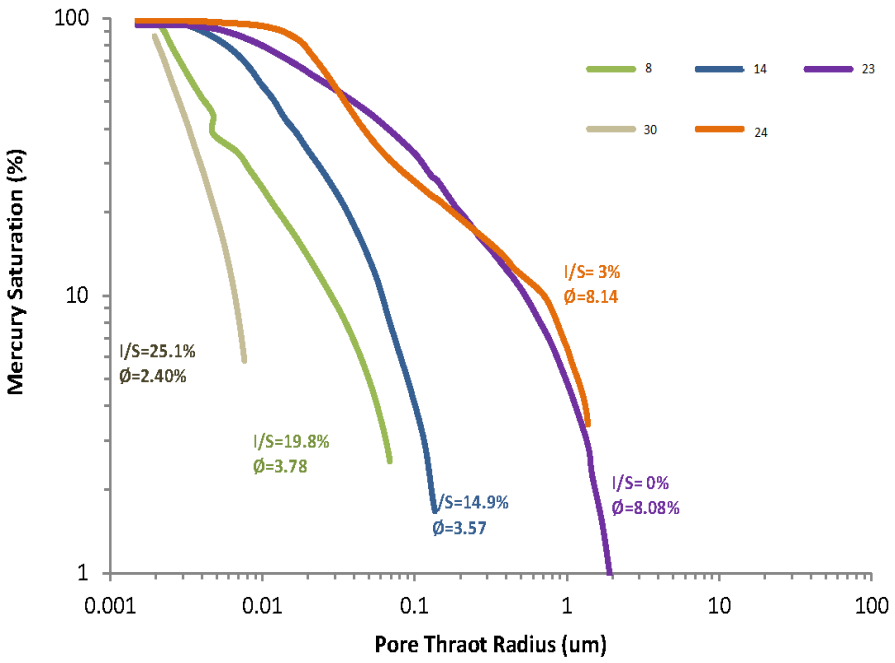

Figure 5-11: Log-log graph of mercury injection versus pore throat size showing how illite to smectite ratio decreases when the pore throat size decreases on high porosity selected gas shale samples

Table 5-4: MICP threshold pressure of the samples with clay content

ID	Porosity MICP (%)	Entry Pressure (psi)	Quartz	Mixed Illite / Smectite (20%)	Kaolinite
1	6.2	1394	15.1	6.4	28.3
3	7.7	246	14.7	12	29.1
8	3.78	6196	24.5	19.8	2.6
13	3.54	1795	53	11.7	0.8
14	3.57	1701	41.3	14.9	0.8
17	7.22	6115	51.1	5.8	19.7
18	8.43	10027	47.2	-	27.8
19	6.52	7347	54.1	-	25.6
20	8.5	469	56.1	-	21.5
21	9.02	1259	45.6	-	26.8
23	8.08	218	67.1	-	11.3
24	8.14	1019	60.5	3	22.6
25	4.18	4460	67.2	-	13.8
26	7.41	6725	50.5	4.1	25.1
27	6.98	5895	34.2	7.2	17.6
30	2.4	11585	23.3	25.1	16.3
31	2.4	4942	15.5	27.7	10.5

5.4.2 Mixed Illite/Smectite effects on surface area from N_2 experiment

The BET surface areas were found to be 2 to 8 m^2/gr for both PCM and CCM formations,, with the exception of sample 27 < 10 m^2/gr. There was no direct relationship found between the BET surface area, the occurrence of Illite/Smectite, and the total clay content. Based on the IUPAC pore classification, N_2 pore volumes showed a pore range from 60–90% meso-pores, 6 to 34% macro-pores, and a small portion of 1 to 11% micro-pores (Figure 5-12).

In addition, the N_2 adsorption and desorption curves for the tested samples indicate that the change in I/S to Kaolinite ratio has an effect on the profile (i.e. shape of the curve) (Figure 5-13). The samples with the least kaolinite content have a narrow separation, quasi-superimposed, between the adsorption and desorption curves at high relative pressure, while samples with higher kaolinite content showed high separation. Also, the quantity of N_2 adsorbed increases as kaolinite increases. If we compare samples 21 and 25, we can see that sample 25 has 13.8% kaolinite, and sample 21 has a twofold higher concentration at 26.8%. The amount of N_2 adsorbed in mmol/g increased from 0.27 (sample 25) to 0.77 (sample 20).

This behaviour is also confirmed in samples 8, 13 and 27, where the I/S to kaolinite ratio effect ranges from high to low. At a low ratio of I/S to kaolinite (i.e. high kaolinite content), the separation and quantity of N_2 adsorbed is large. In other words, if the desorption profile is similar to the adsorption profile, the N_2 is adsorbed at the same rate and amount as increasing pressure is released during the desorption process. When a separation appears between the N_2 profiles, typically more N_2 is released during desorption than during adsorption, and there is very little fluid trapping effect. It is basically easy to release gas that is typically related to the amount of kaolinite and is stored in the pore network. A high amount of kaolinite will store a lot of gas during adsorption and will desorb much more quickly and at a high rate as soon as the pressure decreases.

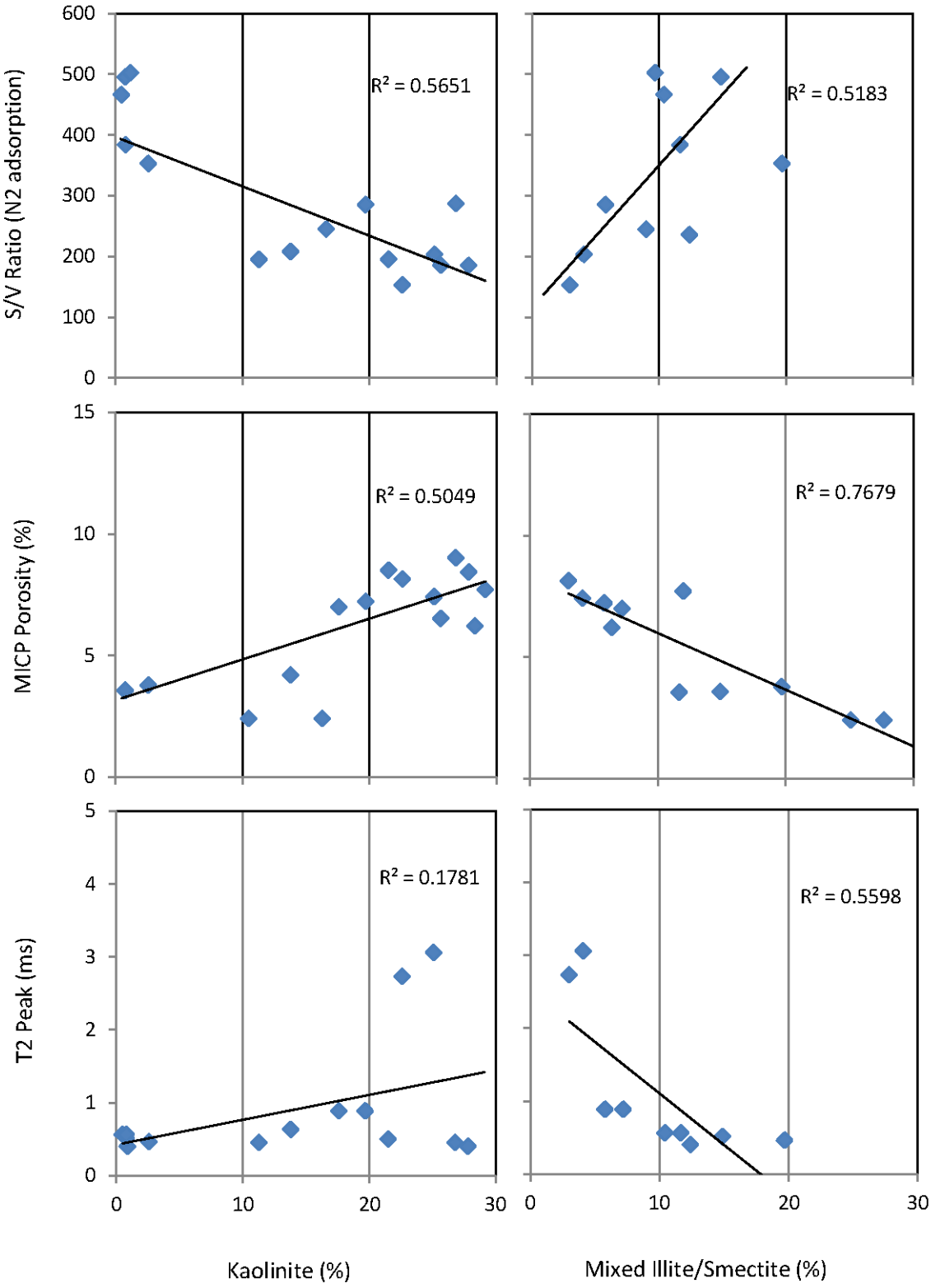

Figure 5-12: Influence of I/S and Kaolinite on various parameters

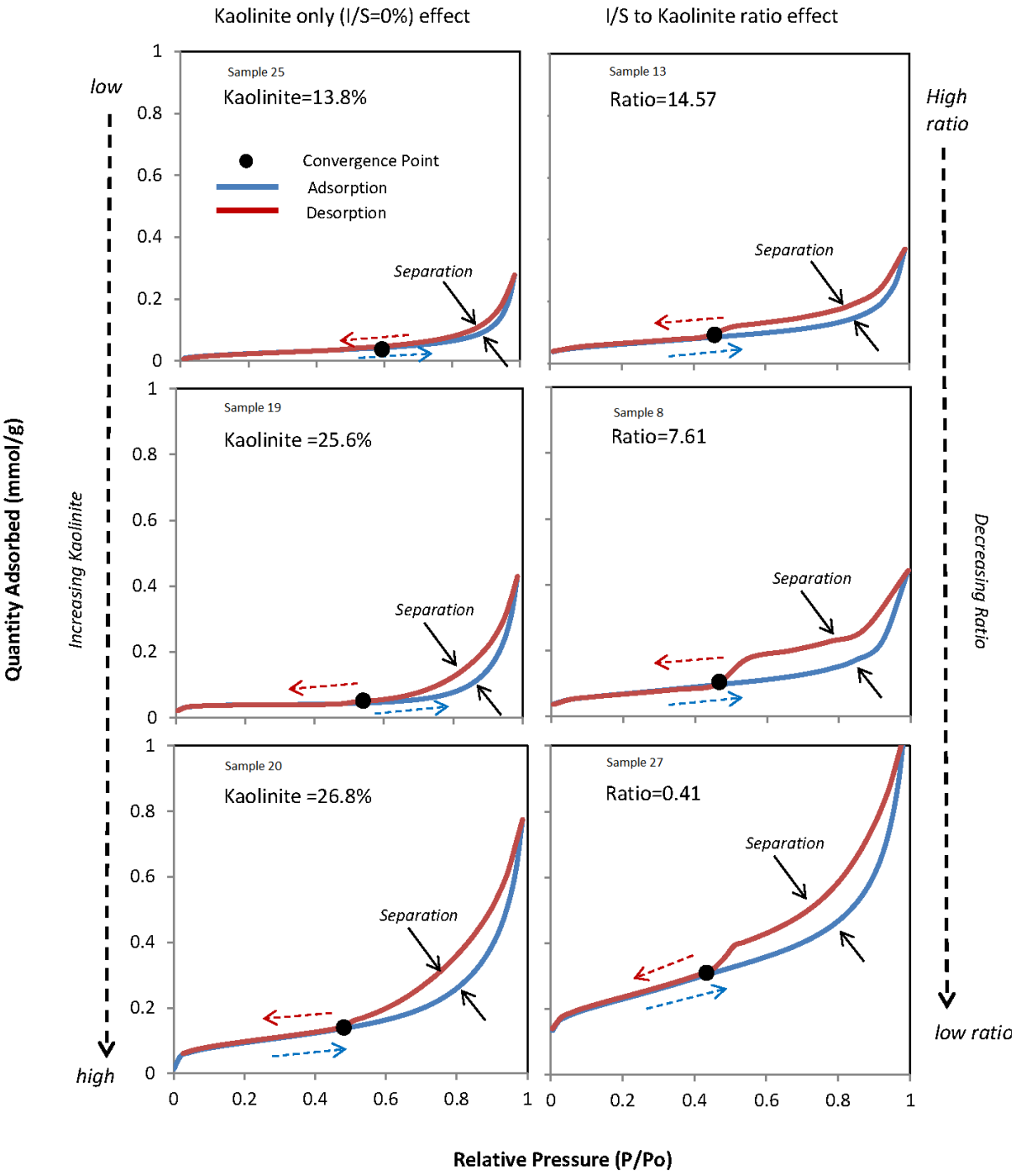

Figure 5-13: Quantity of N_2 adsorbed versus relative pressure at various I/S and Kaolinite contents. (Left column) Samples with low kaolinite content have a narrow separation between the adsorption and desorption lines at high relative pressure. The quantity adsorbed increases as kaolinite content increases. (Right column) A low ratio I/S to kaolinite, the separation & the quantity adsorbed increases.

5.4.3 Effects of clay on T_2 relaxation time

CCM has a lower percentage of mixed Illite/Smectite clays but a higher kaolinite percentage compared to the PCM formation (Appendix 1: XRD results). Furthermore, the presence of mixed Illite/Smectite influences the NMR response (Figure 5-12). As the clay component of mixed Illite/Smectite increases, the T_2 relaxation time tends to decrease, corresponding to smaller pore sizes or restricted environment (higher specific surface area and/or stronger grain surface relaxation effect on proton spin). This contrast with kaolinite shows little influence on the T_2 values that remains constant no matter the amount of kaolinite.

The presence of the swelling clay (smectite) could have been responsible for blocking the pore throats, or in a more general view, the pore connectivity that allows the fluids to access neighbouring pores during the saturation process, leading to lower T_2 amplitude values. The long T_2 represents macro-pores that are potentially new cracks induced by the artificial brine reactivity during re-saturation with the shales, and by mechanical damage inherited during the sample recovery up to the sample preparation.

5.4.4 Surface to Volume Ratio (S/V) and Mineralogy

The tested shale samples contain an average of 37% clay content for CCM, 42% for PCM and 51% for PKM. It is expected that (S/V) should be high for these clay rich samples. To illustrate this postulate, nitrogen adsorption measurements seem more appropriate to use than MICP data, as MICP determines only the connected pores, missing the isolated pores. Using the BET method, the surface area was determined from the N_2 adsorbed volume at maximum relative pressure. N_2 results presented higher average pore throat radii for CCM (9.2 ± 2.4 nm) samples compared to PCM ones (5.2 ±1.5 nm).

Similarly, the total pore volume is determined to be 2 ± 0.9 cm3/gr and 1.4 ± 0.2 cm^3/gr for CCM and PCM, respectively (Table 5-5). Both the presence of Kaolinite and mixed Illite/Smectite show a reasonable trend with the S/V (Figure 5-12). Kaolinite decreases with the increase in S/V, while mixed I/S increases with the increase in S/V. This demonstrates that a larger I/S content is found in shales that exhibit larger surface to volume ratio (Howard, 1991).

Table 5-5: Surface to volume ratio from N_2 experiments

SAMPLE ID	BET Surface Area (m^2/gr)	Total Pore Vol. (cm^3/100gr) at maximum pressure	Average Pore Radius (nm)	Average pore width (4V/A) (nm)	S/V ratio
8	5.43	1.54	5.66	11.32	3.53
9	7.57	1.67	4.41	8.82	4.53
11	2.34	0.99	8.5	17	2.36
12	4.28	1.19	5.57	11.14	3.60
13	4.91	1.28	5.21	10.42	3.84
14	7.79	1.57	4.04	8.08	4.96
15	5.98	1.28	4.29	8.58	4.67
16	7.79	1.55	3.985	7.97	5.03
17	8.66	3.04	7.02	14.04	2.85
18	3.39	1.83	10.82	21.64	1.85
19	2.75	1.49	10.8	21.6	1.85
20	2.77	1.42	10.485	20.97	1.95
21	7.7	2.69	6.98	13.96	2.86
22	3.41	1.39	8.18	16.36	2.45
23	2.03	1.04	10.28	20.56	1.95
24	2.08	1.36	13.085	26.17	1.53
25	2	0.96	9.62	19.24	2.08
26	6.26	3.09	9.86	19.72	2.03
27	18.02	3.6	3.99	7.98	5.01

5.4.5 Clay influence on fluid flow properties

When gathering all the experimental results from MICP, NMR and N_2 adsorption along with mineralogical information from XRD and structures from SEM images, three general fluid flow behaviours of these gas shales can be discriminated:

(1) I/S clay mineral as the dominant clay phase (> 15%):

The I/S clays are known to have larger surface area, thus creating small pore volumes. Thus generating very small pore throats but also creates very complex pore geometry. Such geometry leads to trapping volume of fluids, as attested by nitrogen adsorption, and degrade the flow properties of the rock in the same time. The swelling mechanism of smectite in the interstratified I/S clay structures observed from NMR results will block even more the pore throats when exposed to

water/drilling mud, making such formation a poor candidate to flow water and/or hydrocarbons. It is the ideal formation to trap hydrocarbon/water fluids within the pore network but the volume of fluid storage will be very low.

(2) Kaolinite clay minerals as the dominant clay phase (>15%):

The kaolinite rich gas shales present opposite behavior to the I/S rich clay formations. The entry pore pressure is much smaller that ease the flow dynamics with bigger pores and a smooth pore geometry that avoid too much fluid trapping as illustrated by MICP and N_2 adsorption methods. This low trapping effect and high storage capacity seen by nitrogen adsorption make such formation ideal to fluid flow. But if no trapping mechanism can play, no hydrocarbon will be stored inside the pore network. It will therefore act as a basic sealing formation.

(3) Quartz minerals as the dominant phase with small amount of clays (<15%):

The porosity and pore size are too high and clays cannot hold properly hydrocarbon fluids. It is the worst scenario for hydrocarbon storage. When the amount of clay reach a critical amount, the clay types combined to their locations will govern the way of trapping and the flow dynamics. It is then fundamental to understand the distribution of the clays and the type of clays, if accurate predictions of fluid production and/or fluids storage need to be assessed from gas shale reservoirs.

The best conditions are found when some fluid trapping mechanisms can occur with I/S clays and when storage capacity can also play with the help of kaolinite. Therefore, when enough clay minerals occur within gas shales with a good equilibrium of kaolinite and I/S clays, such formation become the best target for hydrocarbon storage and production (Figure 5-14).

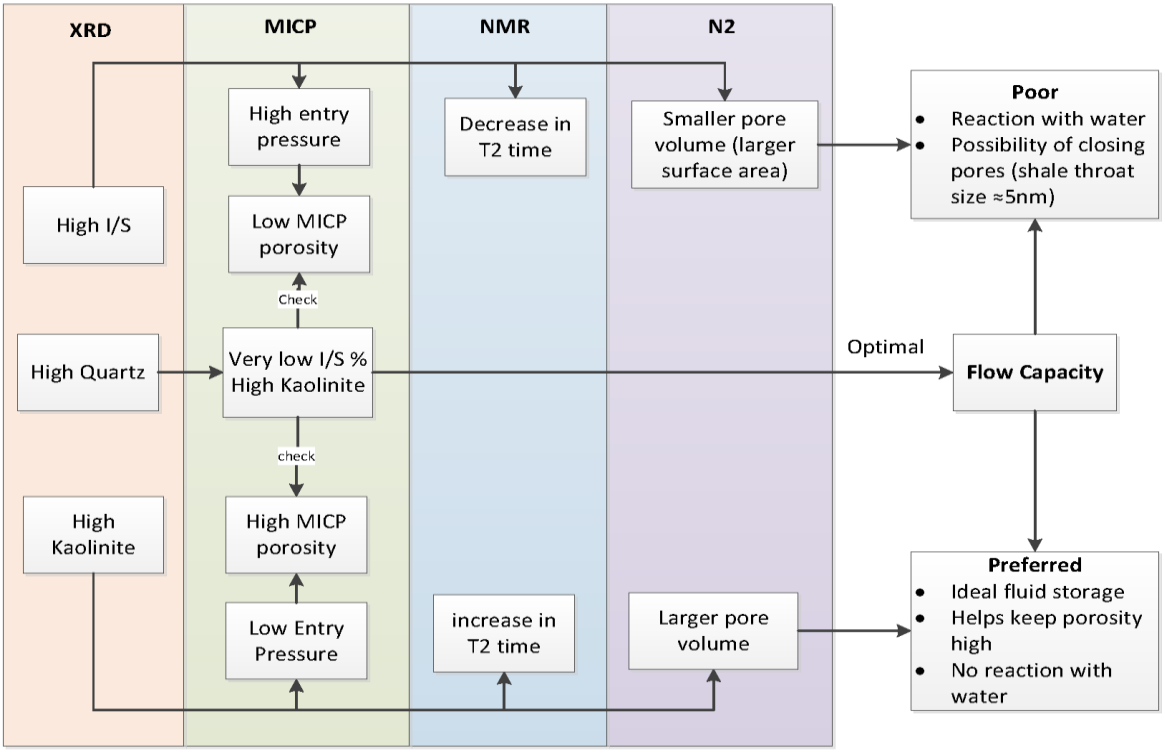

Figure 5-14: Flow chart summarising flow capacity scenarios

6. CHAPTER 6: CONCLUSIONS

Five laboratory techniques have been utilized to assess the full pore size structures of the PCM and PKM shale formations at the core sample scale: MICP, N_2 adsorption, low field NMR, SEM and FIB/SEM. The following conclusions can be reached about the pore structure assessment of these gas shale formations:

(1) MICP is relatively fast, and seems to be a reliable method to understand the pore throat size distribution down to 3 nm and determine most of the porosity involved in the fluid transport, despite the dry state of gas shale samples.

(2) N_2 adsorption analysis can effectively reveal information about the pore size distribution in the micro-pore range (< 2 nm) that is not accessible by MICP and limited in low field NMR resolution.

(3) When comparing low pressure N_2 adsorption pore volumes with MICP, a discrepancy was found when classifying the pore size. The inconsistency comes from MICP that quantifies pore throat sizes and not the pore bodies, while N_2 pore volumes provide both pore size types.

(4) It is suggested that NMR is an applicable non-destructive method to examine the water content and the pore body size distribution to further characterize the pore geometry of gas shale deposits. The porosity from NMR is always larger than MICP and N_2 porosity. NMR measures both connected and unconnected pores at all scales. However, as for MICP, the micro-porosity remains difficult to access with a 2 MHz NMR apparatus and the NMR logging tools.

(5) Clay rich rocks show complex pore geometry that directly controls the permeability within the same formation, while porosity and pore size distributions remain quasi-similar.

(6) SEM images have supported the discerned trends in mineralogical samples obtained by XRD. The large dominating quartz particles are found throughout the samples of PCM and CCM. Typical clay platelets of Illite and Illite/Smectite were found alongside the quartz particles. Additionally, secondary minerals were shown to be intermixed with the dominant quartz and clay particles. Macro- and meso-porosity was displayed in the images, with voids as large as a few micron (~3 µm) being viewed at particle

boundaries. Micro-porosity is expected; however, SEM imaging did not display these pores due to machine limitations.

(7) MICP porosity involves only the connected porosity that is responsible for the fluid transport property. MICP porosity is proportional to Kaolinite content and the connectivity of the system favours Kaolinite.

(8) The increased content of I/S restricts the flow of mercury into the sample, thus the high displacement pressure and the pore throat size distribution range decreases.

(9) Optimum conditions would be lots of Kaolinite with a bit of I/S and quartz, which will store HC/fluids and trap enough volume to create a valuable reservoir.

(10) The increase in I/S presence in the rock shows an increase in surface to volume ratio from N_2 adsorption tests, and the opposite behaviour is found with an increase in Kaolinite.

(11) Pore geometry is a function of shape and is conditioned by the types of clay. There is no relationship between porosity and permeability in shale as there is in sandstone/carbonates.

5. REFERENCES

Al-Bazali, Talal M., Jianguo Zhang, Martin E. Chenevert, and Mukul Mani Sharma. 2005. "Measurement of the Sealing Capacity of Shale Caprocks." Paper presented at *SPE Annual Technical Conference and Exhibition, Dallas, Texas, 9-12 October*. doi: 10.2118/96100-MS.

Al-Raoush, R. I. & Willson, C. S. (2005). Extraction of physically realistic pore network properties from three-dimensional synchrotron X-ray microtomography images of unconsolidated porous media systems. *Journal of Hydrology* **300**, 44-64.

Allen, Terence. 1997. *Particle Size Measurement*. New York: Chapman and Hall.

Barret, E.P., Joyner, L.G., Halenda, P.P., 1951. "The determination of pore volume and area distribution in porous substances: Computations from nitrogen isotherms". *Journal of American Chemical Society 73, 373-380.*

Beilby, P. S. 1998. "Pore Scale Modelling of NMR Response in Mixed Porous Media." Paper presented at *European Petroleum Conference, The Hague, Netherlands, 20-22 October*. doi: 10.2118/52084-STU.

Boudier, Thomas. 2014. "3D Processing and Analysis with ImageJ." Paris: Université Pierre et Marie Curie. Accessed April 16

Boyer, Charles, John Kieschnick, Robert Suarez-Rivera, Richard E. Lewis, and George Waters. 2006. "Producing Gas from Its Source." *Oilfield Review* 18 (3): 36-49.

Brunauer, Stephen, Lola S. Deming, W. Edwards Deming, and Edward Teller. 1940. "On a Theory of the van der Waals Adsorption of Gases." *Journal of the American Chemical Society* 62 (7): 1723–1732.

Burdine, N. T., L. S. Gournay, and P. P. Reichertz. 1950. "Pore Size Distribution of Petroleum Reservoir Rocks." *Journal of Petroleum Technology* 2 (7): 195-204.

Bustin, R. Marc, Amanda M. M. Bustin, Albert Cui, Daniel, Ross, and Venkat Murthy Pathi. 2008. "Impact of Shale Properties on Pore Structure and Storage

Characteristics." Paper presented at *SPE Shale Gas Production Conference, Fort Worth, Texas, 16-18 November.* doi: 10.2118/119892-MS.

Butcher, Alan R., and Herman J. Lemmen. 2011. "Advanced SEM Technology Clarifies Nanoscale Properties Of Gas Accumulations In Shales." *The American Oil and Gas Reporter* July:

Chalmers, G.R., Bustin, R.M., Power, I.M., 2012. "Characterization of gas shale pore systems by porosimetry, pycnometry, surface area, and field emission scanning electron microscopy/transmission electron microscopy image analyses: Examples from the Barnett, Woodford, Haynesville, Marcellus, and Doig units". *AAPG Bulletin 96, 1099-1119.*

Chen, Quan, and Y. –Q Song. 2002. "What is the Shape of Pores in Natural Rocks?" *The Journal of Chemical Physics* 116: 8247-8250.

Churcher, P. L., French, P. R., Shaw, J. C. & Schramm, L. L. 1991. "Rock Properties of Berea Sandstone, Baker Dolomite, and Indiana Limestone". *SPE International Symposium on Oilfield Chemistry. Anaheim, California.*

Clarkson, C. R., N. Solano, Bustin, R. M. Bustin, A. M. M. Bustin, G. R. L. Chalmers, L. He, Y. B. Melnichenko, A. P. Radlin, and T. P. Blach. 2013. "Pore Structure Characterization of North American Shale Gas Reservoirs Using USANS/SANS, Gas Adsorption, and Mercury Intrusion." *Fuel* 103: 606-616.

Coates, George R., Lizhi Xiao, and Manfred G. Prammer. 1999. *NMR Logging Principles and Applications*. Houston: Halliburton Energy Services.

Cohen, Morrel H., and Kenneth S. Mendelson. 1982. "Nuclear Magnetic Relaxation and the Internal Geometry of Sedimentary Rocks." *Journal of Applied Physics* 53: 1127-1135.

Comisky, Joseph Thomas, Kent Newsham, Jay Alan Rushing, and Thomas Alwin Blasingame. 2007. "A Comparative Study of Capillary-Pressure-Based Empirical Models for Estimating Absolute Permeability in Tight Gas Sands."

Paper presented at *SPE Annual Technical Conference and Exhibition, Anaheim, California, 11-14 November*. doi: 10.2118/110050-MS.

CSIRO (Commonwealth Scientific and Industrial Research Organisation). 2013. "Australia's Shale Gas Resources." Commonwealth Scientific and Industrial Research Organisation.

Dastidar, Rahul, Carl H. Sondergeld, and Chandra S. Rai. 2007. "An Improved Empirical Permeability Estimator From Mercury Injection For Tight Clastic Rocks." *PetroPhysics* 48 (3): 186-190.

De Boer, J.H., 1958. "The structure and properties of porous materials". Proceedings of the tenth symposium of the Colston Research Society held in the University of Bristol, Butterworths, London, 68-94

Dollimore, D., Heal, G.R., 1964. An improved method for the calculation of pore-size distribution from adsorption data. Journal of Applied Chemistry 14, 109-114.

Dougherty, Edward R., and Roberto A. Lotufo. 2003. *Hands-on Morphological Image Processing*. Washington: SPIE Press.

Education, M. H. H. 2000. Chapter 13: Spectroscopy. Organic Chemistry 4e Carey, Online Learning Center: *The McGraw-Hill Companies.*

Evdokimov, Igor N., Nikolai Yu Eliseev, Aleksandr P. Losev, and Mikhail A. Novikov. 2006. "Emerging Petroleum-Oriented Nanotechnologies for Reservoir Engineering." Paper presented at *SPE Russian Oil and Gas Technical Conference and Exhibition, Moscow, 3-6 October*. doi: 10.2118/102060-RU.

Fibics. 2011. *Introduction: Focused Ion Beam Systems*. http://www.fibics.com/fib/tutorials/introduction-focused-ion-beam-systems/4/ (accessed 14 June).

Fleming, P. D. 1983. *An Interpretation of the Petrophysical Properties of Reservoir Rocks Based on Percolation Theory*. Richardson, Texas: Society of Petroleum Engineers.

Gale, Julia F. W., Robert M. Reed, and Jon Holder. 2007. "Natural Fractures in the Barnett Shale and their Importance for Hydraulic Fracture Treatments." *AAPG Bulletin* 91 (4): 603-622.

Giesche, Herbert. 2006. "Mercury Porosimetry: a General (Practical) Overview." *Particle & particle systems characterization* 23 (1): 9-19.

Granier, Bruno. 2003. "A New Approach in Rock-typing, Documented by a Case Study of Layer-cake Reservoirs in Field "A", Offshore Abu Dhabi (U.A.E.)." *Carnets de Géologie / Notebooks on Geology*. A04 (July): 1-13.

Gregg, S. J. & Sing, K. S. W. (1991). Adsorption, surface area and porosity. *Academic Press: London*, 303.

Heath, Jason E., Thomas A. Dewers, Brian J. O. L. McPherson, Robin Petrusak, Thomas C. Chidsey, Alex J. Rinehart, and Peter S. Mozley. 2011. "Pore Networks in Continental and Marine Mudstones: Characteristics and Controls on Sealing Behavior." *Geosphere* 7 (2): 429-454.

Hidajat, Irwan, Mohit Singh, and Kishore K. Mohanty. 2003. "NMR Response of Porous Media by Random Walk Algorithm: A parallel Implementation." *Chemical Engineering Communications* 190 (12): 1661 - 1680.

Hildenbrand, A., and J. L. Urai. 2003. "Investigation of the Morphology of Pore Space in Mudstones—First Results. Marine and Petroleum." *Geology* 20 (10): 1185-1200.

Hornak, Joseph P. 2011. *The Basics of NMR*. n.p: J. P. Hornak.

Howard, James. J. 1991. "Porosimetry Measurements of Shale Fabric and its Relationship to Illite/Smectite Diagenesis." *Clays and Clay Minerals* 39 (4): 355-361.

IHS. 2014. “Information on Australia, Perth Basin Monitor Report”. Basin Monitor and Worldwide Maps Ordering Service. IHS. http://maps.ihs.com/basin-monitor-ordering-service/australasia/perth-basin-monitor-report.html (assecced 14 June)

Jarvie, Daniel M., Ronald J. Hill, Tim E. Ruble, and Richard M. Pollastro. 2007. “Unconventional Shale-gas Systems: The Mississippian Barnett Shale of North-central Texas as One Model for Thermogenic Shale-gas Assessment.” *AAPG Bulletin* 91 (4): 475-499.

Jennings, Jeffrey. B. 1987. “Capillary Pressure Techniques: Application to Exploration and Development Geology". *AAPG Bulletin* 71 (10): 1196-1209.

Jones, F. O. & Owens, W. W. (1980). A Laboratory Study of Low-Permeability Gas Sands. *SPE Journal of Petroleum Technology* **32**, 1631-1640.

Jorgensen, Donald G. 1988. “Estimating Permeability In Water-saturated Formations.” *The Log Analyst* 29 (6): 9.

Josh, M., L. Esteban, C. Delle Piane, J. Sarout, D. N. Dewhurst, and M.B. Clennell. 2012. “Laboratory Characterisation of Shale Properties.” *Journal of Petroleum Science and Engineering* 88–89: 107-124.

Kale, Sagar, Chandra Rai, and Carl Sondergeld. 2010a. “Rock Typing in Gas Shales.” Paper presented at *SPE Annual Technical Conference and Exhibition, Florence, Italy, 19-22 September.* doi: 10.2118/134539-MS.

Kale, Sagar, Chandra Rai, and Carl Sondergeld. 2010b. “Petrophysical Characterization of Barnett Shale.” Paper presented at *SPE Unconventional Gas Conference, Pittsburgh, Pennsylvania, 23-25 February.* doi: 10.2118/131770-MS.

Kanj, Mazen Y., Jim J. Funk, and Zuhair Al-Yousif. 2009. “Nanofluid Coreflood Experiments in the ARAB-D.” *Paper presented at SPE Saudi Arabia Section Technical Symposium, AlKhobar, Saudi Arabia, 9-11 May*. doi: 10.2118/126161-MS.

Katz, A. J. & Thompson, A. H. (1986). Quantitive Prediction of Permeability in Porous rock. *Physical Review* **34**, 8179.

Kenyon, W. E., Takezaki, H., Straley, C., Sen, P. N., Herron, M., Matteson, A. & Petricola, M. J. (1995). A Laboratory Study of Nuclear Magnetic Resonance Relaxation and its Relation to Depositional Texture and Petrophysical Properties - Carbonate Thamama Group, Mubarraz Field, Abu Dhabi. *Middle East Oil Show*. Bahrain: 1995 Copyright 1995, Society of Petroleum Engineers, Inc

King, George Everette. 2010. "Thirty Years of Gas Shale Fracturing: What Have We Learned?" Paper presented at *SPE Annual Technical Conference and Exhibition, Florence, Italy, 19-22 September*. doi: 10.2118/133456-MS .

Kolodzie, S. (1980). Analysis of pore throat size and use of the Waxman-Smits equation to determine OOIP in Spindle Field, Colorado. *Society of Petroleum Engineers, 55th Annual Fall Technical Conference*, Paper 9382.

Kuila, U. and Prasad, M. 2011. "Surface Area and Pore-size Distribution in Clays and Shales". *SPE Annual Technical Conference and Exhibition. Denver, Colorado, USA: Society of Petroleum Engineers.*

Kuuskraa, Velo, Scott Stevens, Tyler Van Leeuwen, and Keith Moodhe. 2011. *World Shale Gas Resources: An Initial Assessment of 14 Regions Outside the United States.* Washington, DC: Energy Information Administration.

Lasswell, Pat. 2013. "Steady State Permeability Analysis in Unconventional Plays." Paper presented at *GeoConvention 2013: Integration, Calgary, 6-10 May.*

Looyestijn, W.J. "Distinguishing Fluid Properties and Producibility from Nmr Logs." Paper presented at the 6th Nordic Symposium on Petrophysics, Norway, 2001.

Lowden, Ben. 2009. "Some Simple Methods for Refining Permeability Estimates from Nmr Logs and Generating Capillary Pressure Curves ". Suffolk: ResLab-ART.

Lu, Xiao-Chun, G. P. Pepin, R. M. Moss, and A. T. Watson. 1992. “Determination of Gas Storage in Devonian Shales With X-Ray-Computed Tomography.” Paper presented at *SPE Annual Technical Conference and Exhibition, Washington, DC, 4-7 October.* doi: 10.2118/24810-MS.

Ma, Shouxiang, Mind-Xuan Jiang, and N. R. Morrow. 1991. “Correlation of Capillary Pressure Relationships and Calculations of Permeability.” Paper presented at *SPE Annual Technical Conference and Exhibition, Dallas, Texas, 6-9 October.* doi: 10.2118/22685-MS.

Marschall, D., Gardner, J.S., Mardon, D. and Coates, G.R. 1995. “Method for correlating NMR relaxometry and Mercury Injection Data”. Paper presented at SCA Conference. Paper number 9511.

Minh, C. C. & Sundararaman, P. (2006). NMR Petrophysics in Thin Sand/Shale Laminations. *SPE Annual Technical Conference and Exhibition*. San Antonio, Texas, USA.

Mory, Arthur John, and Robert Paul Iasky. 1996. *Stratigraphy and structure of the onshore northern Perth Basin, Western Australia Western Australia: Western Australia Geological Survey, Report 46.* Perth: Geological Survey of Western Australia.

Nelson, P. H. 2009. “Pore-throat Sizes in Sandstones, Tight Sandstones, and Shales.” *AAPG Bulletin* 93 (3): 329-340.

Olah, George A., Alain Goeppert, and G. K. Surya Prakash. 2006. *Beyond Oil and Gas : the Methanol Economy.* Weinheim: Wiley-VCH.

Øren, P. E., Antonsen, F., Rueslåtten, H. G. and Bakke, S. 2002. “Numerical Simulations of NMR Responses for Improved Interpretations of NMR Measurements in Reservoir Rocks.” Paper presented at *SPE Annual Technical Conference and Exhibition, San Antonio, Texas, 29 September-2 October.* doi: 10.2118/77398-MS.

Osment, P. A., K. J. Packer, M. J. Taylor, J. J. Attard, T. A. Carpenter, L. D. Hall, N. J. Herrod, S. J. Doran, R. F. Gordon, K. J. Packer, E. L. Hahn, E. R. Andrew,

P. A. Bottomley, I. R. Young, A. N. Garroway, J. Frahm, and E. W. Randall. 1990. "NMR Imaging of Fluids in Porous Solids [and Discussion]." *Philosophical Transactions: Physical Sciences and Engineering* 333 (1632): 441-452.

Owolabi, O. O., and R. W. Watson. 1993. "Estimating Recovery Efficiency and Permeability From Mercury Capillary Pressure Measurements for Sandstones." Paper presented at *SPE Eastern Regional Meeting, Pittsburgh, Pennsylvania, 2-4 November*. doi: 10.2118/26936-MS.

Pape, Hansgeorg, Christoph Clauser, and Joachim Iffland. 1998. "Permeability Prediction For Reservoir Sandstones And Basement Rocks Based On Fractal Pore Space Geometry." Paper presented at *1998 SEG Annual Meeting, New Orleans, Louisiana, 13-18 September*. doi: 10.1190/1.1820060.

Pittman, E. D. (1992). Relationship of Porosity and Permeability to various Parameters Derived from Mercury Injection-Capillary Pressure Curve for Sandstone. *AAPG Bulletin* **76**, 191.

Prodanovic, M., W. B. Lindquist, and R. S. Seright. 2006. "Porous Structure and Fluid Partitioning in Polyethylene Cores from 3D X-ray Microtomographic Imaging." *Journal of Colloid and Interface Science* 298 (1): 282-297.

Puddephat, M. 2001. *Nuclear magnetic resonance (NMR).* n.p

Purcell, W. R. 1949. "Capillary Pressures - Their Measurement Using Mercury and the Calculation of Permeability Therefrom." *Journal of Petroleum Technology* 1 (2): 39-48.

Quantachrome Instruments. n.d. "Pore Network Modeling from Mercury Intrusion/Extrusion Porosimetry." *Powder Tech Note* 33: 1-7.

Quantachrome Instruments. 2008. *Autosorb AS-1/ASWin Gas sorption system operation manual*. Boynton Beach, Florida: Quantachrome Instruments

Ravikovitch, P.I., Haller, G.L., Neimark, A.V., 1998. "Density functional theory model for calculating pore size distributions: pore structure of nanoporous catalysts". *Advances in Colloid and Interface Science* 76-77: 203-226.

Rezaee, M. R., Jafari, A. & Kazemzadeh, E. (2006). Relationships between permeability, porosity and pore throat size in carbonate rocks using regression analysis and neural networks. *Journal of Geophysics and Engineering* **3**, 370.

Ross, Daniel J. K., and R. Marc Bustin. 2009. "The Importance of Shale Composition and Pore Structure Upon Gas Storage Potential of Shale Gas Reservoirs." *Marine and Petroleum Geology* 26 (6): 916-927.

Rouquerol, J., D. Avnir, C. W. Fairbridge, D. H. Everett, J. M. Haynes, N. Pernicone, J. D. F. Ramsay, K. S. W. Sing, and K. K. Unger. 1994. "Recommendations for the characterization of porous solids." *Pure and Applied Chemistry* 66 (8): 1739-1758.

Rushing, Jay Alan, Kent Edward Newsham, and Thomas Alwin Blasingame. 2008a. "Rock Typing-Keys to Understanding Productivity in Tight Gas Sands." Paper presented at *SPE Unconventional Reservoirs Conference, Keystone, Colorado, 10-12 February*. doi: 10.2118/114164-MS.

Rushing, Jay Alan, Kent Edward Newsham, and Thomas Alwin Blasingame. 2008b. "Rock Typing 0x97 -Keys to Understanding Productivity in Tight Gas Sands." Paper presented at *SPE Unconventional Reservoirs Conference, Keystone, Colorado, 10-12 February*. doi: 10.2118/114164-MS.

Saeedi, Ali. 2013a. "Darcy's Law and Applications". Class lecture, Reservoir Engineering from Curtin Univesiyt, Perth, Western Australia, March 2013.

Saeedi, Ali. 2013b. "Storage Capacity of Reservoir Rocks". Class lecture, Reservoir Engineering from Curtin Univesiyt, Perth, Western Australia, March 2013.

Salman, Z., Amanat Ali, B., Hasnain Ahmad, K. & Toseef, A. 2007. "Development of Unconventional Gas Resources: Stimulation Perspective". *Production and Operations Symposium.* Oklahoma City, Oklahoma, U.S.A.

Shaw, J. C., M. M. Reynolds, and L. H. Burke, L. H. 2006. "Shale Gas Production Potential and Technical Challenges in Western Canada." Paper presented at *Canadian International Petroleum Conference, Calgary, Alberta, 13-15 June*. doi: 10.2118/2006-193.

Shirley, K. 2001. "Shale Gas Exciting Again." *AAPG Explorer* March: 1-4.

Siddiqui, Shameem, Abraham S. Grader, Mustafa Touati, Antonius M. Loermans, and James Joseph Funk. 2005. "Techniques for Extracting Reliable Density and Porosity Data From Cuttings." Paper presented at *SPE Annual Technical Conference and Exhibition, Dallas, Texas, 9-12 October*. doi: 10.2118/96918-MS.

Sisk, Carl, Elizabeth Diaz, Joel Walls, Avrami Grader, and Michael Suhrer. 2010. "3D Visualization and Classification of Pore Structure and Pore Filling in Gas Shales." Paper presented at *SPE Annual Technical Conference and Exhibition, Florence, Italy, 19-22 September*. doi: 10.2118/134582-MS.

Swanson, B. F. 1981a. "A Simple Correlation Between Permeabilities and Mercury Capillary Pressures." *SPE Journal of Petroleum Technology* 33 (12): 2498–2504.

Talabi, Olumide Adegbenga, Saif Alsayari, Martin Julian Blunt, Hu Dong, and Xiucai Zhao. 2008. "Predictive Pore Scale Modeling: From 3D Images to Multiphase Flow Simulations." Paper presented at *SPE Annual Technical Conference and Exhibition, Denver, Colorado, 21-24 September*. doi: 10.2118/115535-MS.

Talabi, Olumide Adegbenga, Saif AlSayari, Stefan Iglauer, and Martin J. Blunt. 2009. "Pore-scale Simulation of NMR Response." *Journal of Petroleum Science and Engineering* 67 (3-4): 168-178.

Tiab, Djebbar, and Erle C. Donaldson. 2004. *Petrophysics: Theory and Practice of Measuring Reservoir Rock and Fluid Transport Properties.* 2nd ed. Boston: Gulf Professional.

Timur, A. 1968. “An Investigation of Permeability, Porosity, and Residual Water Saturation Relationships For Sandstone Reservoirs.” *The Log Analyst* 9 (4): 8.

Volkert, C. A., and A. M. Minor. 2007. “Focused Ion Beam Microscopy and Micromachining.” *MRS Bulletin* 32 (5): 389-399.

Volokitin, Y., Looyestijn, W. J., Slijkerman, W. F. J. & Hofman, J. (1999). A Practical Approach to Obtain Primary Drainage Capillary Pressure Curves from NNR Core And Log Data. *SCA*.

Walls, Joel D. 1982. “Tight Gas Sands-Permeability, Pore Structure, and Clay.” *Journal of Petroleum Technology* 34 (11): 2708-2714.

Wang, Xiaowen, Lizhi Xiao, Ranhong Xie, and Yuanzhong Zhang. 2006. “Study of NMR Porosity for Terrestrial Formation in China.” *Science in China: Series G Physics, Mechanics and Astronomy* 49 (3): 313-320.

Washburn, E. W. 1921. “Note on a Method of Determining the Distribution of Pore Sizes in a Porous Material”. *Proc Natl Acad Sci U S A* 7: 115-116.

Wyllie, M.R.J and Gregory, A.R.. 1955. “Fluid flow through unconsolidated porous aggregates: Effect of porosity and particle shape on Kozeny-Carman constants”. *Industrial & Engineering Chemistry* 47 (7): 1379–1388.

Yao, Yanbin, and Dameng Liu. 2012. “Comparison of Low-field NMR and Mercury Intrusion Porosimetry in Characterizing Pore Size Distributions of Coals.” *Fuel* 95: 152-158.

Xu, Peng, and Boming Yu. 2008. “Developing a New Form of Permeability and Kozeny–Carman Constant for Homogeneous Porous Media by Means of Fractal Geometry.” *Advances in Water Resources* 31 (1): 74-81.

Zahid, S., Bhatti, A., Khan, H. and Ahmed, T. 2007. “Development of Unconventional Gas Resources: Stimulation Perspective.” Paper presented at *Production and Operations Symposium, Oklahoma City, Oklahoma, 31 March-3 April*. doi: 10.2118/107053-MS.

Zhi-Qiang, Mao, He Yu-Dan, and Ren Xiao-Jun. "An Improved Method of Using Nmr T2 Distribution to Evaluate Pore Size Distribution." Chinese Journal of Physics 48, no. 2 (2005): 412-18.

6. APPENDIX

6.1 Appendix 1: XED Results

Sample ID	Quartz	K-Feldspar	Siderite	Pyrite	Natro-jarosite	Ankerite/ FE-Dolomite	Plagio-clase	Calcite	Dolomite	Fluora-patite	Barite	Magnetite	Kerogen/ Others	Smectite	Mixed Illite/ Smectite (20%S)*	Illite/ Mica	Kaolinite
1	15.1	6.3	1.4	1.3									17.9		6.4	13.3	28.3
2	14.7	4.7	0.5	0.9									22.6		12	8.2	29.1
5	34.1	1.3		1.6			8.3	1.5					8.3		27.6	3.7	4.3
6	37.3	2.7		1.2			5.3	0.5	1.2				8.1		32.5	3.2	2.1
8	24.5	4	0.8	3.7			5.7	4			0.4	0.9		1.7	19.8	24.9	2.6
11	49.2	4	1.4	1.7		1.2	4.6	3.3		0.2	0.4			1.7	12.4	14.3	0.9
13	53	3.3	1	2.1		0.2	8.1	0.9		0.4				1.6	11.7	13.9	0.8
14	41.3	3.6	1.5	3.1		0.7	7.6	0.6	0		0.7			0.9	14.9	18.9	0.8
15	53.8	4	1.2	1.7		1.8	7.8	1.2	0.4	0.2	0			1.7	10.4	12.4	0.5
16	44.5	3.6	2.3	0.9		1	10.8	2.1	1.1		0.5			1.9	9.7	16	1.2
17	51.1	5.3	2.4												5.8	11.8	19.7
18	47.2	6.9	0.5		1.9											14.6	27.8
19	54.1	2.5	0.4	0.6	2.5											13.5	25.6
20	56.1	6.5	0.6		2.9											11.5	21.5
21	45.6	6.5	0.8	0.3	3.9											14.7	26.8
22	52.5	3	0.6	0.2	1.2										9	15.1	16.6
23	67.1	9.1	0.5	0.2	1.8											9.7	11.3
24	60.5	1.3	0.3	1.5	1.2										3	8.5	22.6
25	67.2	3.6	0.5	0.6	2.1											11.6	13.8
26	50.5	2.4	0.4		0.8										4.1	13.7	25.1
27	34.2	3.2	20.5		0.8										7.2	12	17.6
30	23.3	0.8		10.4			3.6	0.5					8		25.1	4.9	16.3
31	15.5	0.8		3.7			2.9	21.9					6.5		27.7	4.5	10.5

Table 6-1: XRD Results for the shale collection

6.2 Appendix 2: MICP Pore Throat Size Distribution

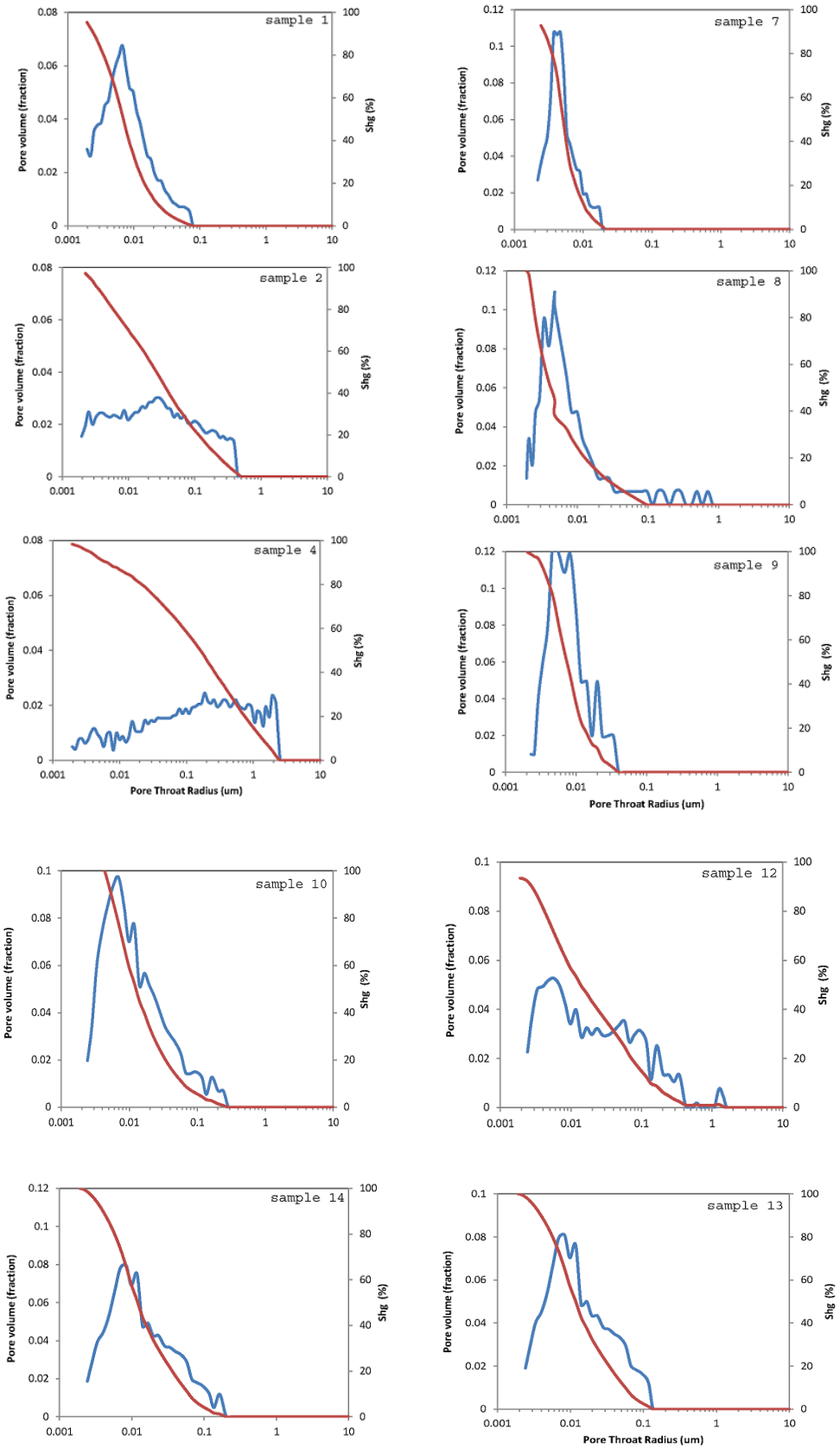

Figure 6-1: PSD versus mercury saturation and pore volume for PCM samples

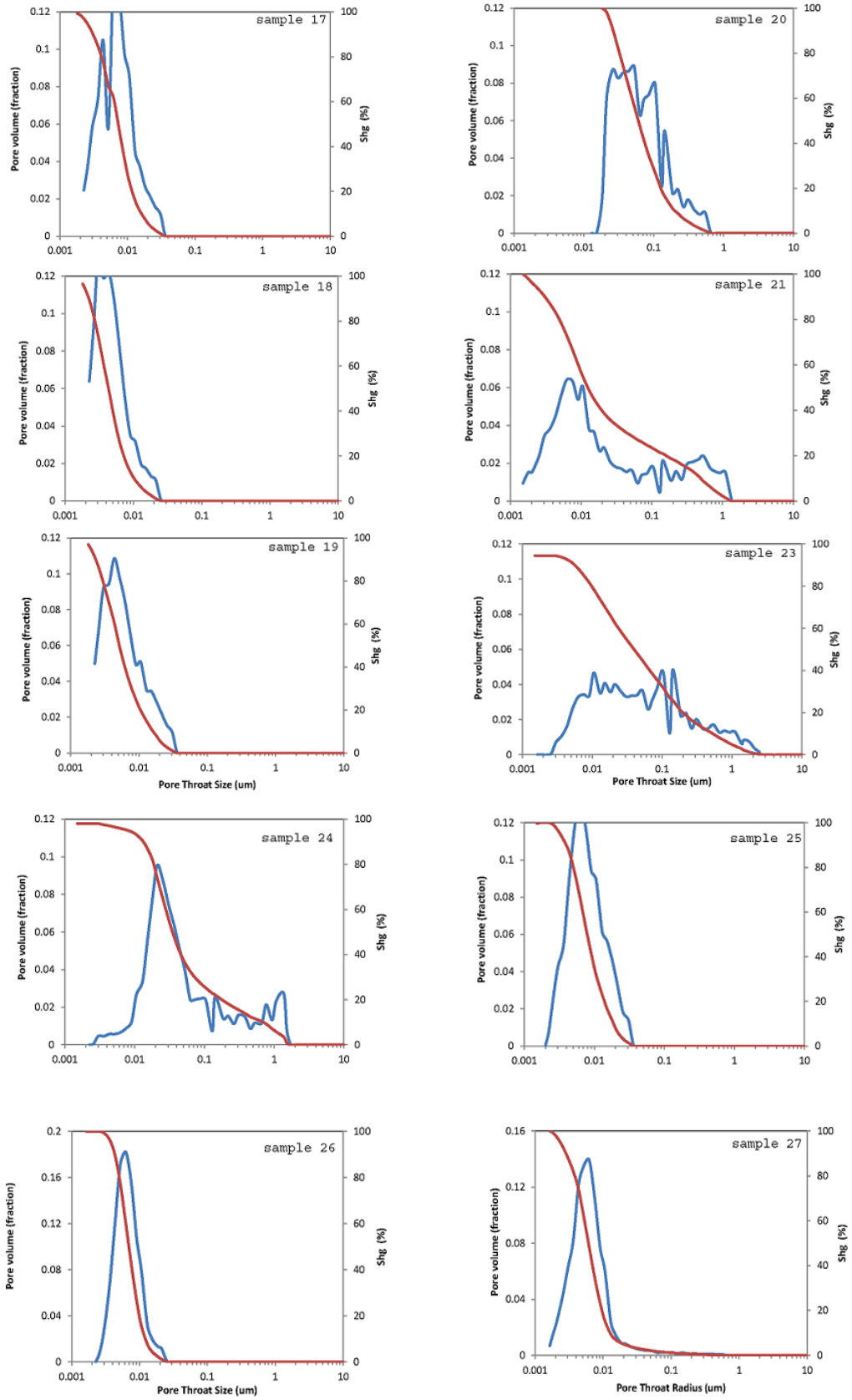

Figure 6-2: PSD versus mercury saturation and pore volume for CCM samples

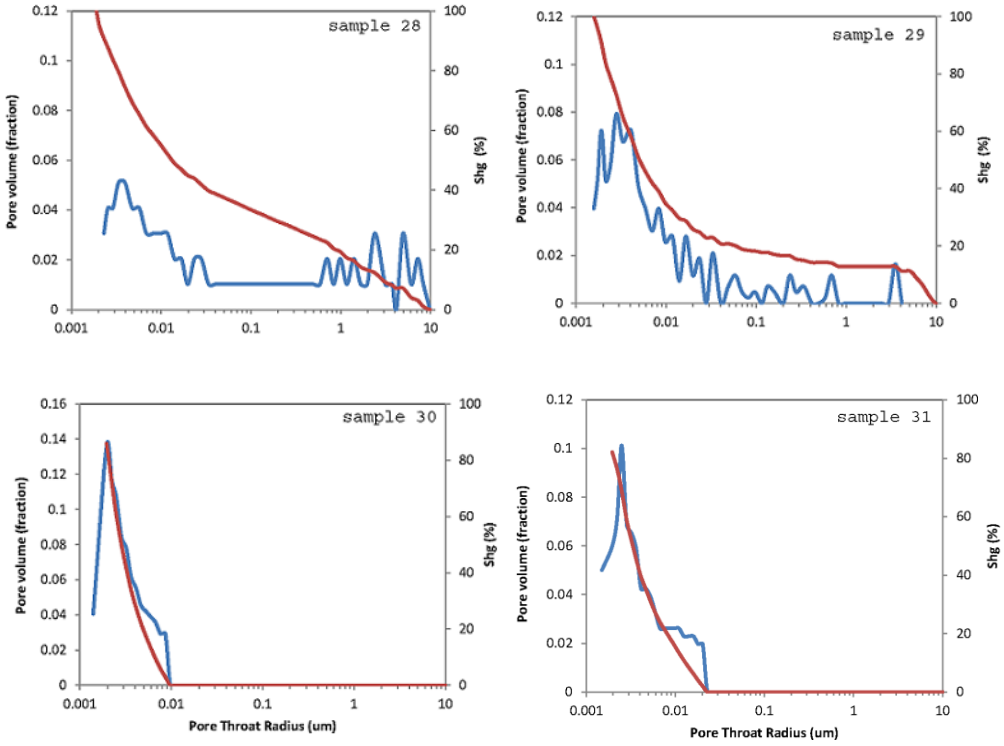

Figure 6-3: PSD versus mercury saturation and pore volume for PKM samples

6.3 Appendix 3: NMR T_2 Relaxation Time

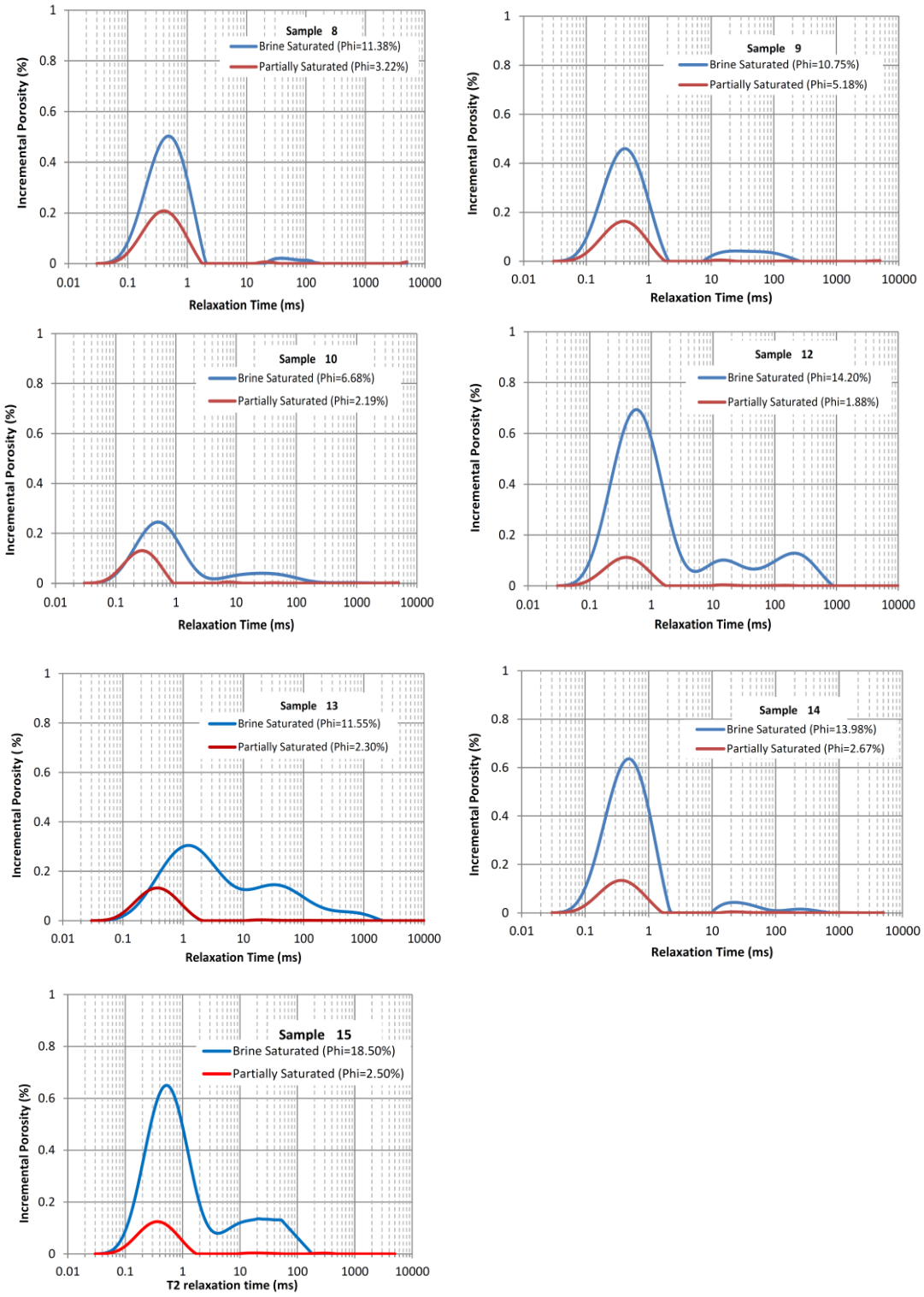

Figure 6-4: NMR pore size distribution of partially saturated and brine saturated for the individual PCM shale samples

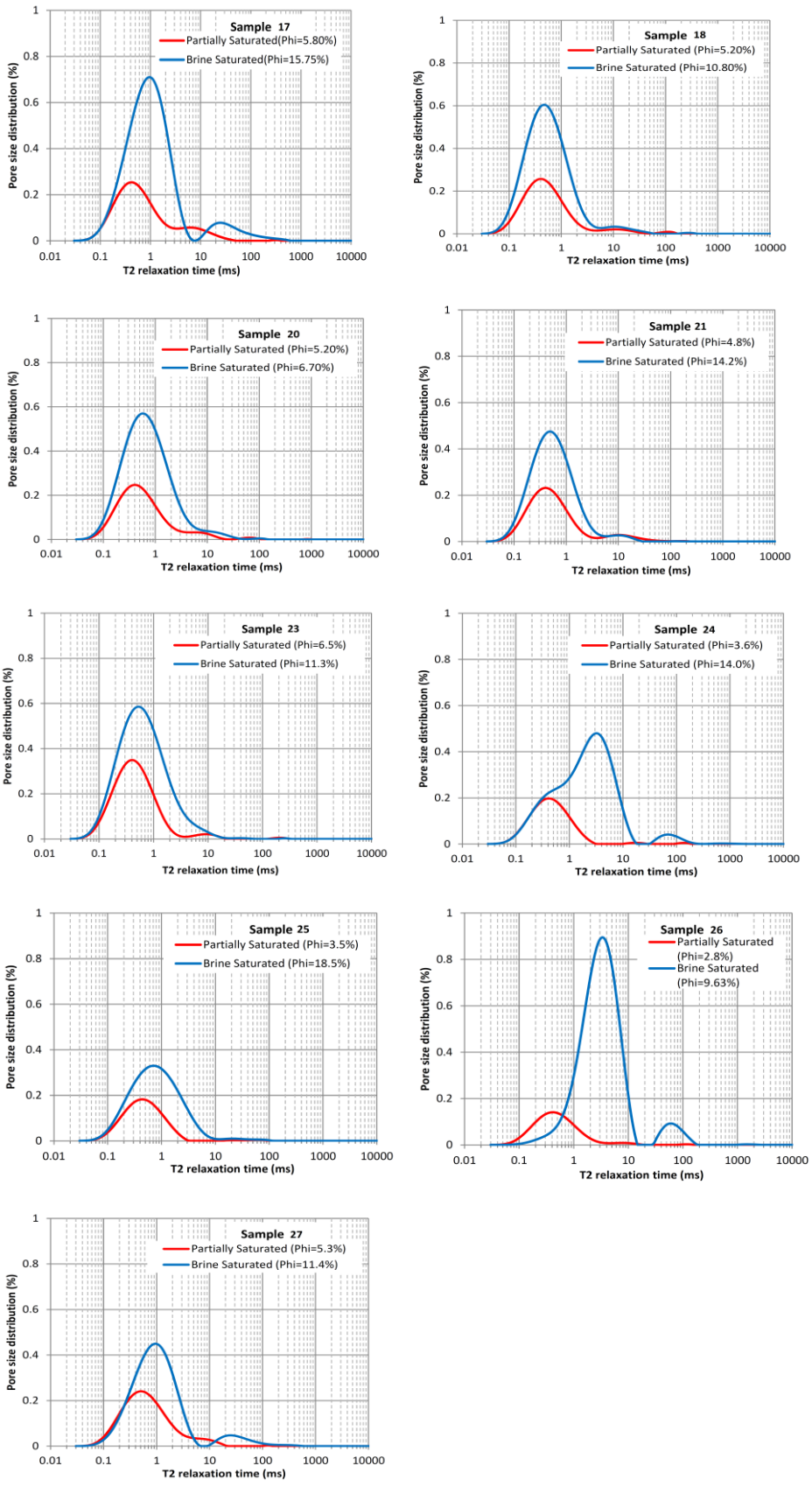

Figure 6-5: NMR pore size distribution of partially saturated and brine saturated for the individual CCM shale samples

6.4 Appendix 4: N_2 adsorption and desorption graphs

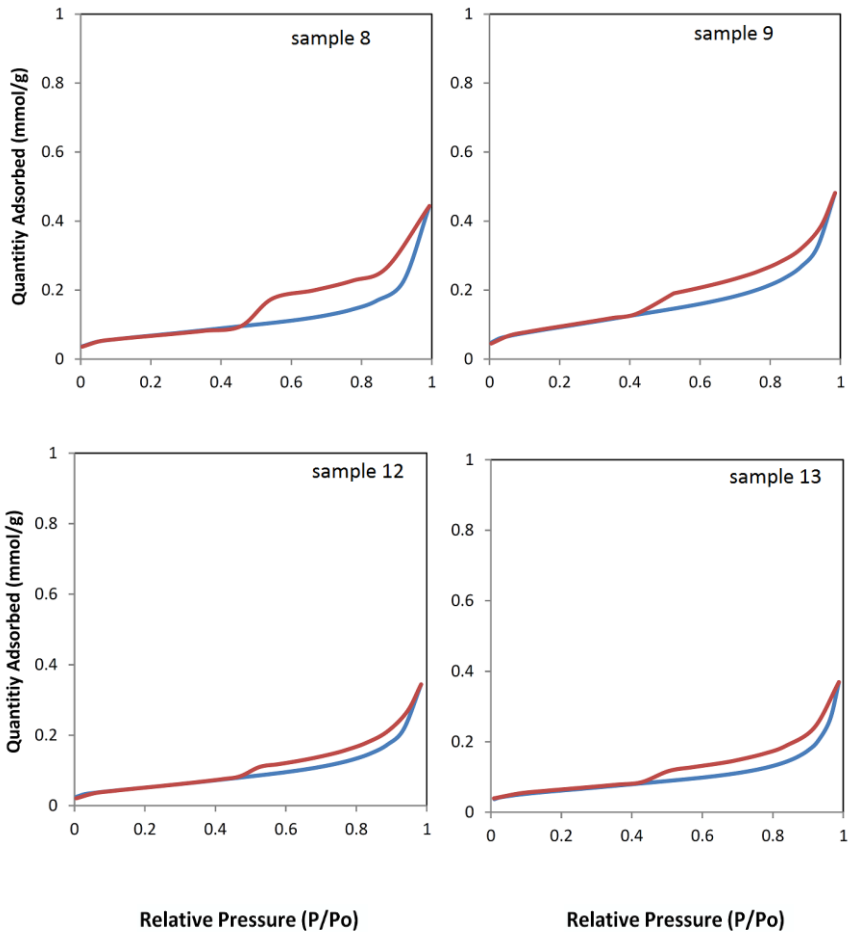

Figure 6-6: PCM N_2 adsorption (blue) and desorption (red) graphs

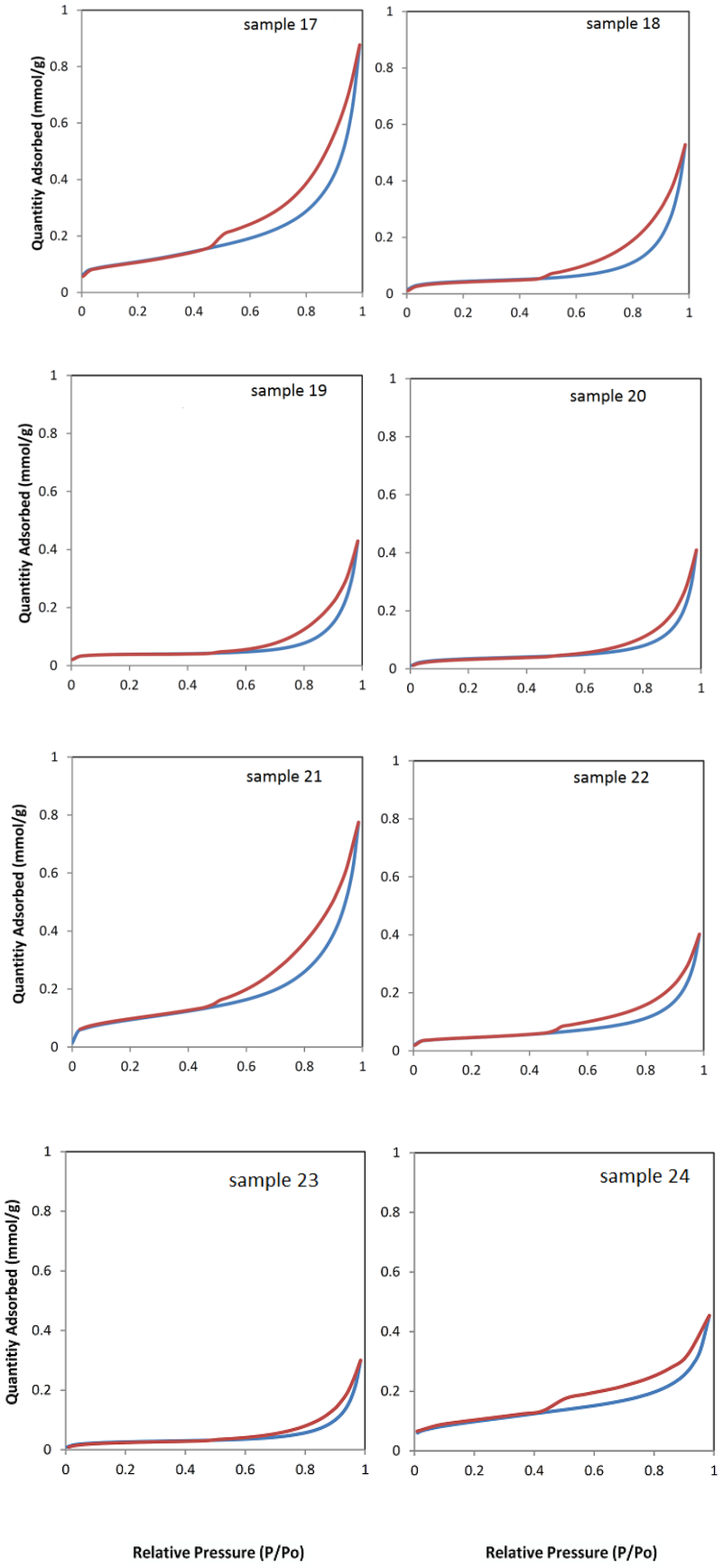

Figure 6-7: CCM N_2 adsorption (blue) and desorption (red) graphs

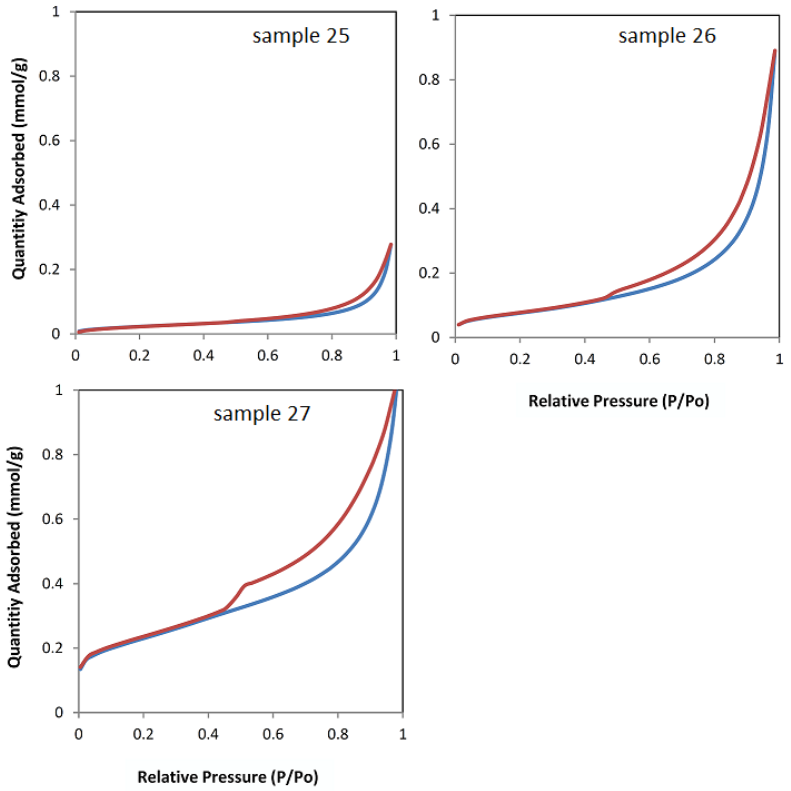

Figure 6-8: CCM N_2 adsorption (blue) and desorption (red) graphs

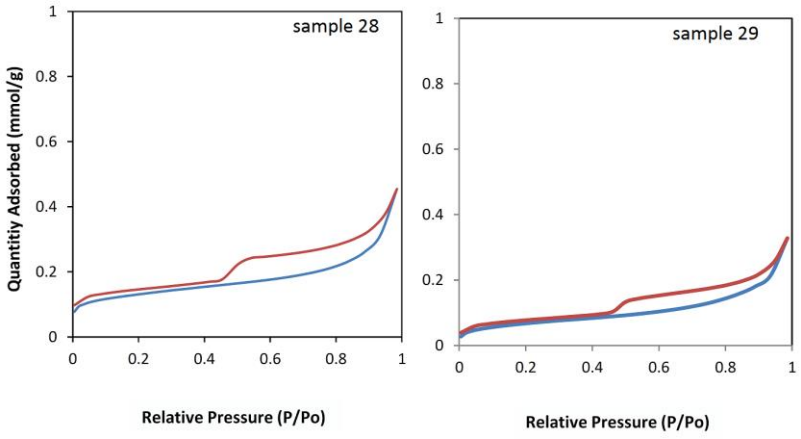

Figure 6-9: PKM N_2 adsorption (blue) and desorption (red) graphs

6.5 Appendix 5: Additional SEM Images of the Shale Samples in Study

SEM imaging for PCM samples were conducted using a Zeiss Neon 40EsB equipped with a field emission gun with a maximum EHT voltage of 30 kV. Figure 6-10 shows additional acquired images for PCM samples.

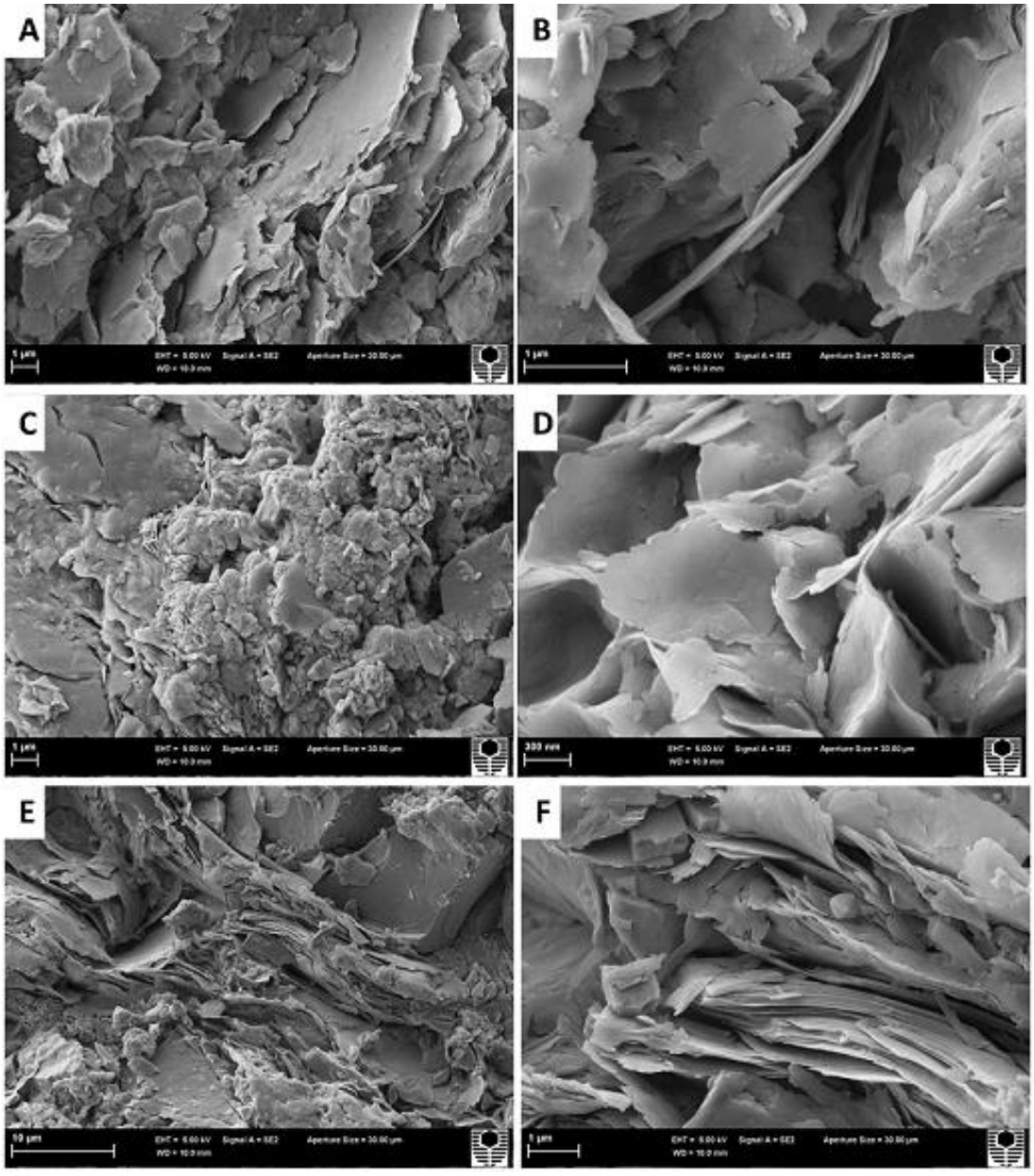

Figure 6-10: SEM Images of PCM shale samples. A & B sample 8, C & D sample 14 and E & F sample 16. Images showing ehe clay particles displayed as repeating layers of flat platelets, typical of Illite and/or Kaolinite.

SEM imaging and energy dispersive x-ray spectroscopy (EDS) was conducted on CCM samples using a Philips XL40 equipped with a Bruker Quantax EDS detector. The Philips XL40 is a controlled pressure SEM equipped with a tungsten filament with a maximum EHT voltage of 30 kV. Figure 6-11 shows additional acquired images for CCM samples.

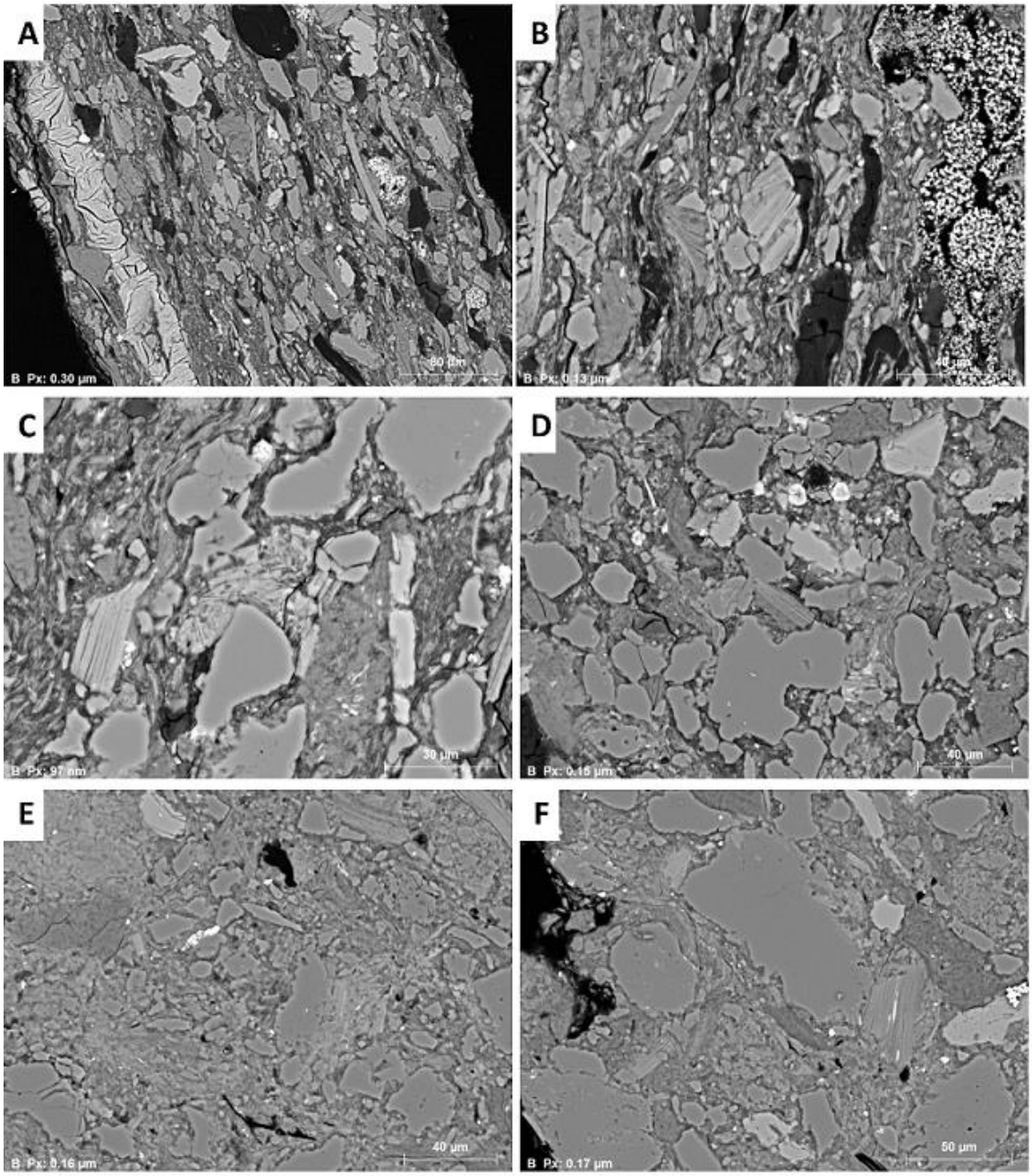

Figure 6-11: SEM Images of CCM samples. A & B sample 18, C & D sample 20 and E & F sample 22. The dominant particles are kaolinite, illite and quartz particles.

6.6 Appendix 6: Additional FIB/SEM Image Acquisition Setup

FIB/SEM image acquisition was conducted on sample 10 from PCM formation using a FEI DualBeam Focused Ion Beam Scanning Electron Microscope to visually inspect the pore characteristics and to support experimental analysis (Figure 6-12).

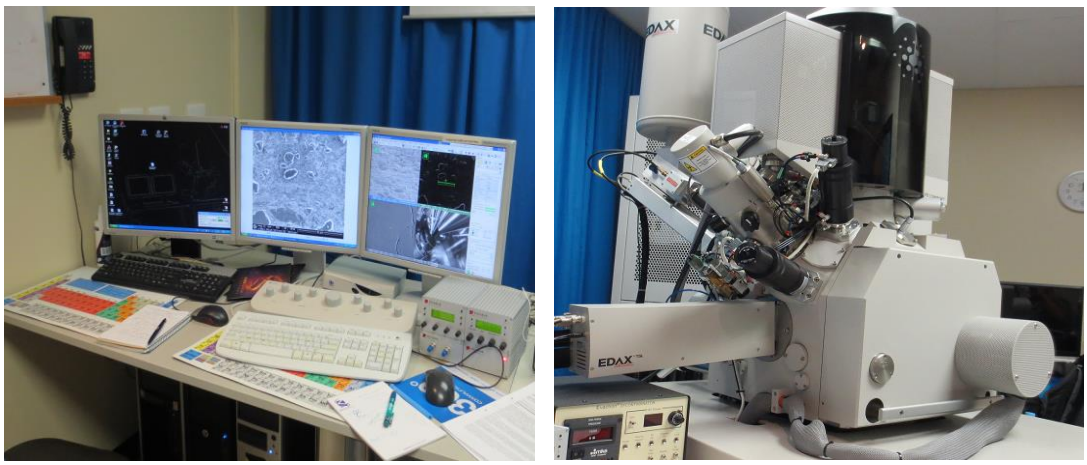

Figure 6-12: FEI DualBeam used for FIB/SEM image acquisition

A chunk of ± 20 x 5 mm size from the sample 10 embedded in resin and the surface polished up to 1200 grit. The sample was then placed on an aluminium stub using a silver dab and coated with silver (Figure 6-13).

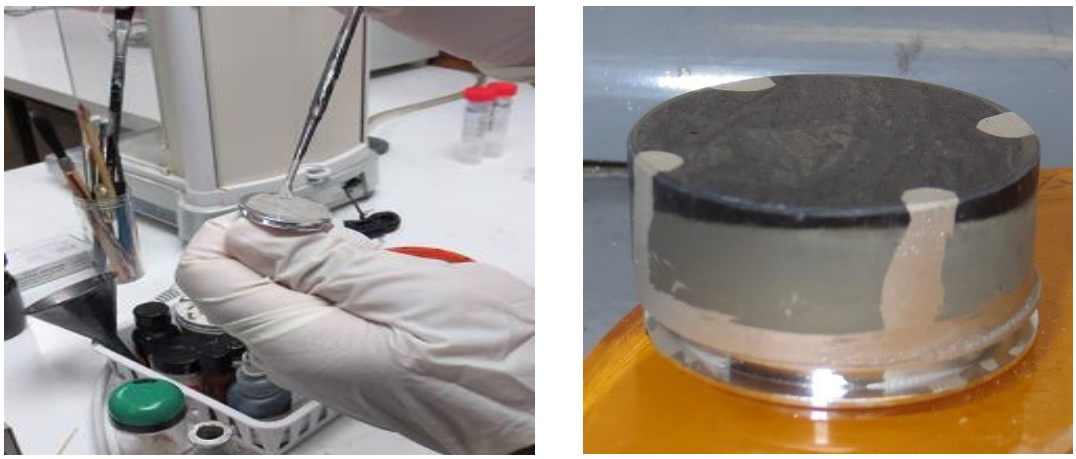

Figure 6-13: Sample preparation (left) silver dag placed on the stub (right) polished sample

Figure 6-14 shows the sample being placed on the dual beam stage at a working distance of 4mm. After completing the necessary instrument setup and automated cut and slice is performed (Figure 6-15).

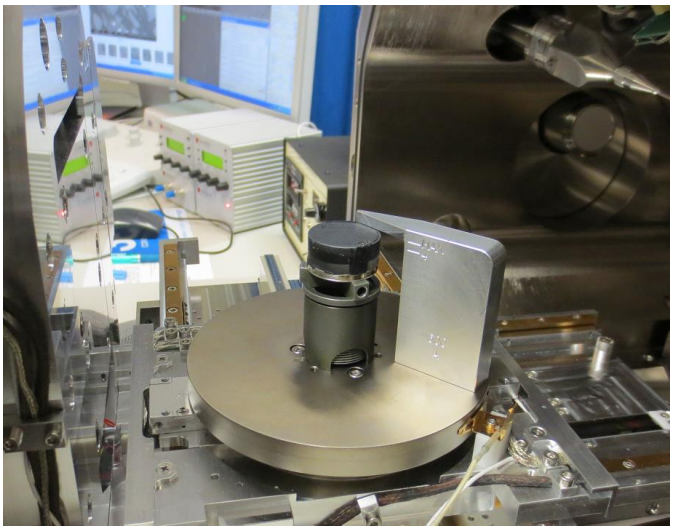

Figure 6-14: Sample placed on the dual beam stage

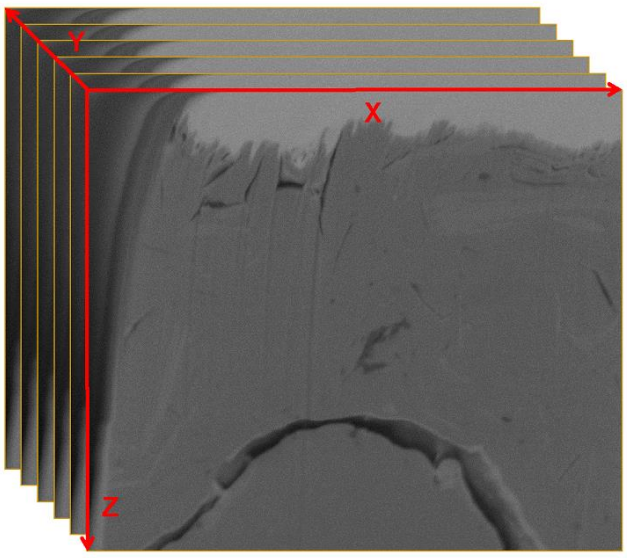

Figure 6-15: Illustration of the slice and view setup for sample 10. With dimensions of W= 10um, L=7um and D=10um. The length per slice is 35nm. Takes approximately 13 hours for 200 slices